

**“Surface Derivatization of Polymer/Nanoparticles for Diverse
Biological Applications”**

THESIS

Submitted in partial fulfilment
of the requirements for the degree of

DOCTOR OF PHILOSOPHY

By

Pranay Amruth Maroju

ID No: 2018PHXF0008H

Under the Supervision of

Prof. Jayati Ray Dutta

&

Co-Supervision of

Prof. Ramakrishnan Ganesan



BITS Pilani
Pilani | Dubai | Goa | Hyderabad


BIRLA INSTITUTE OF TECHNOLOGY AND SCIENCE - PILANI

2023

CERTIFICATE

This is to certify that the thesis entitled “**Surface Derivatization of Polymer/Nanoparticles for Diverse Biological Applications**” was submitted by **Pranay Amruth Maroju**, ID No: **2018PHXF0008H** for the award of the Ph.D. of the Institute embodies original work done by him under our supervision.

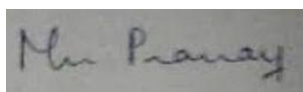
Signature of the Supervisor : 
Name in capital letters : PROF. JAYATI RAY DUTTA
Designation : Associate Professor, Department of Biological Sciences
Date : 08-05-2023

Signature of the Co-supervisor: 
Name in capital letters : PROF. RAMAKRISHNAN GANESAN
Designation : Associate Professor, Department of Chemistry
Date : 08-05-2023

Declaration

I, Pranay Amruth Maraju, declare that this thesis titled, “**Surface Derivatization of Polymer/Nanoparticles for Diverse Biological Applications**”, submitted by me under the supervision of Prof. Jayati Ray Dutta and Prof. Ramakrishnan Ganesan is a bonafide research work. I also declare that it has not been submitted previously in part or in full to this University or any other University or Institution for award of any degree.

Signature of the Student :



Name of the Student :

PRANAY AMRUTH MAROJU

ID number of the Student :

2018PHXF0008H

Date :

08-05-2023

Acknowledgements

Firstly, I thank the **Director** (BITS-Pilani, Hyderabad Campus) for my research funding and fellowship.

I am grateful and indebted to my supervisors, **Prof. Jayati Ray Dutta** (Department of Biological Sciences) and **Prof. Ramakrishnan Ganesan** (Department of Chemistry), for their constant encouragement, guidance, and support.

I thank the **Head of the Department** and **Doctoral Research Committee** for facilitating my work at the department of biological sciences.

I am grateful to my **Doctoral Advisory Committee** members, **Prof. Kumar Pranav Narayan** (Department of Biological Sciences) and **Prof. Kannan Ramaswamy** (Department of Physics), for their valuable suggestions and critical review.

I sincerely thank the **reviewers**, **Prof. Sanjoy Ghosh** (IIT-Kharagpur) and **Prof. Supratim Dutta** (IISER, Kolkata) for critically reviewing my research work.

I thank all the *department's faculty members* for their support and encouragement.

This thesis will only be possible with my past - **Dr. Imran and Dr. Almas**; present lab mates - **Mr. Aniket, Ms. Pranathi, Ms. Hemanjali, Ms. Mariya, and Ms. Anindita**

I thank all my colleagues and friends (**Daipayan, Akshay, Shifa, Sonal, Shiv, Monica, Sumana, Anuhya, Minali, and Dwaipayan**) for their unconditional help and support.

I thank the **technical staff** (Department of Biological Sciences), **Mr. Ramakrishna, Mr. Imtiyaz, Mrs. Geethanjali, Mrs. Purnima, Mr. Santosh, and Mr. Kutumba Rao**, for all their help and cooperation.

I thank the **technical staff** (Central Analytical Laboratory), **Mr. Uppalaiah, Mr. Mallesh, Mr. Suresh, Mr. Narasimha, Mr. Tirumalaiah, Mr. Balakishan, and Mr. Balakrishna** for their immense support and help.

Lastly, I thank my parents (**Kamal and Madhavi**), sister (**Divya**), and my best friend (**Shifa**) for being a pillar of strength and providing me the constant support.

Abstract

Polymers and nanoparticles have a wide range of applications in the field of biology ranging from catalysis to cancer therapy. In recent years several bio-polymers and nanoparticles have shown great potential in controlling microbial infections in medicine, drug delivery in cancer therapy, and tissue engineering. Nanoparticles have also been employed in developing biosensors for rapidly detecting diseases and separating biomolecules in catalysis. Surface derivatization plays a crucial role in imparting new functions to bio-polymers and nanoparticles and enables their use in above mentioned biological applications. In this thesis, we employed robust chemical-based surface modification techniques to render bactericidal activity to an FDA-approved polymer for biomedical applications, enabled the use of nanoparticles in nucleic acid (DNA/RNA) sensing, and enhanced the activity of biocatalysts (lipases) from benign sources in biofuel production.

Poly(ϵ -caprolactone) (PCL) is a widely used biopolymer in bone and dental implants and lacks inherent antimicrobial properties like other natural antimicrobial polymers (Poly(ethylene glycol) and Chitosan). Several researchers have worked on imparting antibacterial properties to PCL by blending with antibiotics, antimicrobial peptides, and chemical substances. However, extensive use of antibiotics poses a threat of antimicrobial resistance, through mutations in the bacteria and host cells. Recent studies showed that inorganic nanoparticles have antimicrobial properties with little or no side effects. Among various metallic nanoparticles, silver is a highly efficient inorganic broad-spectrum antimicrobial substance. Silver at lower oxidation states oxidizes quickly and loses its ability as an antibacterial substance which can be prevented by stabilizing agents like proteins. Our study employs EDC-NHS chemistry to surface derivatize the PCL films to immobilize silver stabilized by a probiotic (*Lactobacillus amylovorus*)-derived lipase. The antimicrobial studies employing silver-derivatized PCL films on *E.*

coli have revealed 100 % inhibition in bacterial growth in 4–6 h. Additionally, the cytotoxicity assay on mouse fibroblast cells exhibited high cell compatibility, making it suitable for *in vivo* applications.

Gold nanoparticles (Au NPs) and Magnetic nanoparticles (MNPs) possess enormous potential in nucleic acid diagnosis, especially in low-cost settings. Gold-based diagnosis relies on efficient tagging of thiol-modified nucleic acid probes to the gold surface and suitable hybridization conditions between probe and target molecules. In the current study, we modified the hybridization conditions between the target and the antisense oligonucleotide for stable duplex formation and enhanced thiolated ASO's tagging over the Au NPs by adding citrate buffer. The combinatorial effect of these conditions is proven to be advantageous and showed enhanced sensitivity of ratiometric genosensing using Au NPs. Magnetic nanoparticles immobilized with probes through silanization were employed to demonstrate a facile fluorescence-based simultaneous dual oligo sensing of HCV genotypes 1 and 3. Hybridization between the two probes with their target, followed by magnetic removal of the NPs from the solution, enabled quantitative analysis of the target by measuring the fluorescence intensity of the residual concentration of the second fluorescently-tagged probe in the solution. Through this approach, the targets corresponding to genotypes 1 and 3 were simultaneously detected with a detection limit of 10–15 nM.

Boronic acid having a high affinity to 1,2- and 1,3-diols to form a boronic ester, has been vastly used in reactions with sugar moieties for RNA sensing. However, little is known about its interaction with sugar moieties, with only mono-ol units present in single- and double-stranded DNA (ss and dsDNA). In our study, we probe the interaction of boronic acid with oligonucleotides towards DNA sensing, using gold coated magnetic nanoparticles and a fluorophore, 3-dansylaminophenyl-boronic acid (DAPBA). We demonstrated the feasibility of quantitative DNA detection by boronic acid-mediated 3'-hydroxy cross-linking of adjacent

DNA double helices with proximal mono-ol units. This is the first successful approach for the quantitative detection of DNA in addition to RNA. Through this strategy, fluorescence tagging of nucleotides after hybridization is simple and robust. Furthermore, the reversible binding nature of boronic acid at acidic pH facilitates facile oligonucleotide recovery, thereby reducing detection costs.

Lipases are potential biocatalysts for converting fatty acid esters into biodiesel. Nevertheless, most of the lipases employed for this purpose are derived from either fungal or non-probiotic sources, many of which produce harmful toxins during their life cycle. Such concerns do not arise in the case of lipases derived from probiotic origin. In the current work, we derived a lipase from *Bacillus licheniformis*, a probiotic source, and immobilized it over magnetite nanoparticles along with bovine serum albumin (BSA). The immobilized lipase showed high efficacy even at a minimal enzyme loading of 0.11 wt% to the oil in 2 h of duration and retained >50% relative activity even at the eighth cycle.

Contents

	Page No.
<i>Acknowledgements</i>	01
<i>Abstract</i>	03
<i>Contents</i>	06
<i>List of Tables</i>	10
<i>List of Figures</i>	11
<i>List of Abbreviations</i>	15
<i>Chapter 1</i>	17
<i>1.1. Introduction</i>	18
<i>1.2. Review of Literature</i>	20
<i>1.2.1 Surface functionalization of polymer for disinfection performance</i>	20
<i>1.2.2 Nanoparticle mediated bio sensing of oligonucleotides</i>	22
<i>1.2.3 Biofuel generation through probiotic-derived immobilized enzymes</i>	24
<i>1.3 Gaps in existing research</i>	26
<i>1.4 Objectives</i>	26
<i>Chapter 2</i>	27
<i>2.1 Introduction</i>	28
<i>2.2 Methodology</i>	30
<i>2.2.1 Materials</i>	30
<i>2.2.2 PCL film casting and alkaline hydrolysis</i>	30
<i>2.2.3 EDC/NHS-activation</i>	31
<i>2.2.4 Lipase production from L. amylovorus</i>	31
<i>2.2.5 Synthesis of lipase-capped Ag NPs</i>	32

2.2.6 Immobilization of lipase-capped Ag NPs over PCL films	32
2.2.7 Ag deposition over PCL films through dip-coating method	33
2.2.8 Antimicrobial studies	33
2.2.9 Cytotoxicity assay	34
2.2.10 Characterization	34
2.3 Results and Discussions	35
2.3.1 PCL surface derivatization strategy	35
2.3.2 Surface characterization	36
2.3.3 Antimicrobial activity	41
2.3.4 In vitro cytotoxicity	44
2.4 Conclusions	45
Chapter 3	46
3.1 Introduction	47
3.2 Methodology	49
3.2.1 Materials and Characterization	49
3.2.2 Au NPs based geno-sensing	49
3.3 Results and Discussion	51
3.4 Conclusions	58
Chapter 4	59
4.1 Introduction	60
4.2 Methodology	61
4.2.1 Materials	61
4.2.2 Design of the Oligonucleotides	62
4.2.3 Surface Derivatization of Magnetite NPs	62
4.2.4 Dual Oligo Sensing	63

4.2.5 Characterization	64
4.3 Results and Discussion	64
4.4 Conclusions	71
Chapter 5	73
5.1 Introduction	74
5.2 Methodology	74
5.2.1 Materials	75
5.2.2 Synthesis of $Fe_3O_4@Au$ core-shell nanostructures	76
5.2.3 Immobilization of thiolated probe over the core-shell nanostructures	76
5.2.4 Oligonucleotide sensing	77
5.2.5 Agarose gel Electrophoresis	78
5.3 Results & Discussion	78
5.4 Conclusions	88
Chapter 6	89
6.1 Introduction	90
6.2 Methodology	91
6.2.1 Materials	91
6.2.2 Production of native lipase (NL) from <i>B. licheniformis</i>	92
6.2.3 Production of recombinant lipase (EL)	93
6.2.4 Lipase activity	94
6.2.5 Lipase immobilization over magnetite nanoparticles (MNPs)	95
6.2.6 Effect of temperature and pH on lipase activity	96
6.2.7 Transesterification reaction	96
6.2.8 Optimization of the transesterification reaction parameters	97
6.2.9 Recyclability studies of the catalyst	97

6.2.10 <i>Characterization</i>	98
6.3 <i>Results and Discussion</i>	98
6.3.1 <i>Induction and purification of the native lipase (NL)</i>	98
6.3.2 <i>Production of recombinant lipase (EL)</i>	99
6.3.3 <i>Circular dichroism (CD) study</i>	100
6.3.4 <i>Immobilization of lipase over magnetite nanoparticles</i>	102
6.3.5 <i>Lipase activity by the p-NP assay</i>	104
6.3.6 <i>Biodiesel production through transesterification of RBO</i>	105
6.3.7 <i>Characterization of the biodiesel</i>	108
6.3.8 <i>Recyclability studies</i>	112
6.4 <i>Conclusions</i>	115
Chapter 7	117
7.1 <i>Summary</i>	118
7.2 <i>Conclusions</i>	118
7.3 <i>Major contributions of the work</i>	122
7.4 <i>Future scope of the work</i>	123
<i>References</i>	125
<i>Publications (from Thesis)</i>	155
<i>Publications (outside Thesis)</i>	156
<i>Publications (from previous work)</i>	157
<i>Conferences</i>	158
<i>Biography of Student</i>	159
<i>Biography of Supervisor</i>	160
<i>Biography of Co-supervisor</i>	161

List of Tables

Table No.	Title	Page No.
Table 3.1	UV-visible absorbance data	54
Table 4.1	Complementary probes for each genotype 1 and 3, target and control probes.	62
Table 5.1	Oligo sequences used in quantitative DNA/RNA sensing.	76
Table 5.2	LODs of fluorescence-based DNA sensing.	87
Table 6.1	Lipase gene sequence (codon-optimized) from <i>B. licheniformis</i> .	93
Table 6.2	Summary of the reaction parameters in the optimization of the transesterification reaction	97
Table 6.3	Parameters of secondary structure corresponding to Figure 6.3 (b)	101
Table 6.4	Salient parameters employed in the enzymatic biodiesel production using lipases from various sources	107

List of Figures

Figure No.	Title	Page No.
Figure 1.1	Applications of biopolymers and nanoparticles.	19
Figure 1.2	Surface modification techniques.	20
Figure 2.1	Pictorial representation depicting the strategies employed in this study for surface derivatization of PCL films with silver.	35
Figure 2.2	(A). UV-visible spectra of lipase-capped Ag NPs. STEM images of the Ag NPs synthesized using (B) 0.6 mM and (C) 1.0 mM Ag NO ₃ .	36
Figure 2.3	Contact angle measurements over (a) pristine, (b) 2 h alkaline hydrolyzed, and (c) 4 h alkaline hydrolyzed PCL films.	36
Figure 2.4	XPS narrow scan spectra of pristine, hydrolyzed, EDC/NHS-activated, lipase-immobilized, PCL-5-Ag-dip, PCL-10-Ag-dip, PCL-0.6- Ag-imm, and PCL-1.0-Ag-imm PCL films.	37
Figure 2.5	XPS spectra of pristine PCL film and alkaline-mediated hydrolyzed samples (before and after treatment with dilute HCl).	38
Figure 2.6	XPS survey scan spectra of PCL films subjected to various steps in the surface derivatization process.	40
Figure 2.7	FE-SEM images of pristine and EDC/NHS activated PCL films.	41
Figure 2.8	(i). Antimicrobial studies with pristine and silver-derivatized PCL films against <i>E. coli</i> for different incubation periods. (ii). Bacterial cell viability derived from the colony count data of antimicrobial study using the pristine	42, 43
Figure 2.9	(i). FE-SEM images of PCL-0.6-Ag-imm, and PCL-1.0-Ag-imm after 24 h incubation in the bacterial culture. (ii). XPS narrow scan spectra of PCL-0.6-Ag-imm, and PCL-1.0-Ag-imm samples after 24 h incubation in the bacterial culture.	43, 44
Figure 2.10	Cell viability study over mouse fibroblast cells (SNL 76/7) using the pristine and silver-derivatized PCL films.	45
Figure 3.1	Mechanism of the sensing strategy employed in Au NP based	50

	geno-sensing.	
Figure 3.2	(a) Polyacrylamide gel electrophoresis of probe-target and - control hybrids at different hybridization conditions (b) quantification of hybridization using ImageJ software.	52
Figure 3.3	The UV-visible spectra of the Au NPs at different hybridization conditions.	53
Figure 3.4	$A_{700/520}$ ratiometric values as a function of different hybridization conditions.	55
Figure 3.5	Digital photograph showing of the Au NPs subjected to different hybridization conditions before and after salting-out process.	57
Figure 3.6	Dynamic light scattering analyses over Au NPs in citrate buffer before and after salting-out process (340 mM NaCl).	57
Figure 4.1	(a) Schematic representation of the surface-derivatization of magnetite NPs. (b) Pictorial representation of the two-step hybridization method of simultaneous dual oligo sensing.	65
Figure 4.2	XPS narrow scan spectra of (a) Fe $2p$, (b) Si $2p$, (c) N $1s$, and (d) P $2p$ levels of magnetite NPs before and after each surface derivatization steps.	66
Figure 4.3	FE-SEM images of magnetite NPs before and after surface derivatization steps at two different magnifications.	67
Figure 4.4	Digital photograph of the PAGE bands (shown in the inset) and their percentage intensity analyses of the amine-tagged probes in the supernatant solution before and after immobilization over the glutaraldehyde-derivatized magnetite NPs.	68
Figure 4.5	Optimization of the hybridization parameters for the dual oligo sensing by employing one-step and two-step hybridization methods using the oligos derived from HCV genotype 1.	69
Figure 4.6	Quantitative dual oligo sensing of HCV genotypes 1 and 3.	70
Figure 4.7.	Stability analysis of the freshly prepared (a) and 3 months aged (b) probe-immobilized magnetite NPs. (c, d) Genotype sensing studies using synthetic serum in comparison to water.	71
Figure 5.1.	Diagrammatic representation of the boronic acid-mediated DNA sensing strategy.	75

Figure 5.2	Field emission scanning electron microscopy images of Fe ₃ O ₄ @Au core-shell nanostructures. (a) before and (b) after immobilization of the thiolated probe.	79
Figure 5.3	P 2 <i>p</i> and N 1 <i>s</i> narrow scan spectra of Fe ₃ O ₄ @Au core-shell nanostructures before probe immobilization (a and d), after immobilization of thiolated probe (b and e) and after hybridization with cDNA and cRNA (c and f).	80
Figure 5.4	Fe 2 <i>p</i> and Au 4 <i>f</i> narrow scan spectra of Fe ₃ O ₄ @Au core-shell nanostructures before probe immobilization (a and e), after immobilization of thiolated probe (b and f) and after hybridization with cDNA (c and g), and cRNA (d and h).	80
Figure 5.5	Digital photograph of the agarose gels depicting hybridization of probe and targets.	81
Figure 5.6	(a) Absorption and emission spectra of 1 mM DAPBA and (b) standard curve of DAPBA.	81
Figure 5.7	Fluorescence intensity profiles of DAPBA.	83
Figure 5.8	B 1 <i>s</i> narrow scan spectra of Fe ₃ O ₄ @Au core-shell nanostructures after hybridization with cDNA (a) and cRNA (b) at 50 nM concentration, followed by DAPBA incubation.	84
Figure 5.9	Fluorescence intensity profiles in the sensing study performed by varying the DAPBA concentration from 25 nM to 200 nM.	84
Figure 5.10	Reversibility studies of DAPBA at pH 3.0 (using citrate buffer): (a) Initial DAPBA binding at pH 8.5, followed by desorption at pH 3.0 and (b) initial DAPBA binding at pH 3.0, followed by desorption at pH 3.0.	84
Figure 5.11	Digital photograph of the agarose gels depicting hybridization of probe and targets, followed by DAPBA incubation.	85
Figure 5.12	Plausible boronic acid-mediated bridging of the two different dsDNAs.	87
Figure 6.1	(a). SDS-PAGE of lipase induction from <i>B. liceniformis</i> using different inducers (b) SDS-PAGE of purified NL	99
Figure 6.2	Agarose gel of the PCR product of expressed lipase	100
Figure 6.3	(a). Circular dichroism spectral profiles of NL and EL. (b). CD	101

	spectra of native and expressed lipases analyzed using BeStSel online tool.	
Figure 6.4	XPS survey and narrow scan spectra of commercial Fe ₃ O ₄ and its surface derivatized products.	103
Figure 6.5	Composite FE-SEM images of commercial magnetite before functionalization, and after derivatization with APTES	104
Figure 6.6	The specific activity analyses of the free and immobilized lipases using the <i>p</i> -NP assay depicting the effects of (a) temperature, and (b) pH.	105
Figure 6.7	Optimization of reaction parameters	106
Figure 6.8	¹ H NMR spectra of RBO, NLB and ELB.	109
Figure 6.9	¹³ C NMR spectra of RBO, NLB and ELB.	109
Figure 6.10	GC profiles of NLB and ELB	111
Figure 6.11	(a) TGA, and (b, c) rheological behaviour of ELB in comparison with RBO.	112
Figure 6.12	(a) Recyclability studies up to 8 cycles using both NL and EL anchored over magnetite using three different immobilization approaches with RBO. (b) Comparative biodiesel production with sunflower and olive oils using the optimal Fe ₃ O ₄ @BSA@EL catalyst up to 8 cycles.	113
Figure 6.13	XPS survey scan and narrow scan spectra of immobilized catalysts before subjecting to the recyclability	114

List of Abbreviations

Ag NPs	Silver nanoparticles
APTES	(3-aminopropyl)triethoxysilane
ASO	Antisense oligonucleotide
Au NPs	Gold nanoparticles
BSA	Bovine serum albumin
CD	Circular dichroism
CFU	Colony forming units
DAPBA	3-dansylaminophenylboronic acid
DLS	Dynamic light scattering
DMEM	Dulbecco's modified Eagle's medium
DMSO	Dimethyl sulfoxide
DNA	Deoxyribose nucleic acid
DTT	1, 4-dithiothreitol
EDC	1-(3-(dimethylamino)propyl)-3-ethylcarbodiimide hydrochloride
EDS	Energy dispersive spectroscopy
EDTA	Ethylenediaminetetraacetic acid
EL	Expressed lipase
ELB	Expressed lipase Biodiesel
EtBr	Ethidium bromide
FAME	Fatty acid methyl ester
FBS	Fetal bovine serum
FDA	Food and drug administration
FE-SEM	Field-emission scanning electron microscopy
GC	Gas chromatography
HCR	Hybridization chain reaction
HCV	Hepatitis C virus
HIV	Human immunodeficiency virus
LAMP	Loop-mediated isothermal amplification
LB	Luria bertani
MBP	Maltose binding protein
MNPs	Magnetite nanoparticles
MRI	Magnetic resonance imaging
MTCC	Microbial type culture collection
MTT	3-(4,5-dimethylthiazol-2-yl)-2,5-diphenyltetrazolium bromide
NAT	Nucleic acid tests
NHS	N-hydroxysuccinimide

NL	Native lipase
NLB	Native lipase biodiesel
NMR	Nuclear magnetic resonance
NPs	Nanoparticles
OD	Optical density
PAGE	Polyacrylamide gel electrophoresis
PBS	Phosphate buffered saline
PCL	Poly(ϵ -caprolactone)
PCR	Polymerase chain reaction
PMSF	Phenylmethylsulfonyl fluoride
PPB	Parts per billion
PPM	Parts per billion
RBO	Rice bran oil
RCA	Rolling circle amplification
RNA	Ribose nucleic acid
RPM	Rotations per minute
RT-PCR	Reverse transcription-polymerase chain reaction
SDS-PAGE	Sodium dodecyl sulfate-polyacrylamide gel electrophoresis.
SFO	Sunflower oil
SPR	Surface plasmon resonance
STEM	Scanning electron tunneling microscopy
ToABr	Tetraoctylammonium bromide
XPS	X-ray photoelectron spectroscopy

Chapter 1

Surface Derivatization of Polymer/Nanoparticles for Diverse Biological Applications

1.1 General Introduction

The use of biopolymers and nanoparticles (NPs) in the biomedical, food and energy sectors has expanded significantly [1]. Biopolymers possess low toxicity and high stability. The wide availability of polymers allows making a choice that takes into account the desired properties, depending on the potential application, such as appropriate porosity of the structure [2], wettability [3], chemical and biological stability [4], mechanical, and thermal resistance [5], as well as biocompatibility [6] or biodegradation [7]. Among polymers, poly(ϵ -caprolactone) (PCL) is a biodegradable polymer broadly utilized in the fabrication of films and frameworks for different biomedical applications [8]. On the other hand, the nanoparticles with their small size possess strong optical [9], emission properties [10], and have high electron density [11] (e.g., Ag and Au) or magnetic moments [12] (iron oxide nanoparticles). The large surface area of nanoparticles provides enhanced opportunities for interaction with biomolecules [13]. Silver nanoparticles (Ag NPs) show excellent antibacterial activity. Under physiological conditions, silver ions can leach out, interact with the bacterial cell wall and destroy the bacterial envelope [14]. Gold nanoparticles (Au NPs) offer both diagnostic benefits and treatment options in biomedicine because of their optical properties [15]. Magnetite nanoparticle (MNPs) based biosensors have been very successful due to their unique property of magnetic separation [16]. Magnetic probes can be used to detect the analytes in biological samples even at low concentrations [17]. Their large surface area also supports the active site of the reactants and their easy separation of such catalysts [18].

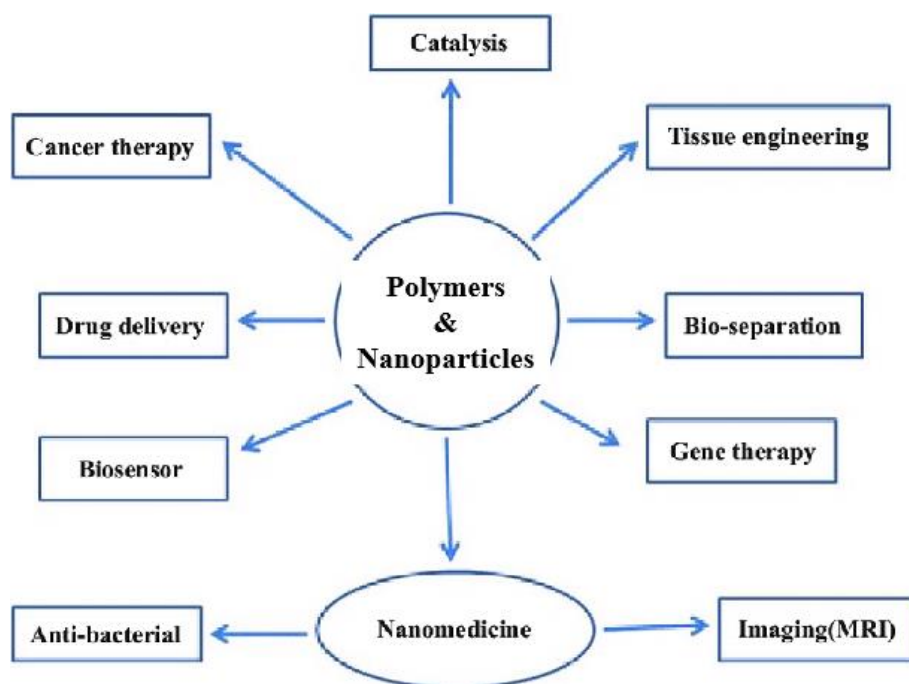


Fig. 1.1 Applications of biopolymers and nanoparticles.

However, in order to achieve desired functions and superior activity, these substances must be modified [19]. Surface modification of nanoparticles with organic and inorganic compounds results in improved physicochemical properties [20][21][22] exhibit unique. For nearly a century, researchers have made significant efforts to bring new properties to materials. Surface modification of materials is now, more than ever, an exciting research topic with numerous promising biological applications. Depending on the type and nature of the material support, various techniques were developed. Surface modification via chemical coating is a promising method for achieving well-defined properties such as stability, biocompatibility, resistance, antibacterial activity, hydrophobicity, and so on [23], [24]. The race against time to develop such materials is due to the urgent need to expedite diagnoses, to prevent the development of diseases—particularly diseases caused by opportunistic pathogens such as bacteria and to pursue the goal of sustainable energy approaches that are benign by design.

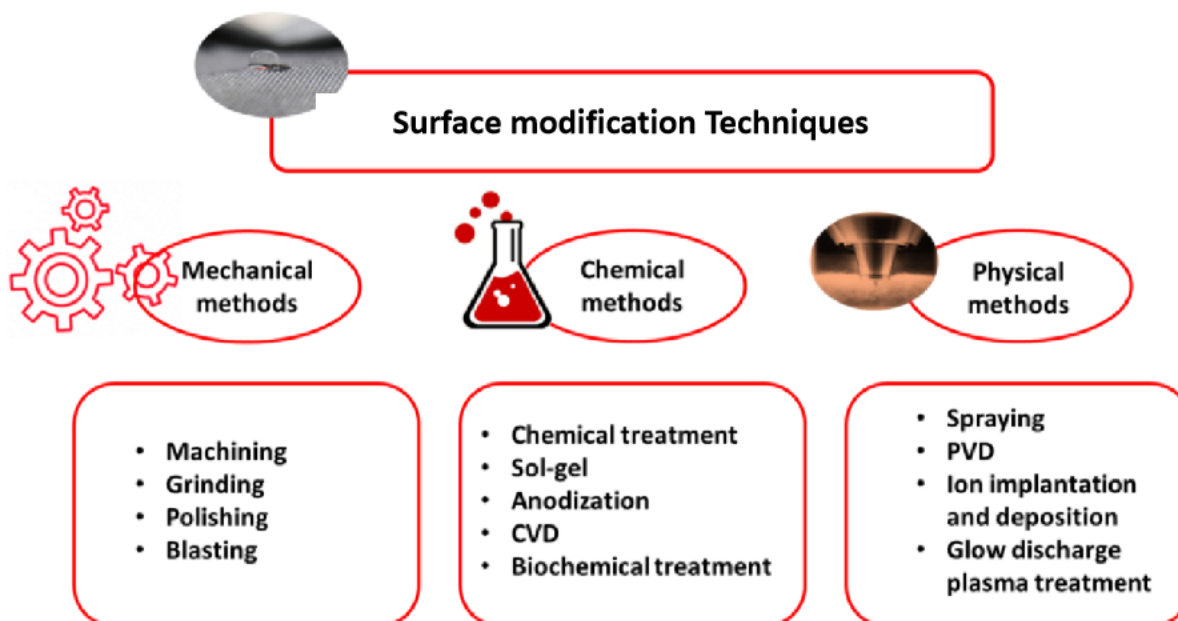


Figure 1.2 Surface modification techniques.

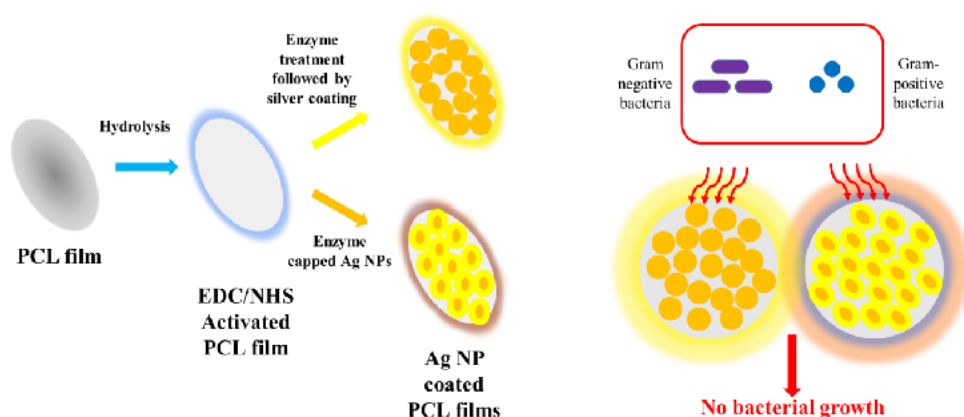
1.2 Review of Literature

1.2.1 Surface functionalization of polymer for disinfection performance

Biopolymers are widely used in biomedical equipment and food packaging due to their low cost, high stability, and biodegradability. However, most polymers lack the inherent antibacterial properties essential to prevent infection and food contamination [5]. In addition, the hydrophobicity of the polymer limits its interaction with mammalian cell membranes, reducing biocompatibility [6]. Plastic materials with unique antibacterial properties are made by polymerizing or copolymerizing new monomers or by chemically modifying and blending polymers. However, this approach often results in unacceptably high costs, changes in bulk properties, and inadequate thermal stability, resulting in non-functional materials. Recently, attempts have been made to mix inorganic or organic substances such as metals and antibiotics into the polymer matrix [7]. Among the additives used, silver (Ag) showed a stronger bactericidal effect [25]. In contrast to antibiotics and chemicals, silver nanoparticles (Ag NPs) do not cause microbial resistance and are active at low concentrations [26]. Though Ag NPs

can act as an antibacterial agent, aggregation without a suitable capping agent strongly inhibits antibacterial activity [27]. This problem can be solved by applying the appropriate capping agent to Ag NPs [28]. Various synthetic natural biopolymers and surfactants are used as capping agents for Ag NPs [29].

Among the biologically derived molecules, enzymes are considered to be more eco-friendly and biocompatible capping agents [30]. Enzymes as capping agents have the added benefit of enhancing the interaction of nanoparticles with bacterial surfaces and supporting controlled degradation of the polymer [31]. Therefore, polymers can be combined with enzyme-stabilized Ag NPs to improve the bactericidal properties of the polymers [32]. These capped nanoparticles can change wettability by altering intramolecular interactions and improving hydrophilicity by altering surface morphology [33]. Poly(ϵ -caprolactone) is a Food and Drug Administration (FDA) authorized, biocompatible and bioresorbable polymer for different biomedical applications. Lipases derived from probiotic sources are considered safe and could be employed in *in vivo* implants. In this study, we propose to use a probiotic-derived enzyme-mediated silver coating over PCL film and check its antimicrobial efficacy and biocompatibility (see Scheme 1 below).



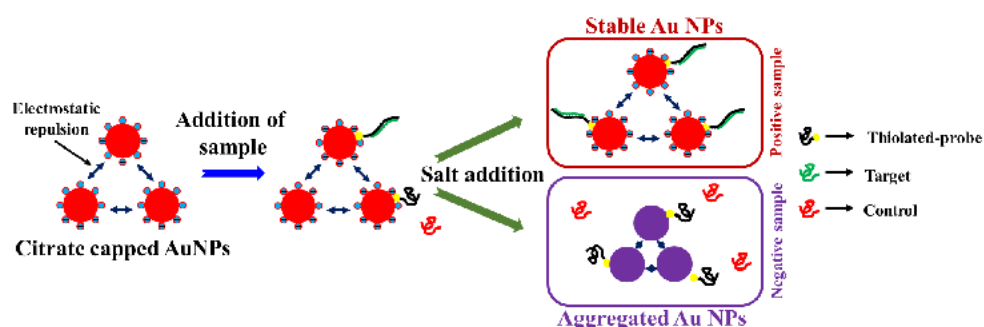
Scheme 1: Pictorial representation of the strategies for surface derivatization of PCL films with silver.

1.2.2 Nanoparticle mediated bio sensing of Oligonucleotides

Au NPs mediated Bio sensing of Oligonucleotides

Nanoscale biosensors have been used to detect and diagnose various bacterial, viral infections, and diseases including cancer [34]. These sensors allow rapid diagnosis and better tracking of the condition. Gold nanoparticles (Au NPs) are of great interest in the biological world. Mirkin and co-workers pioneering work on ligating thiol-labelled DNA to Au NPs [35] have opened up new avenues for bio sensing research. Since then, Au NPs have been used in several methods, including colorimetric, spectrophotometric, electrochemical, surface-enhanced Raman scattering, and piezoelectricity-based bio sensing. Quantitative binding of thiol-labelled probes to Au NPs is critical to the success of the assay. The surface of citrate-capped Au NPs showed a zeta potential of -30 ± 10 mV. The phosphate unit of the DNA backbone is also negatively charged and causes charge repulsions when attempted to bind to the surface of Au NPs capped with citric acid. A salt-aging [36] approach has allowed the thiolated DNA to be attached to the Au NP surface. NaCl minimizes the charge repulsions between the citrate molecules on the Au NPs and phosphate units of DNA. The salting procedure, on the other hand, takes 24 to 48 h for optimal binding. To enable rapid and high thiol conjugation, the pH of Au NPs can be adjusted using citrate buffer [37], or by rapid dehydration with butanol (INDEBT) [38]. The approach using citrate buffer is simple and attractive. However, the effectiveness of these approaches with low DNA to Au NP ratios has not been investigated. RNA is crucial in various biological processes and the manifestation of disease symptoms [39]. SPR sensor technology is most commonly used to study the interactions of high molecular weight analytists. Low molecular weight analytes such as RNA are still difficult to detect due to subtle changes in the index of refraction [40]. In such situations, extrinsic labels should be used to enhance the SPR signal. To detect a particular nucleic acid, traditionally, Au NPs must be modified with unique nucleic acids with complementary sequences, requiring frequent optimizations, which is time-

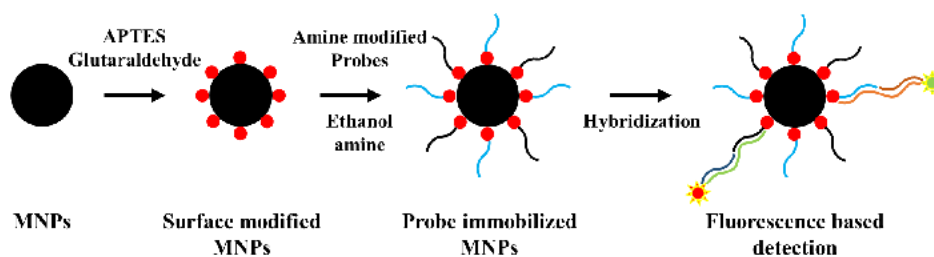
consuming and costly. Therefore, developing a universal nanoparticle-based signal amplification approach for RNA detection is necessary. Specific reagents are widely used in sensor technology, chromatography, and biological research because of their ability to bind to cis-diol groups specifically [41]. Most studies with such compounds focus on the purification and detection of sugars or glycoproteins. Despite their wide applications, they have not been explored in nucleic acid identification. These reagents prefer RNA over DNA because they can preferentially interact with cis-diol groups in RNA. We propose to produce such modified Au NPs to amplify RNA signals in bio sensing selectively. A schematic of the bio sensing is using gold nanoparticles is depicted below in the Scheme 2 below.



Scheme 2: Representation on the mechanism of the sensing strategy using Au NPs

MNPs mediated biosensing of Oligonucleotides

MNPs are known to display super paramagnetic properties, having potential applications in product separation, drug delivery, imaging (MRI), and bio sensing [42]. Using magnetic separation of MNPs, it is possible to concentrate the analytes before the detection [42]. In bio sensing applications, the interference or noise during signal capturing is limited when magnetic labels were used [43]. In this current work, we aim to develop sensing strategy by combining magnetite NPs with a fluorescence-based detection assay. The surface derivatization of magnetite NPs with the probe DNA complementary to the target, subsequent hybridization and fluorescent detection is presented in the Scheme 3 below.

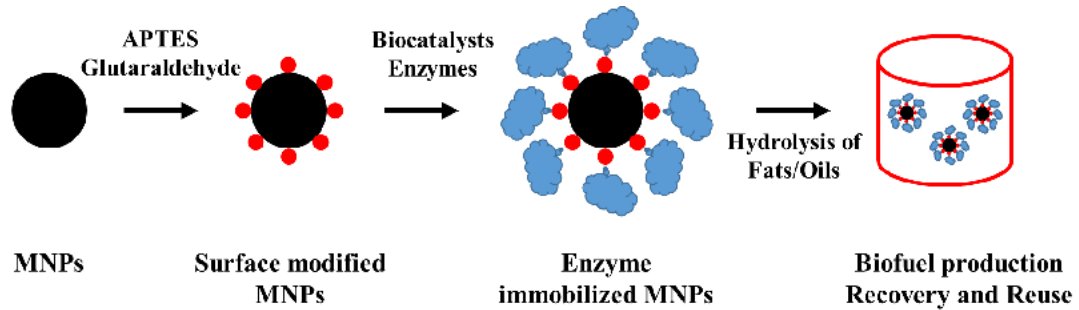


Scheme 3: Representation on the strategy for surface derivatization and mechanism of biosensing using MNPs.

1.2.3 Biofuel generation through probiotic derived immobilized enzymes

A significant percentage of food is wasted worldwide, causing an economic burden and a global problem [44]. Food waste is rich in carbohydrates, proteins, and lipids, so it has the potential to be converted into value-added products [45]. Traditional approaches often use chemical catalysts that can esterify lipids in the presence of alcohol to produce biodiesel [46]. However, they often lead to unwanted by-products. Microbial-derived enzymes, due to their specificity, are superior to traditional chemical catalysts in recycling waste streams with no harmful by-product generation. Lipases are ubiquitous biocatalysts that catalyze triacylglycerol hydrolysis to produce free fatty acids diacylglycerol, monoacylglycerol, and glycerol [47]. Purified lipases have high catalytic efficiency, but challenges include the high cost of purification, low stability, and recovery under industrial conditions [47]. Increased enzyme activity has been achieved in commercial applications by immobilizing them on hydrophobic surfaces or by packing them onto porous and non-porous carriers, magnetic nanoparticles, carbon nanotubes, graphene oxide, organic metal frameworks, and polymers [48], [49]. MNPs are increasingly being used as carriers because of their large surface area and chemical changeability. Its high mechanical stability across a wide range of temperatures and pH decreased diffusion limitation, and ease of separation using magnets allowed it to be used in biological operations. Based on the literature reports, the immobilization of catalytically active lipases derived from thermophilic

bacteria on MNPs will be attempted in the current study for biofuel generation, enhancing the enzyme stability and activity (see Scheme 4 below).



Scheme 4: Representation on the strategy for surface derivatization and mechanism of biofuel generation using MNPs.

1.3 Gaps in existing research

- Polymer coatings with Ag NPs alone might not be stable for long time and there is a need for improvement.
- Enzymes from probiotic source can be an alternative for controlled degradation and yet be biocompatible.
- By using probiotic lipase stabilized Ag NPs and subsequent immobilization may give a multifunctional value to the derived polymer.
- Rapid and effective thiol tagging over Au NPs at low concentrations of DNA probes for bio sensing of oligonucleotides remains unexplored.
- To explore of the interaction of boronic acid with 3' OH groups of DNA, especially in free floating sensing strategies.
- To develop a simultaneous dual-probe sensing strategy by combining magnetite NPs with a fluorescence-based detection assay.
- Enzyme immobilized on MNPs for biofuel production for increased reactivity, stability, and better recovery will be further explored.

1.4 Objectives

- I. Surface functionalization of polymer for disinfection performance
- II. Bio sensing of oligonucleotides
- III. Biofuel generation through immobilized enzymes

Chapter 2

***Lactobacillus amylovorus* derived lipase-mediated silver derivatization over poly(ϵ -caprolactone) towards antimicrobial coatings**

2.1 Introduction

Antimicrobial coatings over frequently contacted surfaces have garnered significant attention for combating the spread of infections [50]–[52]. Antimicrobial coatings are also preferred in implantable scaffolds coatings over the food and packaging sector [53], [54]. The use of antibiotics is one of the earliest adopted strategies, penicillin was used in World War II to confine the spread of pathogenesis in the soldiers. Several synthetic chemicals, such as pesticides, fungicides, nematicides, etc., were extensively used in healthcare and agricultural purposes [55]–[57]. Since synthetic chemicals and antibiotics lead to drug-resistant microbes and adverse environmental effects, there is a surge in developing non-toxic and natural component-derived antimicrobial agents for such applications [58]–[61]. These agents are immobilized or embedded in polymers and studied for their antimicrobial efficacy [62], [63].

In recent years, metal nanoparticle-based biotechnology has positively impacted various bio- and pharmaceutical applications such as anticancer, antiparasitic, bactericidal, fungicidal, etc. [64]–[68]. Several factors govern the biological activity of the inorganic nanoparticles, including size distribution, morphology, surface charge, surface chemistry, capping agents, etc. [69]–[74]. Among the metals used as antimicrobial agents, silver is the preferred element besides gold, copper, and zinc [75]–[77]. Silver is effective at a much lower dose (typically in ppm to ppb level of concentration) than the other metals, it does not cause resistance in microbes [26], unlike antibiotics or synthetic chemicals. Due to this favourable attribute, silver-based coatings are highly preferred in wound dressing materials, food storage containers, paints, cosmetics, etc. [78]–[80]. In all these applications, nanoscopic silver is preferred owing to the high surface-to-volume ratio and thereby provides maximum benefit from the lower concentration of the metal [81], [82]. For stabilizing the silver nanoparticles (Ag NPs), surface-active agents such as citrate, polyphenols, sodium borohydride, and alkyl

thiols are used as the capping ligands. The Ag NPs are also stabilized or embedded in polymers like poly-(N-vinyl-2-pyrrolidone), polyvinyl alcohol, biopolymers, etc. [29]. In recent years, there has been a significant surge in utilizing biogenically synthesized noble metal nanoparticles for antimicrobial applications [60], [75]. Gopinath *et al.* reported the biogenic synthesis of Ag NPs using soil-derived *Pseudomonas putida* and its cell-free supernatant solution [61]. The obtained nanoparticles were found to show high antimicrobial efficacy over several bacterial pathogens. Karatoprak *et al.* synthesized Ag NPs using root extracts from *Pelargonium endlicherianum* Fenzl and showed their high bactericidal efficacy [83]. Shivakumar *et al.* studied the synthesis of Ag NPs using the phyto-constituents from the pre-hydrolyzed liquor of *Eucalyptus* wood and demonstrated the antibacterial and antifungal efficacy of the nanoparticles [84]. Ganesan *et al.* synthesized Au NPs using the extract from the *Acorus calamus* rhizome and attributed the reduction of chloroauric acid to the amine groups in the protein [85]. Cui *et al.* have demonstrated the sustained antimicrobial activity of silver nanoparticles deposited over silver, copper, and zinc-ternary ion-exchanged zeolite as an additive in paint coatings [51].

Poly(ϵ -caprolactone) (PCL) is a food and drug administration (FDA) approved biocompatible and bioresorbable polymer for several biomedical applications such as root canal fillings, sutures, controlled drug delivery systems, and tissue engineering implants [19], [86]–[91]. Due to the high potential of this biomaterial, there is considerable interest in making the polymer antimicrobial to enhance its applicability [92], [93]. Recently, there has been a growing demand for sustained antimicrobial activity for a prolonged period, which is desirable for implant-related applications [94], [95]. Several strategies have been adapted to render the polymer with antimicrobial properties that include loading the matrix with antibiotics [96], terpenoids [97], natural components like grapefruit seed extract [98], copper oxide nanoparticles [5], and Ag NPs [99]. Also, strategies to develop amorphous solid dispersions

have gained momentum, in which a bioactive component is incorporated in the PCL matrix to modulate the mechanical properties and drug release kinetics [100]. Surface functionalization of PCL with silver and bacteriophage has also been reported to enhance antimicrobial properties [93], [101]. In the current work, we prepared *Lactobacillus amylovorus*-derived lipase-mediated silver coating over PCL and studied their antimicrobial efficacy. It is known that the lipases derived from the probiotic sources are highly benign therefore, may be used in *in vivo* implants. Hence, the lipase derived from probiotic *L. amylovorus* is chosen as a mediator to functionalize the PCL surfaces with silver to render sustained antimicrobial properties.

2.2 Methodology

2.2.1 Materials

AgNO₃, NaBH₄, 1-(3-(dimethylamino)propyl)-3-ethylcarbodiimide hydrochloride (EDC), N-hydroxysuccinimide (NHS), PCL pellets (M_w = 45,000 Da), phenylmethylsulfonyl fluoride (PMSF), 3-(4,5-dimethylthiazol-2-yl)-2,5-diphenyltetrazolium bromide (MTT), chloroform, dimethyl sulfoxide (DMSO), and acetone were purchased from Sigma-Aldrich and used as received. *Lactobacillus amylovorus* (MTCC 8129) was procured from IMTECH, Chandigarh, India. Luria Bertani (LB) broth and agar required to plate the microbes for studying the antimicrobial efficacy of the silver-coated films were purchased from Himedia Chemicals, India Ltd. The reagents required for the MTT assay, fetal bovine serum (FBS) and antimycotic solution, were procured from Himedia, India. Dulbecco's modified Eagle's medium (DMEM) was purchased from Invitrogen, USA.

2.2.2 PCL film casting and alkaline hydrolysis

The PCL films used in this study were prepared using the solvent casting method. Briefly, a 1 w/v % of chloroform solution dissolved with the PCL pellets was poured into a glass petri dish and allowed to dry overnight. The obtained films were then subjected to alkaline hydrolysis at room temperature with 5 N NaOH solution for two time points, such as 2 h and 4 h. The hydrolyzed films were thoroughly washed with milliQ water followed by diluted HCl solution, and finally with milliQ water.

2.2.3 EDC/NHS-activation

The carboxylic acid groups obtained on the PCL film surface through hydrolysis were activated using a classical EDC/NHS amide coupling agent. In a typical experiment, about 4 cm × 4 cm size hydrolyzed PCL films were activated by immersing in a 10 mL solution containing 45 mM EDC and 15 mM NHS for 2 h at room temperature. The films were washed thoroughly with PBS buffer and immediately utilized for further surface derivatization experiments. Two types of surface derivatization were carried out in this work: (1) Immobilizing lipase-capped Ag NPs over the EDC/NHS activated PCL films, and (2) immobilizing the lipase over the EDC/NHS-activated PCL films in the first step followed by deposition of silver using the dip-coating method.

2.2.4 Lipase production from *L. amylovorus*

The production of extracellular lipase from *L. amylovorus* was performed as per the following protocol. The lipase production was carried out in 250 mL Erlenmeyer flasks, each containing 50 mL of a medium composed of peptone (0.5 %), yeast extract (0.3 %), NaCl (0.25 %), MgSO₄ (0.05 %) and 1 % olive oil. The bacterial inoculum added to the substrate was 10⁸ CFU/mL in the ratio of 1:1. After incubation for 48 h, the cell-free supernatant was obtained

by centrifugation at 7860 RPM at 4 °C for 20 min, and the extracellular lipase activity of the fermented broth was determined. The total protein content was estimated by Lowry's method using Bovine serum albumin as the standard. The lipase assay was performed spectrophotometrically using *p*-nitrophenyl palmitate as the substrate. Briefly, 2.5 mL of 420 μM *p*-nitrophenyl palmitate, 2.5 mL of 0.1 M Tris-HCl (pH 8.2), and 1 mL of enzyme solution were mixed and incubated in a water bath at 37 °C for 10 min. The *p*-nitrophenol was liberated from *p*-nitrophenyl palmitate by lipase-mediated hydrolysis imparting a yellow color to the reaction mixture. After incubation, the absorbance was measured at 410 nm, which was compared against a control. The supernatant was added with chilled acetone to precipitate the protein as per the literature protocol [102]. The obtained lipase lysate was used for further studies.

2.2.5 Synthesis of lipase-capped Ag NPs

The lipase-capped Ag NPs were synthesized in two different compositions that vary in the concentration of the precursor, AgNO₃ [60]. In a typical synthesis, the AgNO₃ solutions having a concentration of 0.6 mM and 1.0 mM were added with lipase derived from *L. amylovorus* such that the final concentration of the enzyme is 50 μg mL⁻¹. The resultant solution was kept stirring at 500 RPM in a beaker, to which freshly prepared NaBH₄ solution (3.2 equivalent with respect to AgNO₃) was quickly added, and the stirring was continued for another 10 min. The Ag NPs thus synthesized were subjected to dialysis for 2 h using a cellulose membrane having a 10 kDa cut off to remove the excess of NaBH₄ and any reaction byproducts. The lipase-capped Ag NPs thus synthesized were then used for subsequent covalent immobilization over EDC/NHS-activated PCL films.

2.2.6 Immobilization of lipase-capped Ag NPs over PCL films

The EDC/NHS-activated PCL films were separately reacted by immersing them into lipase-capped Ag NPs having different concentrations. The immobilization reaction was performed overnight at room temperature and washed thoroughly with PBS buffer. The obtained films were then dried by purging with nitrogen gas and used for further studies. The two samples prepared by immobilizing Ag NPs synthesized using 0.6 mM and 1.0 mM AgNO₃ solutions were labeled as PCL-0.6-Ag-imm and PCL-1.0-Ag-imm, respectively.

2.2.7 Ag deposition over PCL films through dip-coating method

The EDC/NHS-activated films were incubated at room temperature overnight with 100 µg mL⁻¹ solution of lipase derived from *L. amylovorus*. The films immobilized with lipase were washed with PBS buffer and with milliQ water. The lipase-immobilized PCL films were then used for surface depositing of silver using the dip-coating method. Briefly, the lipase immobilized PCL films were sequentially dipped into 1 mM AgNO₃ solution for 10 min and 5 mM NaBH₄ solution for 5 min. After each dipping, the films were gently washed with milliQ water before dipping into the next reagent solution. Two different compositions, such as 5-times dipped, and 10-times dipped PCL films, were prepared, dried by purging with nitrogen gas, and then used for further studies. The films prepared by 5-times and 10-times dipping were labelled PCL-5-Ag-dip and PCL-10-Ag-dip, respectively.

2.2.8 Antimicrobial studies

The antimicrobial efficacy of the surface-derivatized PCL films was performed as follows: Initially, in a 100 mL conical flask, 0.9 % NaCl (upto 5 mL), *E. coli* culture with 10⁷ – 10⁸ cells/mL were taken [57]. The silver-coated PCL films cut into 4 cm² were added to this solution and incubated for various time intervals such as 2, 3, 4, 6, 8, and 24 h at 37 °C, 60

RPM. After each time interval, 10 μL of the culture was mixed with 20 μL of water, and plated in LB agar plates and incubated at 37 °C overnight.

2.2.9 Cytotoxicity assay

The cytotoxicity of the PCL films, derivatized with lipase-mediated silver coating was tested on mouse fibroblast cell line (SNL 76/7) by MTT assay [61]. The films were cut and carefully placed in a 12-well plate to cover the culture's surface (3.5 cm^2) and seeded with 10^5 cells per well in DMEM supplemented with 10 % FBS and 1X antimycotic solution. The plates were incubated at 37 °C in a CO_2 incubator with 5% CO_2 for 24 h. After incubation, the cells were washed with 1X PBS and, MTT solution was added at a final concentration of 0.5 mg/mL in the culture media and incubated further for 4 h. The medium was removed, cells were washed with PBS and 500 μL of DMSO was added to the wells and incubated for 1 h in the dark. The absorbance of the solution was read at 570 nm by using a microplate reader. The cell viability was calculated as shown below..

$$\% \text{ Cell Viability} = (OD \text{ Sample} \div OD \text{ Control}) \times 100$$

2.2.10 Characterization

The surface elemental composition of the pristine and surface-derivatized PCL films was characterized using X-ray photoelectron spectroscopy (K-alpha instrument, ThermoFisher) equipped with Al K_α monochromated X-ray source. A flood gun was used to prevent the surface charging of the PCL films. The water contact angle of the PCL films was obtained using the Theta Flex contact angle goniometer (Biolin Scientific). Field-emission scanning electron microscopy (FE-SEM) from FEI (model: Apreo S) was employed to image the morphology of pristine and surface-derivatized PCL films. In the same instrument, scanning electron tunneling microscopy (STEM) mode was employed to image the as-synthesized Ag

NPs at an acceleration voltage of 30 kV. JASCO V-650 UV-vis spectrophotometer was used to confirm the synthesis of Ag NPs. SpectraMax[®] iD3 from Molecular Devices, USA was used to record the microplate absorbance values used in the MTT assay.

2.3 Results and Discussions

2.3.1 PCL surface derivatization strategy

Two surface derivatization strategies depicted in **Figure 2.1** have been employed in the current study to immobilize silver onto the PCL films.

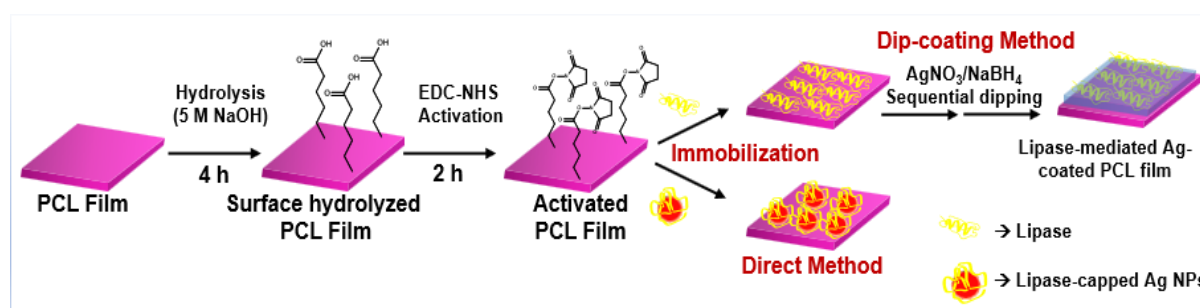


Figure 2.1 Pictorial representation depicting the strategies employed in this study for surface derivatization of PCL films with silver.

In the first strategy, Ag NPs have been synthesized in the first step using lipase derived from *L. amylovorus* as the surface stabilizing agent. Using the amine groups present in the protein; the lipase-capped Ag NPs have been immobilized over the EDC/NHS-activated PCL films in the second step. Two different compositions of Ag NPs that vary in the initial concentration of AgNO₃ (0.6 mM and 1.0 mM) were separately synthesized (**Figure 2.2**) and used for the immobilization. In the second strategy, at first, the lipase derived from the probiotic source was immobilized over the EDC/NHS-activated PCL films. In a subsequent step, the lipase-immobilized PCL films were dipped into an AgNO₃ solution to adsorb the silver precursor over the amine, carboxylic, and thiol groups present in the lipase. The adsorbed AgNO₃ was then

reduced to metallic silver using NaBH_4 . This process was repeated 5 times and 10 times to obtain two compositions of PCL films that were enriched with silver on the surface.

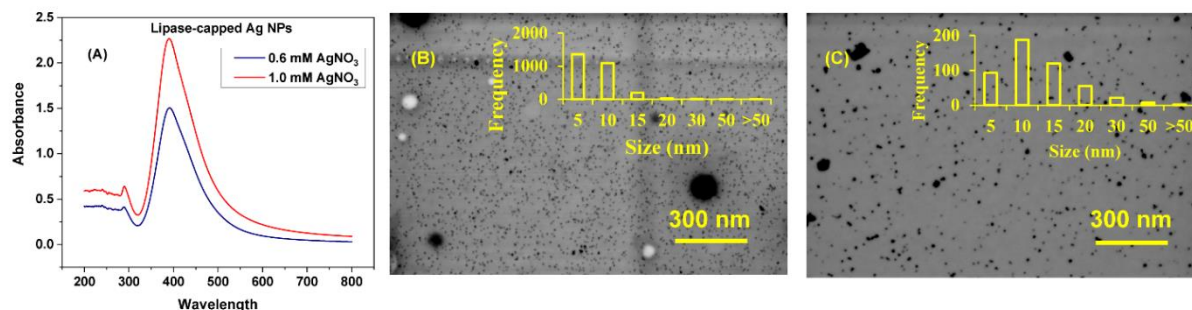


Figure 2.2 (A). UV-visible spectra of 3x diluted 50 $\mu\text{g}/\text{mL}$ lipase-capped Ag NPs synthesized using 0.6 mM and 1.0 mM Ag NO_3 . STEM images of the Ag NPs synthesized using (B) 0.6 mM and (C) 1.0 mM Ag NO_3 , where the latter sample was prepared using 3x diluted solution. The inset in (B) and (C) shows the particle size distribution.

2.3.2 Surface Characterization

For the surface hydrolysis of PCL films using NaOH solution, two time points such as 2 h and 4 h were initially tested using contact angle measurements. The pristine PCL film exhibited a water contact angle of $85 \pm 2^\circ$, while the water contact angles of 2 h and 4 h hydrolyzed samples were found to be $55 \pm 3^\circ$ and $12 \pm 3^\circ$, respectively (**Figure 2.3**). The decrease in the water contact angle indicates increasing hydrophilicity of the PCL film due to surface hydrolysis. Due to the close agreement between our results and those reported in the literature [101], [103], we have chosen the 4 h hydrolyzed PCL films for further studies.



Figure 2.3 Contact angle measurements over (a) pristine, (b) 2 h alkaline hydrolyzed, and (c) 4 h alkaline hydrolyzed PCL films.

XPS has been employed to probe the surface derivatization of the PCL films since it is a powerful surface characterization tool [104]. The *C 1s*, *N 1s*, *O 1s*, and *Ag 3d* narrow scan XPS spectra of various samples have been presented in **Figure 2.4**.

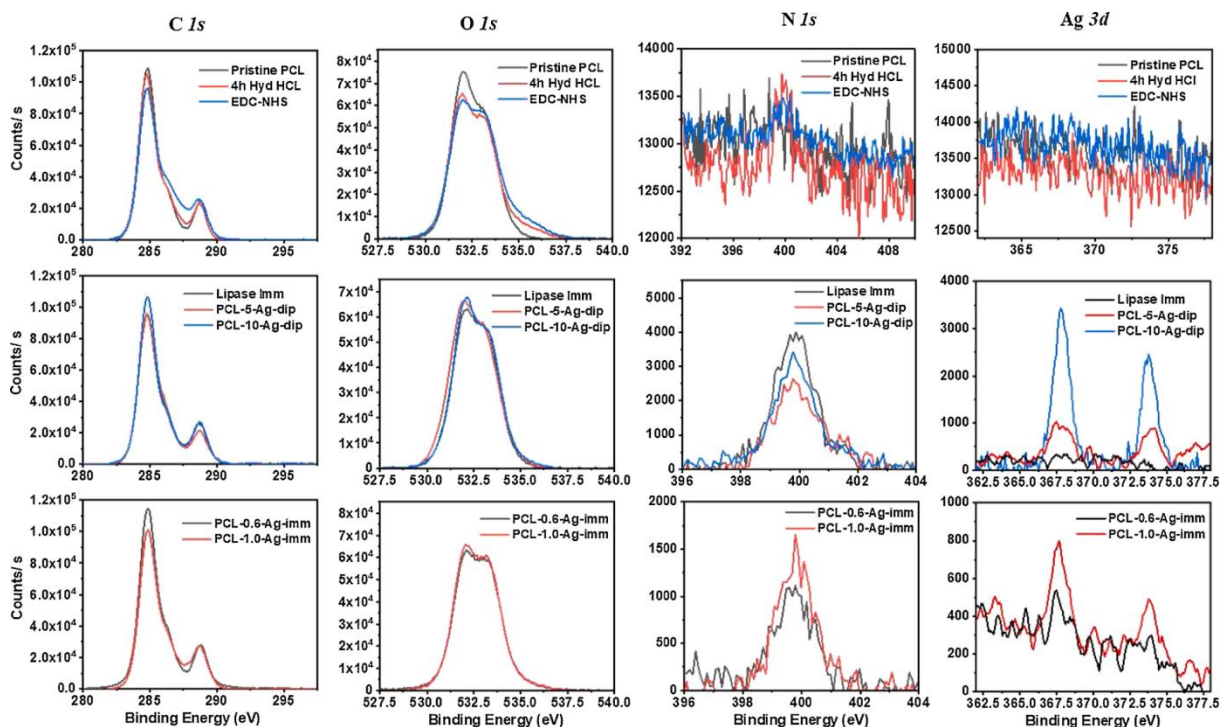


Figure 2.4 *C 1s*, *O 1s*, *N 1s*, and *Ag 3d* XPS narrow scan spectra of pristine, hydrolyzed, EDC/NHS-activated (top row), lipase-immobilized, PCL-5-Ag-dip, PCL-10-Ag-dip (middle row), PCL-0.6-Ag-imm, and PCL-1.0-Ag-imm PCL films (bottom row).

The deconvolution of *C 1s* and *O 1s* narrow scan spectra of the pristine and hydrolyzed PCL films are shown in **Figure 2.5**. The pristine PCL film exhibited the presence of carbon and oxygen elements. The deconvolution of *C 1s* narrow scan spectrum revealed the presence of carbon in the C–C and C–H environments at 284.8 eV. In addition, the characteristic peak corresponding to the carbon present in the ester environment was also observed at 286.4 eV (C–O–C) and 288.8 eV (O–C = O). The *O 1s* narrow scan spectrum of the pristine PCL film exhibited a sharp peak at 532.0 eV along with a shoulder at 533.4 eV, which can be attributed to the carbonyl (–C = O) and ether (C–O–C) oxygens, respectively. In the case of alkaline-mediated hydrolyzed PCL film, the intensity of the peak possessing higher binding energy in

the O 1s narrow scan spectrum was increased, which could be attributed to the surface oxidation of the ester groups.

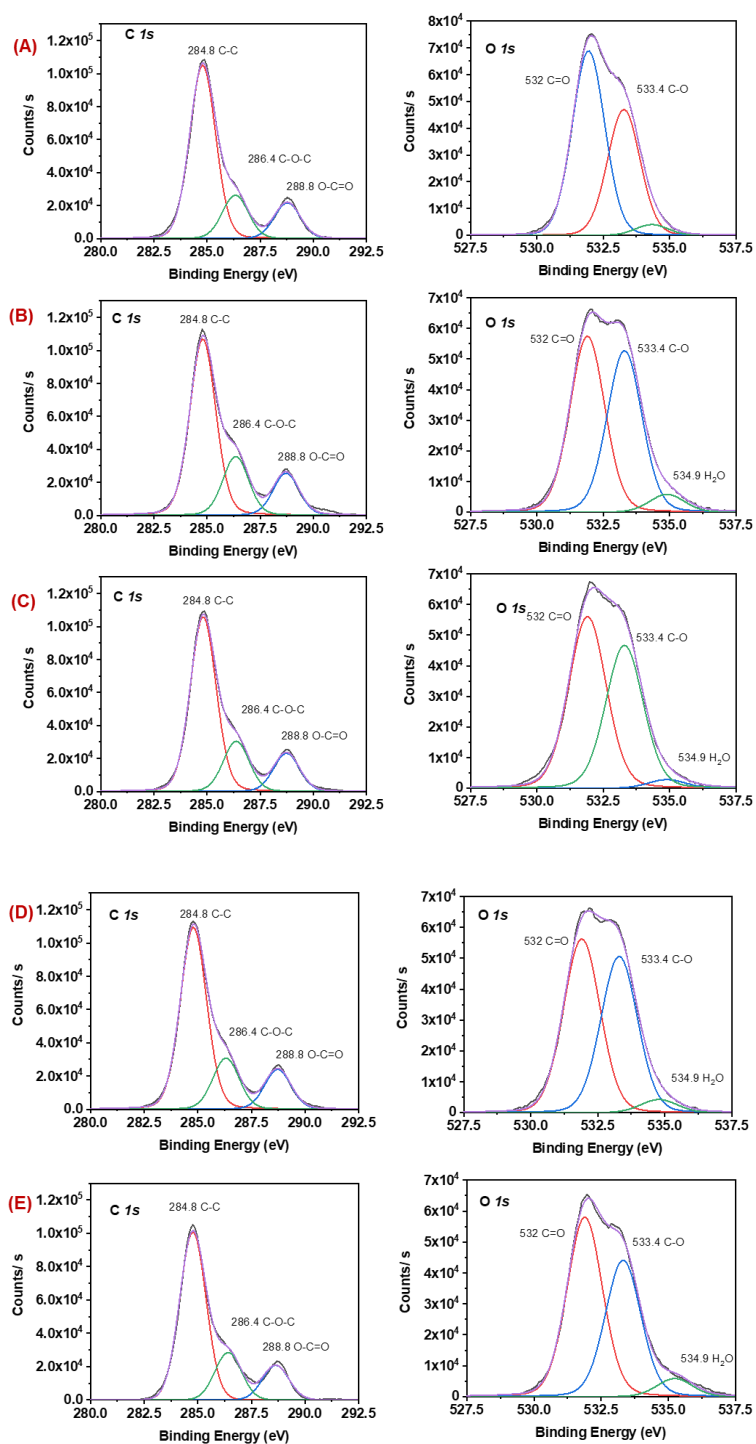


Figure 2.5 C 1s and O 1s narrow scan XPS spectra of pristine PCL film and alkaline-mediated hydrolyzed samples (before and after treatment with dilute HCl). The sample codes (A), (B), (C), (D), and (E) represent the C 1s and O 1s narrow scan spectra in each row corresponding to the samples pristine PCL, 2 h as-hydrolyzed, 2 h hydrolyzed – after HCl treatment, 4 h as-hydrolyzed, and 4 h hydrolyzed – after HCl treatment, respectively.

The NaOH-mediated hydrolysis is expected to yield sodium carboxylate on the PCL surface, which has been confirmed with the appearance of Na *1s* peak at 1072 eV and a feeble signal at 497 eV corresponding to the sodium Auger peak in the XPS survey scan of 4 h as-hydrolyzed sample **Figure 2.6**. When the hydrolyzed PCL films were rinsed with dilute HCl solution, the characteristic signals of sodium disappeared, thus confirming the protonation of sodium carboxylates. Upon activation of the hydrolyzed films using the amide coupling reagent EDC/NHS, nitrogen was also detected along with carbon and oxygen. This observation has confirmed the successful activation of the surface carboxylic groups by the coupling reagent. The lipase immobilized PCL film also exhibited the presence of nitrogen along with carbon and oxygen, which was confirming the presence of the enzyme on the film surface. In the case of PCL-0.6-Ag-imm and PCL-1.0-Ag-imm, in addition to the elements carbon, oxygen, and nitrogen, silver was also detected. The atomic percentage of silver in PCL-0.6-Ag-imm and PCL-1.0-Ag-imm was found to be 0.01 % and 0.02 %, respectively, which was also revealed in the Ag *3d* narrow scan spectra, wherein the latter was exhibiting higher intensity than the former. The atomic silver content in the PCL-5-Ag-dip and PCL-10-Ag-dip samples was found to be 0.01 % and 0.13 %, respectively. The XPS study has thus confirmed the successful surface derivatization of PCL films with silver through both approaches.

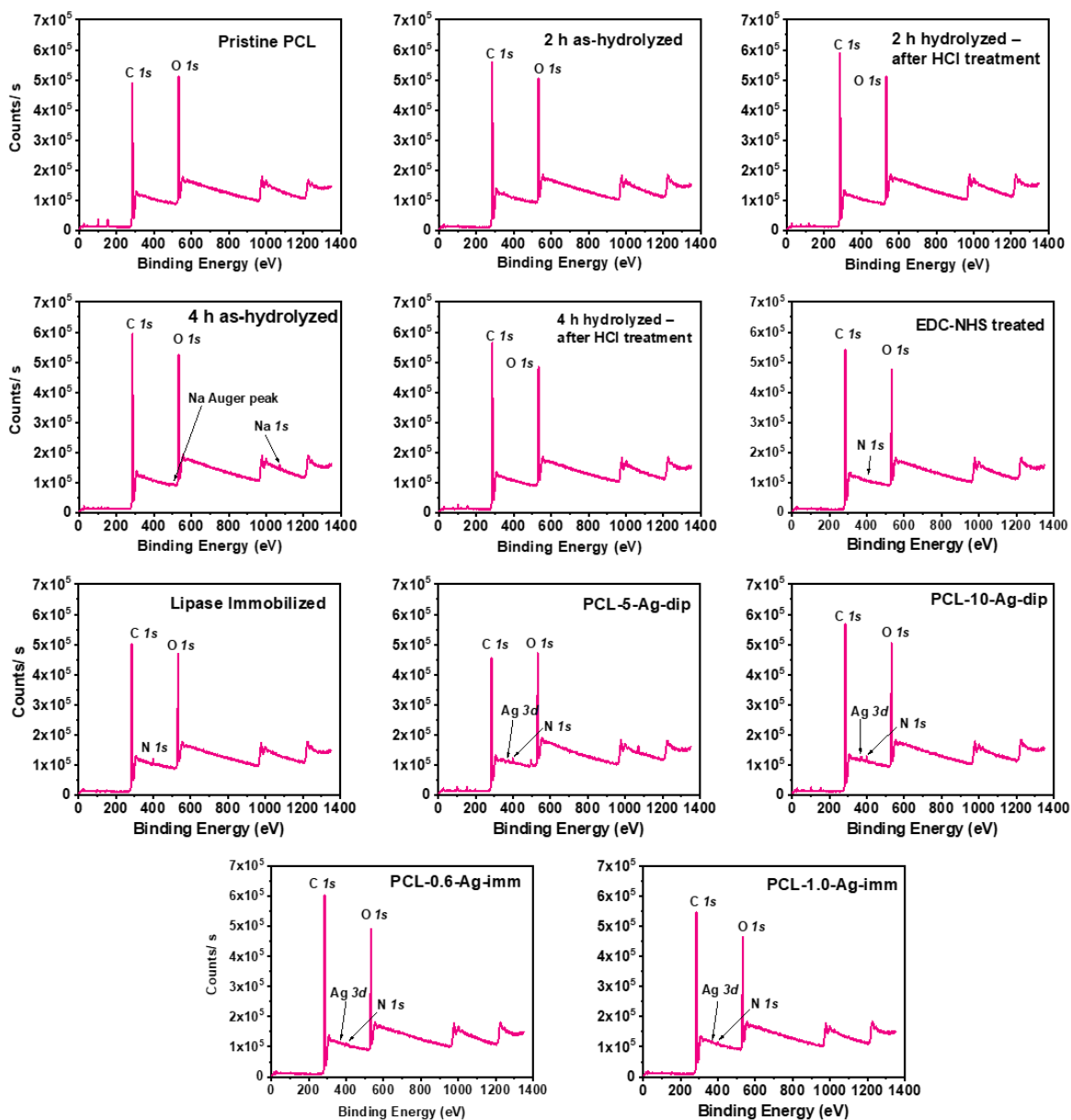


Figure 2.6 XPS survey scan spectra of PCL films subjected to various steps in the surface derivatization process.

FE-SEM was employed to study the surface morphology of the pristine and surface derivatized PCL films, and the results are shown in **Figure 2.7 (i and ii)**. The pristine PCL films were found to exhibit a smooth surface morphology at the macroscopic scale with a micron to nanoscale roughness. The PCL-0.6-Ag-imm and PCL-1.0-Ag-imm samples exhibited similar morphology to that of pristine PCL films on the surface but with a few particulates, presumably the aggregates of Ag NPs. A similar observation was also observed

with PCL-5-Ag-dip, while PCL-10-Ag-dip was found to exhibit a significant amount of bright patches consisting of nanoscopic particulates, which could be attributed to the higher silver loading, as evidenced in XPS as well. These results indicate that the surface derivatization of PCL with silver did not result in a significant change in the surface morphology, except the sample PCL-10-Ag-dip.

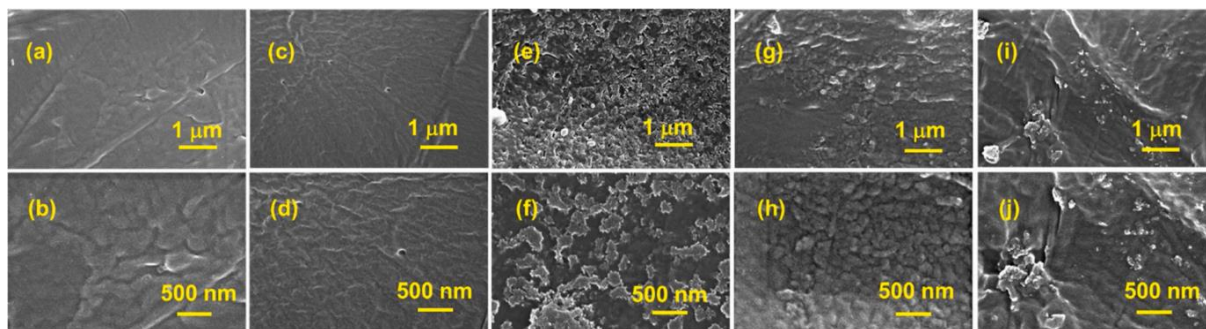


Figure 2.7 (i). FE-SEM images of (a, b) pristine, (c, d) PCL-5-Ag-dip, (e, f) PCL-10-Ag-dip, (g, h) PCL-0.6-Ag-imm, and (i, j) PCL-1.0-Ag-imm PCL films.

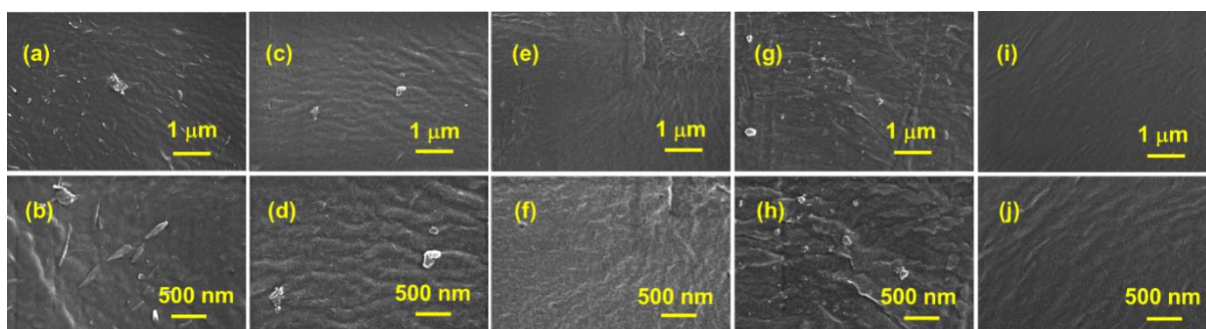


Figure 2.7 (ii). FE-SEM images of (a, b) 2 h as-hydrolyzed, (c, d) 2 h hydrolyzed – after HCl treatment, (e, f) 4 h as-hydrolyzed, (g, h) 4 h hydrolyzed – after HCl treatment, and (i, j) EDC/NHS activated PCL films.

2.3.3 Antimicrobial activity

The antimicrobial efficacy of the silver-coated PCL films obtained by the two strategies has been explored against a gram-negative bacterium *E. coli*, and the results are presented in **Figure 2.8 (i and ii)**. In the control experiment using pristine PCL film, a consistent high bacterial growth was observed even up to 24 h, demonstrating no bactericidal effect from the

untreated film. The PCL-5-Ag-dip and PCL-10-Ag-dip did not exhibit a significant bacterial inhibition even by 8 h; however, they showed complete inhibition by 24 h. On the other hand, the PCL-0.6-Ag-imm and PCL-1.0-Ag-imm showed a much higher bactericidal activity than the films derivatized through the dip-coating method and the control. Among the two compositions obtained through the immobilization method, PCL-0.6-Ag-imm showed ~70 % bacterial inhibition by 4 h, whereas ~95 % inhibition by PCL-1.0-Ag-imm at a lesser time of 3 h. By 4 h, 100 % microbial inhibition was observed with PCL-1.0-Ag-imm, thus proving to be the best composition among all tested in this study. The higher bactericidal efficacy of PCL-1.0-Ag-imm, as opposed to PCL-0.6-Ag-imm, may be attributed to the higher silver loading in the former composition. The bactericidal behavior of all the samples was analyzed after 24 h, which revealed no relapse of any bacterial growth.

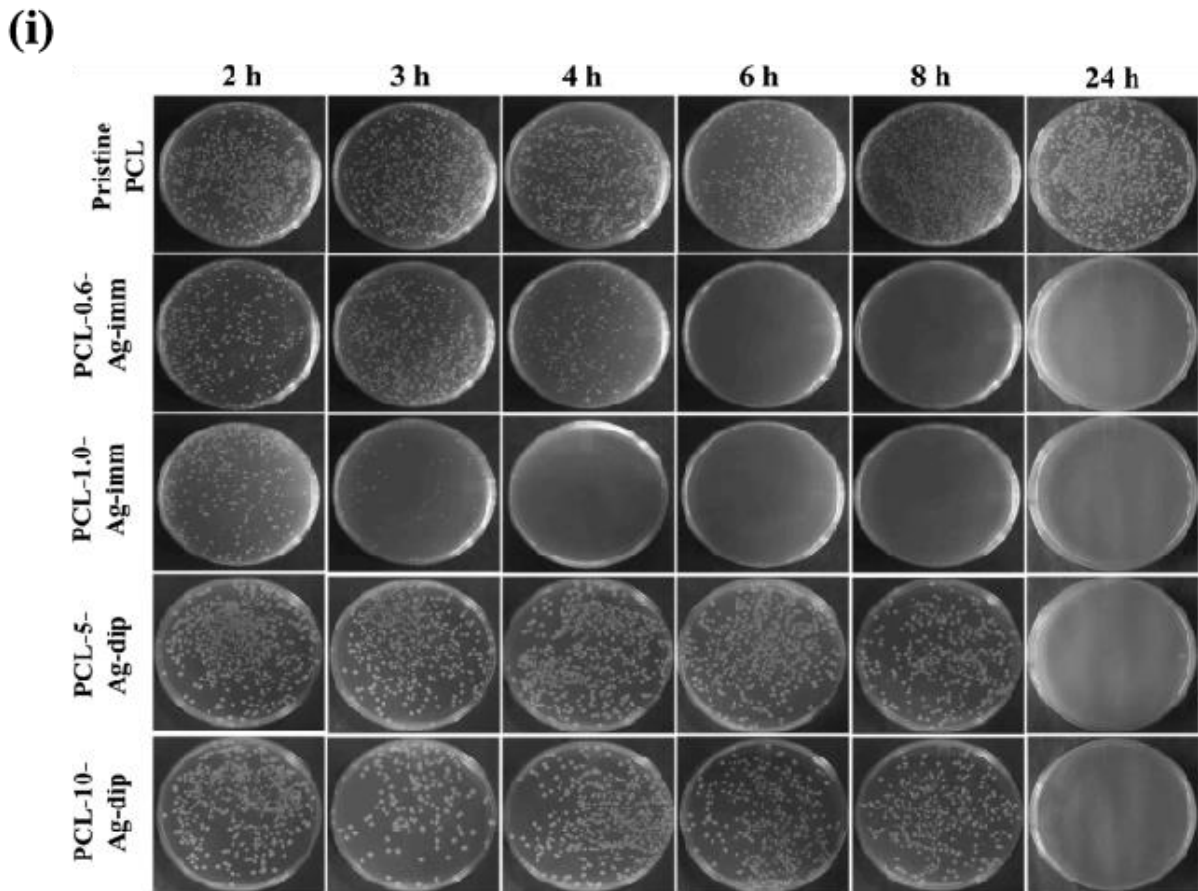


Figure. 2.8 (i). Antimicrobial studies with pristine and silver-derivatized PCL films against *E. coli* for different incubation periods.

(ii)

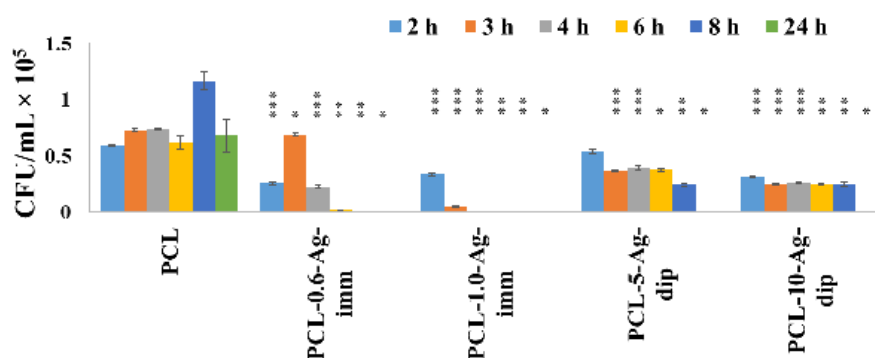


Figure 2.8 (ii) Bacterial cell viability derived from the colony count data of antimicrobial study using the pristine and silver-derivatized PCL films. The experiments were performed in triplicates, whose statistical significance was calculated using the student's t-test and represented in asterisks: * ($P < 0.05$) for border line significance, ** ($P < 0.01$), *** ($P < 0.001$) for high level significance.

The sample PCL-1.0-Ag-imm was analyzed for its surface morphology using FE-SEM and silver content through XPS after 24 h incubation in the bacterial culture **Figure 2.9 (i and ii)**. The results revealed that the 24 h incubation in the bacterial culture did not alter the morphology and silver content significantly. These results revealed the long-lasting bactericidal activity of the PCL films immobilized with the lipase capped Ag NPs, which is a preferred attribute for several biomedical applications.

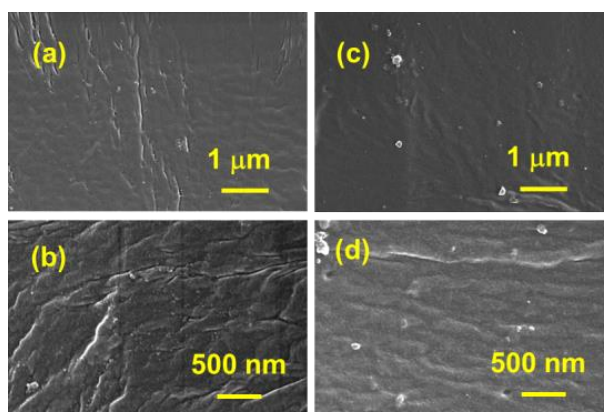


Figure 2.9 (i). FE-SEM images of (a, b) PCL-0.6-Ag-imm, and (c, d) PCL-1.0-Ag-imm after 24 h incubation in the bacterial culture.

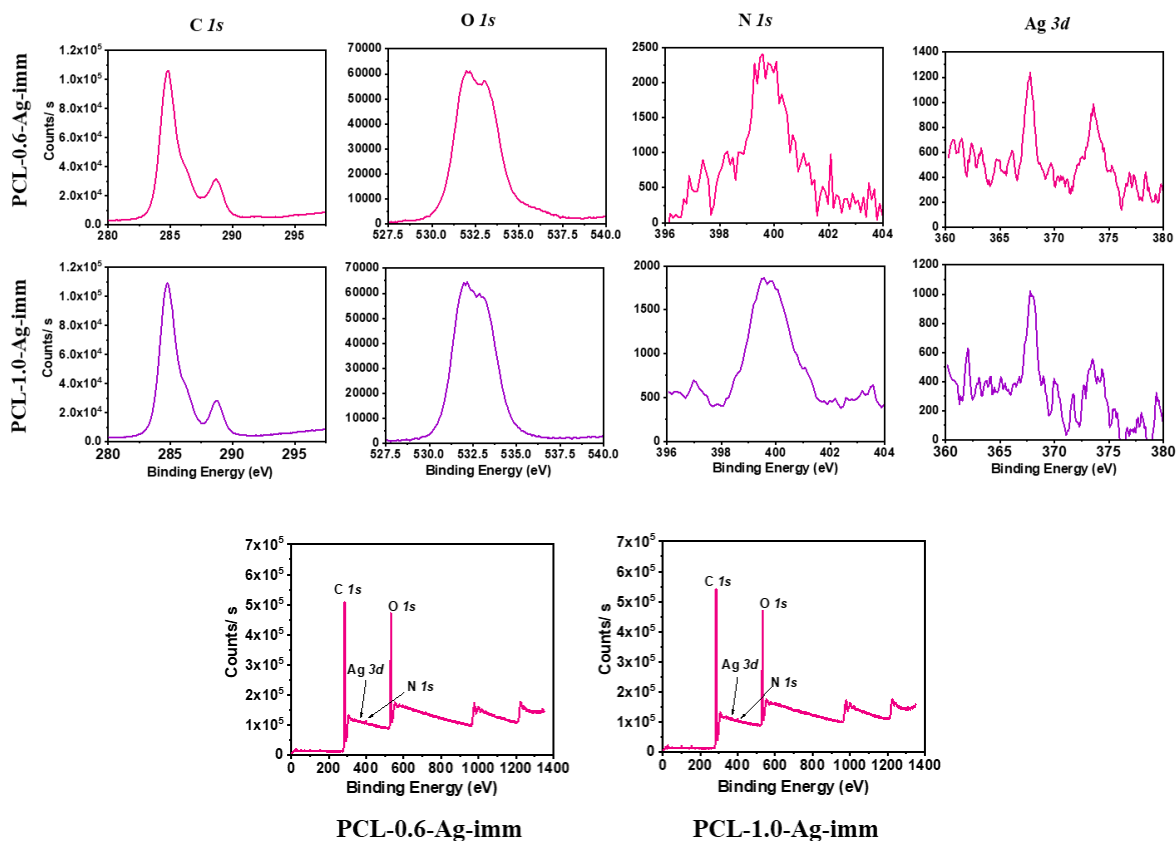


Figure 2.9 (ii). Top and middle rows: XPS narrow scan spectra of PCL-0.6-Ag-imm, and PCL-1.0-Ag-imm samples after 24 h incubation in the bacterial culture. The corresponding survey scan spectra are presented in the bottom most row.

2.3.4 In vitro cytotoxicity

The cell viability test was performed to evaluate the biocompatibility of the PCL films derivatized with silver. The viability of mouse fibroblasts cells seeded over the PCL films taken in the tissue culture plates was observed after 24 h and the results are shown in **Figure 2.10**. It was found that Ag NPs-immobilized PCL films showed ~98 % cell viability when compared to the pristine PCL film. On the other hand, the silver derivatized PCL films prepared through the dip-coating method exhibited ~73–75 % of cell viability against the control PCL film. The precise reason for this decrease in the cell viability in these samples is unclear at the moment. However, the overall antimicrobial and cytotoxicity studies revealed that the Ag NPs-immobilized PCL films have a high potential for *in vitro* as well as *in vivo* applications.

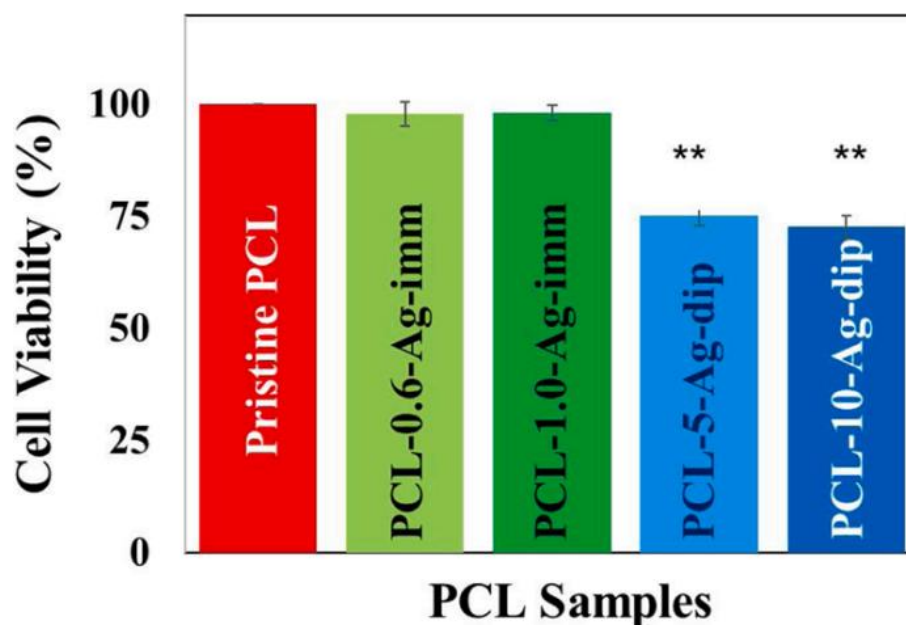


Figure 2.10 Cell viability study over mouse fibroblast cells (SNL 76/7) using the pristine and silver-derivatized PCL films used in this study.

2.4 Conclusions

The current study primarily employed a probiotically derived lipase from *Lactobacillus amylovorus* to derivatize PCL film surface with silver. Two facile surface derivatization approaches, such as lipase-capped Ag NPs' immobilization over EDC/NHS-activated PCL films and dip-coating over lipase immobilized PCL films, were carried out to explore their antimicrobial performance. The surface derivatization was chemically probed using XPS and morphologically probed using FE-SEM. The antimicrobial studies revealed that the PCL films immobilized with the probiotically derived lipase-capped Ag NPs exhibited remarkable bactericidal efficacy as opposed to the samples obtained through the dip-coating method. The cytotoxicity studies using mouse fibroblast SNL 76/7 cells revealed the high cell compatibility of PCL films immobilized with the lipase-capped Ag NPs. The results showed that the PCL films derivatized with biogenically synthesized Ag NPs could potentially serve as infection-free implantable materials.

Chapter 3

Influence of citrate buffer and flash heating in enhancing the sensitivity of ratiometric geno-sensing of Hepatitis C virus using plasmonic gold nanoparticles

3.1 Introduction

Owing to the innate plasmonic and electronic properties, gold nanoparticles (Au NPs) gained significant attention in several biological applications [105]–[111]. In the context of bio sensing, the pioneering work by Mirkin *et. al.*, on ligating the thiol-tagged DNA to Au NPs triggered numerous opportunities. Ever since, the Au NPs turned out to be revolutionary in most of the techniques such as colorimetric, surface-enhanced Raman scattering, electrochemical, spectrophotometric and piezoelectric [112]–[121]. In majority of these techniques, the efficient hybridization between the thiol-tagged probe and target DNA is crucial. Also, quantitative binding of the thiol-tagged probe over Au NPs is another important factor for higher efficacy of the sensing assay [122]–[125].

The citrate-capped Au NPs typically possess a zeta potential in the range of -30 ± 10 mV, signifying the negatively charged surface nature [126]. DNAs also possess similar charge on their backbone due to the negatively charged phosphate moieties [127]. Thus, when the thiol-tagged DNAs were attempted to conjugate with the surface of citrate-capped Au NPs, due to the charge-charge repulsion, the efficacy of the binding was found to be poor [128], [129].

To overcome this, salt-aging technique was developed, in which the externally added electrolyte such as NaCl minimizes the charge-charge repulsion between the citrate units as well as with the phosphate moieties of the incoming DNAs and thereby creating adequate void space for the thiolated DNA to approach the surface of Au NPs [35], [36]. However, the salt-aging process requires 24–48 h for efficient conjugation [122]. This has been overcome by strategies like tuning the pH of the Au NPs using citrate buffers, instant dehydration in butanol (INDEBT), etc. [37], [38]. Such strategies have been found to yield rapid and quantitative thiol conjugation over the Au NPs. Among these, the method that utilizes citrate buffer is highly attractive due to its simplicity and efficiency. It is generally believed that such conjugation

conditions are required when more amount of DNA has to be conjugated over the Au NPs and therefore the previous studies focused with high DNA to Au NPs ratio (typically >20). However, the necessity of citrate buffer for the cases with low DNA to Au NPs ratio has so far not been explored.

Successful hybridization between the probe and target DNA is also critical in bio sensing. The degree of hybridization therefore is an important criterion to realize this. There is a vast diversity in the literature with respect to the DNA hybridization conditions. Many reports employ 37 °C as the hybridization temperature, while adapting the duration as 1–4 h [38], [130]–[133]. On the other hand, in an attempt to realize the hybridization at a shorter time, slightly higher temperatures in the range of 55 to 65 °C are used, while the time was decreased to 20 min [134]–[136]. Few literature reports adopt a short-duration of flash heating at 95 °C, followed by hybridization at normal temperatures [137], [138]. Thus, there exists a significant diversity in terms of the hybridization conditions.

On a different note, 185 million population is globally affected by the Hepatitis C virus (HCV), which is a blood-borne pathogen. It is known that the serological diagnosis responds typically 4 to 6 weeks post-infection due to the time required for the production of adequate amount of the antibodies. Contrarily, the molecular diagnostics is preferred, as it is highly sensitive and early stage detection in 1 to 2 weeks post-infection is possible [135]. Since there is no licensed vaccine available till date, though efforts are undertaken by the researchers [139], the timely detection and diagnosis is imperative, since the undetected and untreated conditions could lead to hepatocellular carcinoma [140]. Therefore, in this current study, we utilized an antisense oligonucleotide (ASO) derived from the core region (conserved region) of the HCV genome and subjected it to Au NPs based sensing against the viral target using optimal hybridization and citrate-mediated conjugation conditions.

3.2 Methodology

3.2.1 Materials and Characterization

Trisodium citrate and $\text{HAuCl}_4 \cdot 3\text{H}_2\text{O}$ were procured from Sigma Aldrich, and used as received. The target (5'-CGGATTCGCCGACCTCATGGGGTACATCCCGCTCGTCGGC-3'), ASO (5'-SH-AAAAAAAAAAGCCGACGAGCGGGATGTACCCCATGAGGTCGGCGAATCCG-3'), and control (5'-TTACCGATAATCCTCCGGGGCATAACGAATGCTTATAGGA-3') oligos were purchased from Eurofins Pvt. Ltd. For reducing the disulfide bond of thiol-modified probe, 100 mM DTT (in 100 mM sodium phosphate buffer, pH 8.3–8.5) was added at 1:5 ratio and incubated at room temperature for 1 h. Phosphate buffer saline (PBS, 1X) was prepared using 37 mM NaCl, 2.7 mM KCl, 10 mM Na_2HPO_4 and 1.8 mM KH_2PO_4 . The citrate buffer was prepared by dissolving 25.08 mg of trisodium citrate in 1 mL of water (100 mM) and the final pH was adjusted to 3.0 using dilute HCl. Spectramax[®] iD3 was employed to follow the UV–visible spectral changes of the Au NPs based geno-sensing assay. The particle size analysis was performed using the Malvern Zeta sizer instrument.

3.2.2 Au NPs-based genosensing

The well-known Turkevich method was employed to synthesize the citrate-stabilized Au NPs [141]. The synthesized Au NPs exhibited a strong plasmonic peak at 520 nm with an average hydrodynamic diameter of ~20 nm. In the case of DNA sensing, the hybridization mixture comprising of 2.5 μL of the ASO and 2.5 μL of target/control in 2.5 μL of the 1X PBS buffer was taken in a PCR tube. Two conditions were employed for hybridization inside a Thermal Cycler: In one case, the hybridization was carried out at 65 °C for 20 min without any flash heating and in the remaining cases a flash heating for a short duration at a designated higher temperature (75 °C for 30 s, 85 °C for 30 s and 95 °C for 30 s / 60 s / 120 s) prior to

hybridization at 65 °C for 20 min. To the hybridized mixture, about 50 μL of Au NPs was added and the resultant solution was subjected to stability analysis by adding 1.75 μL and 2.5 μL of 5 M NaCl solution such that the final NaCl concentration was 145 mM and 340 mM, respectively. The same procedure has also been performed with the addition of 0.75 μL of citrate buffer along with the hybridization buffer to ascertain the effect of DNA conjugation over Au NPs. After salt addition, the absorbance of the plasmonic peak at 520 nm and the ratiometric values of absorbance at 700 nm to 520 nm ($A_{700}/520$) were followed. The strategy employed in the current study is depicted in the **Figure 3.1** below.

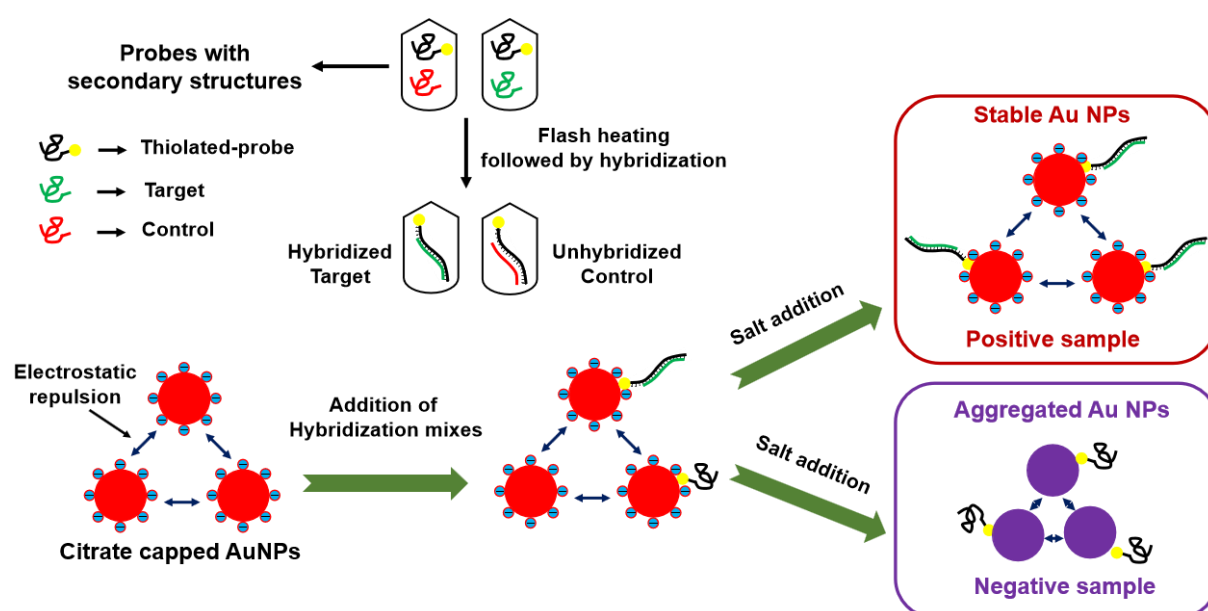


Figure 3.1 Diagrammatic representation on the mechanism of the sensing strategy employed in this study.

3.3 Results and discussion

Initially, a polyacrylamide gel electrophoresis (PAGE) experiment was carried out using a 20 wt% gel solution to assess the effect of different temperature conditions on the hybridization efficacy between the ASO and target DNA. **Figure 3.2 (a)** shows the gel image obtained with 3 μ M concentration of ASO and target/control DNAs subjected to different hybridization conditions. Two bands corresponding to ASO and control were clearly seen in the case of control experiments that confirmed no hybridization took place between the probe and control. On the other hand, a bright thick single band in the case of target subjected to different conditions revealed efficient hybridization between the ASO and target DNA. Further quantification of the bands corresponding to the hybridized DNA using ImageJ software (Version 1.8.0_172) revealed a 7.5% higher hybridization efficacy with the sample subjected to a flash heating of 95 °C for 120 s, as opposed to the sample that was not subjected to any flash heating **Figure 3.2 (b)**. These results prompted us to probe further the effect of hybridization conditions in the Au NPs based DNA sensing. For this, we chose three conditions such as no flash heating, and 30 s and 120 s flash heating at 95 °C. While one set of samples were subjected to Au NPs based sensing assay to ascertain only the effect of flash heating conditions, another set of samples were subjected to the sensing assay with the addition of citrate buffer in the hybridized mixture as it has been proven to yield rapid and quantitative thiol-conjugation over Au NPs in minutes [37].

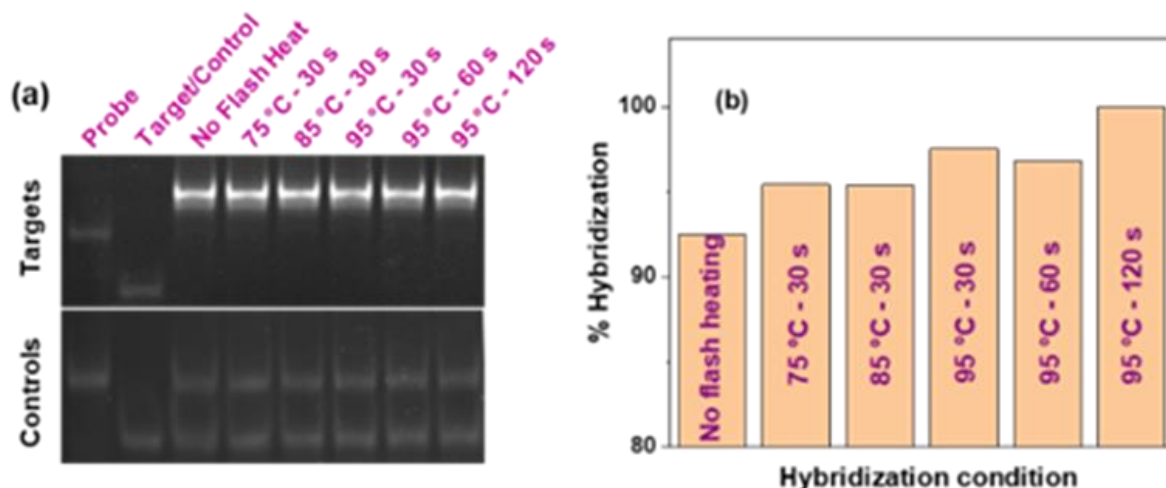


Figure 3.2 (a) Polyacrylamide gel electrophoresis of the probe, target and control DNA subjected to different hybridization conditions and (b) the corresponding percentage hybridization quantification using ImageJ software.

The mechanism of the Au NPs mediated sensing assay is based on the following factors. It is known that the stability of the Au NPs is imparted due to the electrostatic repulsion between the negatively charged citrate moieties on the surface. The citrate-stabilized Au NPs synthesized through the Turkevich method exhibit a plasmonic peak at 520 nm and a relatively low absorbance at wavelengths greater than 650 nm in the UV–visible spectroscopy. Upon salt addition, due to the masking of electrostatic repulsion between the citrate moieties by the excess of sodium ions, the Au NPs tend to aggregate. The aggregated colloidal Au NPs are known to compromise their plasmonic absorbance and exhibit higher light scattering at longer wavelengths. It is known that the negatively charged DNA enhances the charge density (zeta potential) of the Au NPs upon binding to them. Such an enhancement in the charge density shall enhance the stability of the nanoparticles against the salt-induced aggregation of the Au NPs. Thus, the Au NPs effectively hybridized with the target DNA sequence shall possess higher stability in comparison to the negative/control sample, and thereby retain the red color arising from the SPR.

In the case of DNA sensing, two different initial concentrations of the ASO, such as 1.5 and 3 μM were hybridized with equimolar concentration of the target/ control. Also, two different conditions were employed for the thiol conjugation over the Au NPs before the salting-out process: (i) without the addition of citrate buffer and (ii) with the addition of 0.75 μL of citrate buffer. The UV–visible spectral results obtained from the DNA sensing studies are presented in **Figure 3.3**.

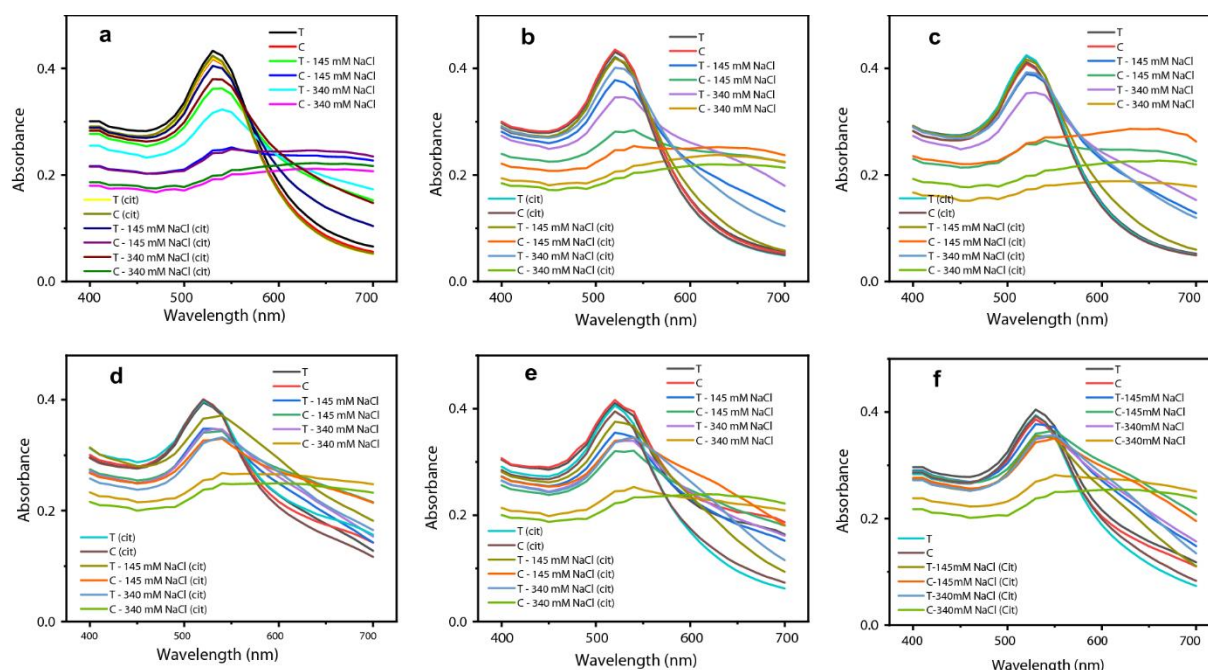


Figure 3.3 The UV-visible spectra of the Au NPs added to the oligonucleotides subjected to different hybridization conditions in terms of flash heating: (a, d) no flash heating, (b, e) 95 °C for 30 s, and (c, f) 95 °C for 120 s. The top and bottom row experiments were performed with 1.5 and 3.0 μM concentrations of the oligonucleotides, respectively. The respective symbols T and C represent target and control, while the experiments performed with the addition of citrate buffer were coded with (cit). The final concentrations of the NaCl were also mentioned alongside the sample code

The absorbance of Au NPs at 520 nm as well as the ratiometric value of 700 nm/520 nm (A_{700}/A_{520}) have been chosen to follow the effect of hybridization conditions on DNA sensing and the absorbance values before and after salting are summarized in **Table 3.1**. It can be seen from **Figure 3.3** that the Au NPs added with target/control exhibit a high absorbance value at 520 nm (> 0.4) and a low A_{700}/A_{520} ratiometric value of < 0.4 . After salt addition, the

absorbance of the positive samples (containing target) at 520 nm gradually decreased with the addition of NaCl solution, while the A700/520 ratiometric value gradually increased. In the case of positive samples, the cut-of values of the absorbance at 520 nm and A700/520 were found to be > 0.26 and < 0.5 , respectively, which indicate the stable nature of the Au NPs. Among the different hybridization conditions employed, the target-ASO hybrids subjected to flash heating were found to have a slightly higher absorbance value at 520 nm than the no flash heating sample, though the difference was less (**Table 3.1**).

Absorbance	Hybridization conditions	T	C	T	C	T	C	T	C	T	C	T	C	
		145 mM	145 mM	340 mM	340 mM	cit	cit	145 mM	145 mM	340 mM	340 mM	cit	cit	
A ₅₂₀	1.5 μM Probe													
	No flash heating	0.43	0.42	0.36	0.25	0.32	0.19	0.42	0.42	0.40	0.24	0.38	0.20	
	95 °C – 30 s	0.43	0.44	0.38	0.28	0.35	0.21	0.42	0.42	0.42	0.25	0.40	0.19	
	95 °C – 120 s	0.42	0.41	0.39	0.26	0.35	0.17	0.43	0.41	0.42	0.26	0.39	0.20	
	3.0 μM Probe													
	No flash heating	0.40	0.40	0.35	0.34	0.34	0.25	0.40	0.40	0.37	0.33	0.32	0.24	
	95 °C – 30 s	0.41	0.42	0.35	0.32	0.34	0.24	0.41	0.39	0.38	0.34	0.34	0.22	
	95 °C – 120 s	0.40	0.39	0.38	0.36	0.35	0.27	0.39	0.39	0.36	0.34	0.35	0.24	
	A _{700/520}	1.5 μM Probe												
No flash heating		0.14	0.13	0.41	0.91	0.53	1.07	0.12	0.12	0.24	0.96	0.37	1.08	
95 °C – 30 s		0.13	0.12	0.35	0.79	0.52	1.09	0.12	0.12	0.14	0.96	0.26	1.10	
95 °C – 120 s		0.12	0.12	0.33	0.87	0.43	1.03	0.12	0.12	0.14	1.01	0.30	1.11	
3.0 μM Probe														
No flash heating		0.32	0.36	0.41	0.63	0.45	0.97	0.39	0.29	0.50	0.66	0.51	0.98	
95 °C – 30 s		0.40	0.45	0.43	0.56	0.48	0.85	0.15	0.19	0.25	0.53	0.34	1.00	
95 °C – 120 s		0.27	0.26	0.36	0.55	0.42	0.91	0.17	0.19	0.28	0.53	0.35	0.98	

Table 3.1 UV-visible absorbance data (at 520 nm and the ratiometric at 700 nm/520 nm) of Au NPs added to the oligonucleotides hybridized under different conditions before and after salting with two different final concentrations of NaCl. The data obtained are at 95% confidence level.

On the other hand, a substantial difference was noticed in the ratiometric values of the hybrids subjected to different hybridization conditions. The ratiometric values corresponding to different hybridization conditions have been plotted in **Figure 3.4**.

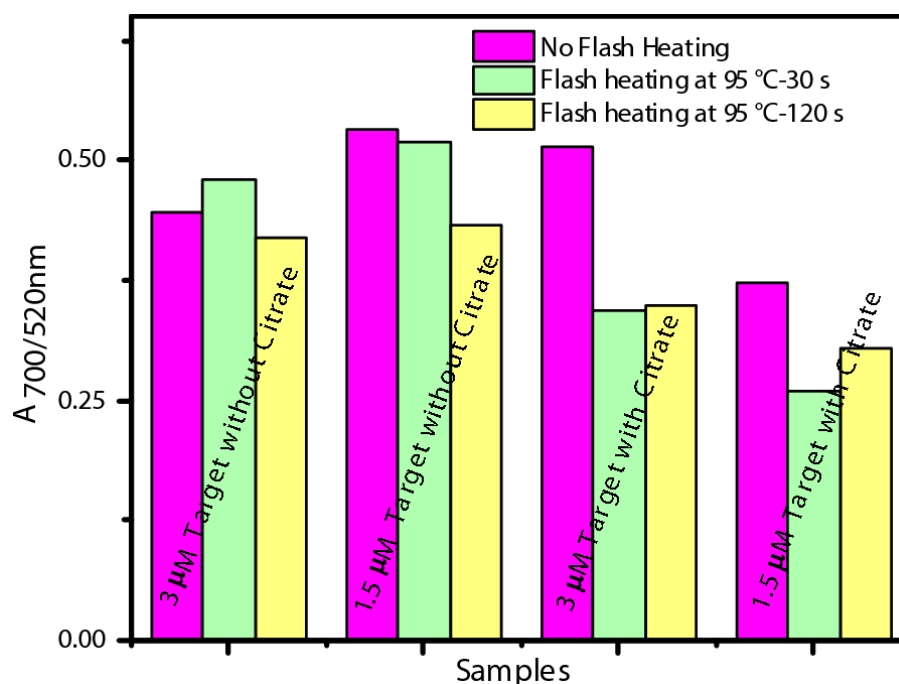


Figure 3.4 Plot depicting the $A_{700/520}$ ratiometric values of selected samples as a function of different hybridization conditions.

In general, before the salting process, the absorbance of Au NPs at 520 nm was found to be in the range of 0.40 to 0.43, while the $A_{700/520}$ ratiometric values were found to be in the range of 0.15 to 0.4 for all the samples. When 1.75 and 2.5 μ L of NaCl was added sequentially (total amount of NaCl added was 4.25 μ L) such that the final salt concentration was 145 and 340 mM, the target and control were properly discriminated, as evidenced by the high absorbance value at 520 nm and low $A_{700/520}$ ratiometric value for the target. It can be seen from **Table 3.1** that the target samples subjected to flash heating exhibited lesser ratiometric values than the ones not subjected to flash heating (highlighted in bold). These results indicate that flash heating does play a positive role in enhancing the hybridization efficacy, which results in better discrimination at the ratiometric values that are often considered to be useful in improving the

sensitivity of the assay. The experiments were then performed with the addition of citrate buffer to ascertain the effect of DNA conjugation over Au NPs and its subsequent effect on the sensitivity of the assay. It was found that the discrimination between the target and control at the ratiometric values was more pronounced when citrate buffer was used. This reveals that the use of citrate buffer is useful in enhancing the conjugation efficiency even when the DNA to Au NPs ratio is as low as 3.5:1, while the available literature reports used a ratio of 20:1 and higher [37]. Since the citrate buffer showed additional benefit in ratiometrically discriminating the samples subjected to flash heating from no-flash heating, their corresponding digital photograph, and dynamic light scattering (DLS) results are presented in **Figure 3.5 and 3.6**. Although the digital photograph shows the color of the Au NPs used in different assay conditions is indistinguishable to human eyes, the DLS measurements of samples subjected to flash heating revealed a decrease in the particle size after subjecting to the salting-out process, which rationalizes their lower ratiometric values. The study has revealed the beneficial role of employing a combination of flash heating for efficient hybridization and citrate buffer for rapid tagging of the thiolated DNA over the surface of Au NPs. Such a combination has been found to enhance the sensitivity of the ratiometric absorbance values in the Au NPs based gene sensing. It can be noted that the ratiometric values are highly decisive in discriminating the single nucleotide polymorphism, as described by Sanromán-Iglesias et al. using gold nanoparticles of sizes 13, 46, and 63 nm [142]. Our study reveals that employing appropriate hybridization conditions can further improve the ratiometric sensitivity of such Au NPs based assays.

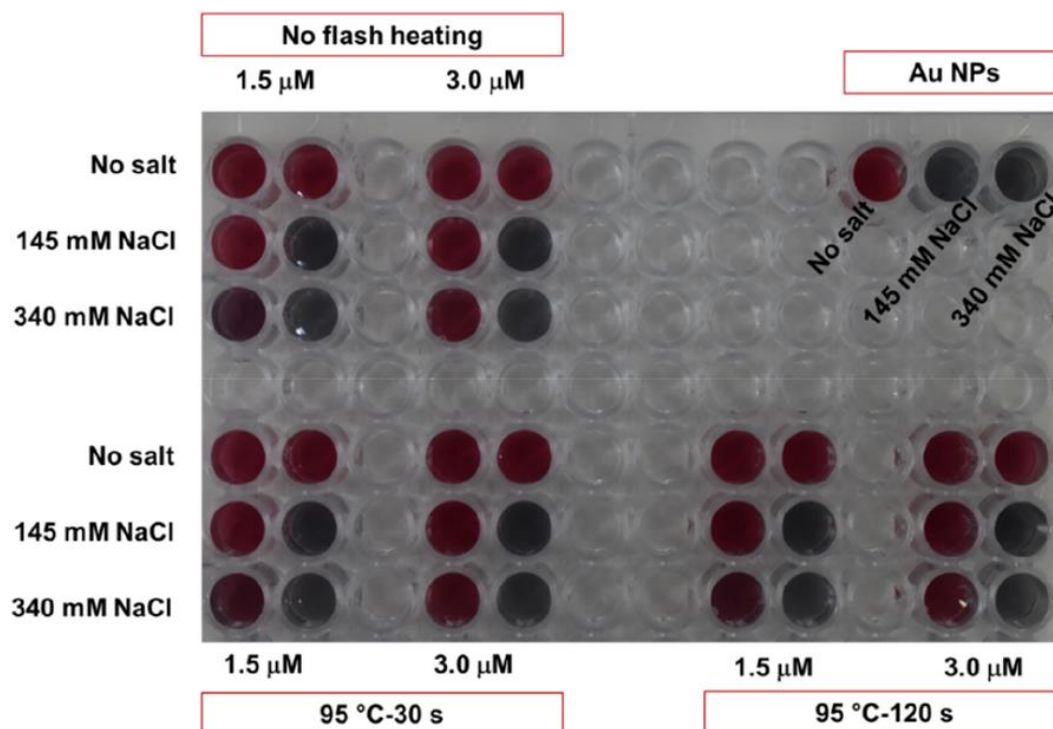


Figure 3.5 Digital photograph showing the color of the Au NPs in citrate buffer—added with the target samples subjected to different hybridization conditions before and after salting-out process.

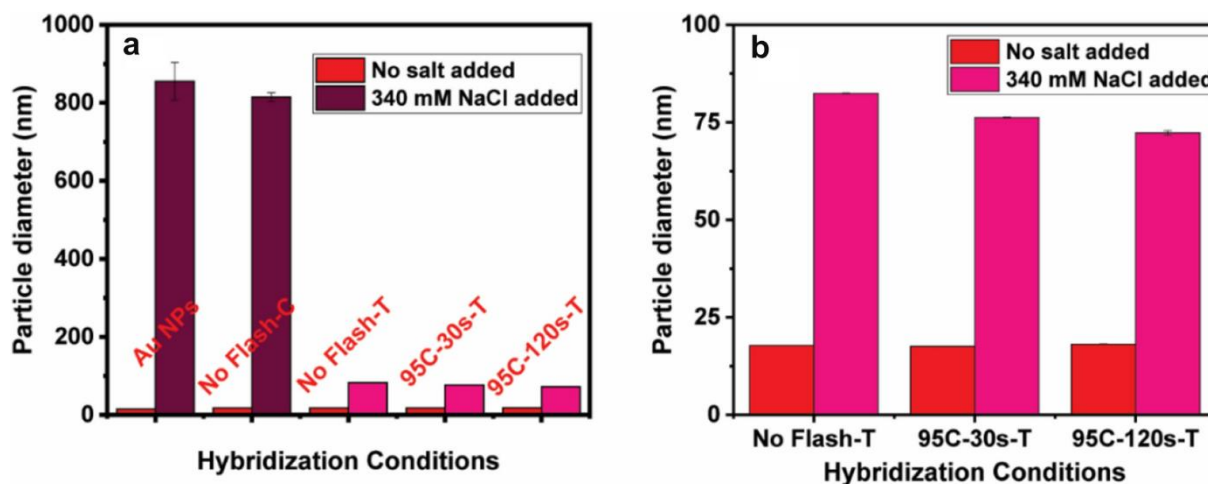


Figure 3.6 Effect of particle aggregation measured through the dynamic light scattering analyses over Au NPs in citrate buffer before and after addition of 340 mM NaCl: (a) panel showing the effect of salt-induced aggregation over citrate-capped Au NPs, control sample without any flash heating, and target subjected to three different hybridization conditions. The concentration of probe, target (T), and control (C) were fixed as 3 μ M. (b) Zoomed in data of the target samples subjected to different hybridization conditions shown in (a).

3.4 Conclusions

In summary, the effect of hybridization between an ASO and target DNA was ascertained using PAGE experiment, which revealed that the hybridization involving a flash heating of 95 °C for 120 s, prior to the incubation at 65 °C for 20 min, resulted in an enhancement in the efficacy to the tune of 7.5% as opposed to the hybridization condition without the flash heating. The effect was further analyzed in the Au NPs based DNA sensing to ascertain the usefulness of the flash heating in practical applications. The DNA sensing studies using thiol-tagged synthetic oligonucleotide derived from the core region of the HCV viral genome revealed that the ASO-target DNA hybrid subjected to the flash heating stabilized the Au NPs more than the case without flash heating, as evidenced by the lesser ratiometric absorbance values for the former. Furthermore, the use of citrate buffer has shown to be beneficial in the efficient conjugation between the thiolated probe and the Au NPs, even when the DNA to Au NPs ratio is as low as 3.5:1 and 7:1. These results may find potential in employing the appropriate hybridization conditions in the DNA bio-sensing studies.

Chapter 4

Fluorescence-based simultaneous dual oligo-sensing of HCV genotypes 1 and 3 using magnetite nanoparticles

4.1 Introduction

Nucleic acid tests (NATs) are considered the gold standard in detecting various disease-causing pathogens [143], [144]. Due to this reason, there is increasing attention to developing efficient strategies that address the challenges associated with efficacy, simplicity, and cost [134], [145], [146]. Unlike antibody-antigen interactions, the NAT-based techniques are more sophisticated and costlier [147]. However, such techniques are essential to derive high sensitivity and selectivity, thus enabling one to detect precious analytes in ultralow concentrations while substantially minimizing the false-positive and false-negative results [148]–[150]. Moreover, NAT is the preferred method to detect the distinct variations in the microbial genes leading to different variants or genotypes [151]–[153]. Several NAT-based strategies such as reverse transcription-polymerase chain reaction (RT-PCR), hybridization chain reaction (HCR), loop-mediated isothermal amplification (LAMP), and rolling circle amplification (RCA), etc., have been extensively studied [154]–[158]. In this context, there has been a surge in developing hybrid strategies that couple the conventional NAT-based techniques with nanotechnology borne approaches like optical, magnetic and electrochemical to harness the benefits of enhanced sensitivity, quantification, cost effectiveness, and potentially towards multiplex detection [159]–[162].

Recently, multiplex detection of biomolecules is gaining impetus, as this would allow simultaneous screening of multiple analytes and thereby substantially save cost [163]–[167] and time. For instance, Wang et al., developed a surface-enhanced Raman scattering-based lateral flow assay biosensor, which was shown for its dual nucleic acid detection capability, as demonstrated with the target DNAs associated with Kaposi's sarcoma-associated herpesvirus and bacillary angiomatosis [168]. In a similar line, Zheng et al., reported a fluorescence quenching-based strategy, wherein fluorescently-labeled dual probes were used for the simultaneous detection of microRNAs, miRNA-21, and miRNA-155, that could indicate the drug resistance in lung cancer [169]. Li et al., developed a paper-based chip to simultaneously detect three antibiotic resistant genes. This assay was based on the coupling of loop-mediated isothermal amplification with a turn-on fluorescent molecule, $[\text{Ru}(\text{phen})_2\text{dppz}]^{2+}$ [170]. Han

et al., 2019 reported a three-helix molecular beacon design, which was demonstrated for simultaneous fluorescence detection of two HIV DNA probes in a sensitive manner [171]. Xiang et al., 2019 developed a new approach for detecting multiple oligos like microRNA and DNA, wherein the formation of an active DNAzyme in the presence of the target sequence triggered the release of the G-quadruplex, which then combined with thioflavin T to cause enhanced fluorescence [172]. Zou et al., 2019 presented an efficient method based on DNA-stabilized fluorescent silver nanoclusters to simultaneously detect two HIV DNAs [173]. These representative literatures indicate the necessity of advanced diagnostic strategies for multiplex sensing of biomolecules.

On a different note, magnetite nanoparticles (NPs), owing to their magnetic responsiveness in nature have garnered an indispensable position in the field of nanotechnology [174]–[177]. Recent work by Patra et al., 2019 has shown that magnetic NPs can be used to pre-concentrate a dye 100 times by a simple adsorption-desorption process [178]. Another article by Goon et al., 2010 reported gold-coated magnetite NPs as dispersible electrodes for selective capturing of the analyte in a dilute solution, followed by rapid electroanalytical quantification [179]. On a different note, hepatitis C virus (HCV) is a blood-borne and contagious pathogen whose discovery was awarded the Nobel prize in the year 2020 [135]. The virus is known to have 8 genotypes, which are classified into 105 subtypes, among which genotypes 1 and 3 globally account for ~ 46.2% and ~ 30.1% of the cases, respectively [136]. In this current work, we aim to develop a simultaneous dual-probe sensing of HCV genotypes 1 and 3 by combining magnetite NPs with a fluorescence-based detection assay. The surface derivatization of magnetite NPs with the probe DNAs, complementary to the HCV genotypes 1 and 3, subsequent steps of dual-probe sensing are presented.

4.2 Methodology

4.2.1 Materials

The reagents iron (II,III) oxide (magnetite) NPs, ethylenediaminetetraacetic acid (EDTA), and the linker glutaraldehyde were procured from Sigma Aldrich, India, while (3-aminopropyl)triethoxysilane (APTES) was procured from Thermo Fisher Scientific, India. All

the oligonucleotides were procured from Eurofins India, Pvt. Ltd. A total of nine oligonucleotides including three control sequences along with two amine-modified probes (G1 probe-1 and G3 probe-1), two fluorescently labeled probes (G1 probe-2 and G3 probe-2), and two target oligos (G1 target and G3 target) corresponding to the HCV genotypes 1 and 3, respectively, were employed in the study.

4.2.2 Design of the Oligonucleotides

The NS4B and NS5A regions corresponding to HCV genotypes 1 and 3 were subjected to multiple sequence alignment using ClustalW to design the target oligonucleotides (36-mer each). These sequences were found to be highly specific to the respective genotypes. The designed sequences were identified by implying the conditions like minimal self-complementarity with a cut-off of 4, no hairpin loop formation above a cut-off of 3, and a GC content of < 60% to have the melting temperature (T_m) close to 65 °C. The complementary probes (18-mer each) for each genotype-specific target were designed, which were also found to obey the above criteria. The designed target, probe, and control sequences pertaining to the study are tabulated below.

Table 4.1: Complementary probes for each genotype 1 and 3, target and control probes.

Oligo	Sequence (5'- 3')
G1 probe-1	NH ₂ -AAAAAAAAAAGAAGACTAGCACACGGGGC
G1 probe-2	GATGCAATTCGAGCTTAT-Rhodamine red (RR)
G1 target	ATAAGCTCGAATTGCATCGCCCCGTGTGCTAGTTCT
G3 probe-1	NH ₂ -AAAAAAAAA ACTGTGTATCGACCCCTG
G3 probe-2	AAGATGAGCTACTCTCCT-Cyanine 3 (Cy3)
G3 target	AGGAGAGTAGCTCATCTTCAGGGTTCGATACACAGT
Control 1	AAAAAAAAAGGGGGGGGGGGGGGGGGGAAAAAAAA
Control 2	CCCCCCCCAAAAAAAAACCCCCCCCCAAAAAAAAAAAA
Control 3	TTACCGATAATCCTCCGGGCATAACGAATGCTTATAGGA

4.2.3 Surface Derivatization of Magnetite NPs

The commercial magnetite NPs were initially functionalized with amine groups using APTES by following the standard protocol reported in the literature [180]. Briefly, a round bottom flask containing 50 mg of magnetite NPs dispersed in 2.5 mL of absolute ethanol was added with 0.5 mL of APTES and incubated under shaking conditions for 24 h at 30 °C. After this, the NPs were magnetically separated from the solution, washed thrice with ethanol, and dried in a vacuum oven. The amine-functionalized magnetite NPs were then treated with a linker,

glutaraldehyde. This was performed by treating the above-obtained magnetite NPs with 2 mL of phosphate saline buffer solution (0.1 M, pH 7.4), supplemented with 1 mL of 25% glutaraldehyde solution, for 2 h under shaking conditions. Following this, the magnetite NPs were washed thrice with milliQ water and then added to 50 μ L of sterile water, to which 50 μ L of 100 μ M amine-probe DNA was added, and the reaction mixture was kept under shaking for 2 h. The magnetite NPs were then recovered using a magnet, washed twice with milliQ water, and used for subsequent studies. To minimize the non-specific binding, the amine probe-immobilized magnetite NPs were treated for 4 h with a 1 mL aqueous solution of triethanolamine (10 mM) to block the unreacted sites, followed by washing and drying. The supernatant solution was analyzed for the quantity of unbound probe DNA through polyacrylamide gel electrophoresis (PAGE).

4.2.4 Dual Oligo Sensing

Two strategies have been employed to ascertain the efficacy of simultaneous dual oligonucleotide sensing: (i) a one-step method, where the amine-tagged probe-1 immobilized magnetite NPs were subjected to hybridization together with the fluorescently-labeled probe-2 and target/control; and (ii) a two-step method, where the fluorescently labeled probe-2 and target/control were separately allowed to hybridize in a first step, followed by hybridization with the amine-tagged probe-1 immobilized over the magnetite NPs in a subsequent step.

In a typical two-step hybridization method, 2 μ L of the fluorescently labeled probe-2 from a 100 μ M stock solution was added with 2 μ L of the target/control of varying concentrations and 6 μ L of sterile water to make the total volume as 10 μ L. The resulting mixture was gently vortexed and subjected to hybridization at 37 °C for 4 h. To the obtained solution, ~2.5 mg of probe-immobilized magnetite NPs was added, and the total volume of the solution was made up to 50 μ L. This mixture was also subjected to hybridization in the same manner as mentioned above. The obtained solution was finally diluted to 2 mL such that the concentration of the fluorescently-labeled probe-2 became 100 nM. The magnetite NPs were then removed from the solution, and the fluorescence intensity of probe-2 (unhybridized) in the supernatant solution was measured. The one-step hybridization method also was performed with an identical concentration of the probes, except that all the samples were taken and

hybridized together in a single step. The experiments were performed in triplicate and the average values are presented in the plots.

To explore the stability of the probe-immobilized magnetite NPs, the functionalized NPs were stored at 4 °C for 3 months, after which they were used for the sensing experiments at the two extreme concentrations. Further, to mimic the applicability of the assay in actual samples, we have performed the dual oligo sensing experiments with the optimized conditions, replacing sterile water with synthetic serum (6.8 g/L NaCl, 0.2 g/L CaCl₂, 0.4 g/L KCl, 0.1 g/L MgSO₄, 2.2 g/L NaHCO₃, 0.126 g/L Na₂HPO₄ and 0.026 g/L NaH₂PO₄ at pH: 7.4).

4.2.5 Characterization

The surface morphology and elemental mapping analyses of the magnetite NPs were performed using field-emission scanning electron microscopy (FE-SEM; Apreo S, FEI) instrument fitted with energy dispersive spectroscopy (EDS). After each derivatization step, the surface functionalization of magnetite NPs was ascertained through X-ray photoelectron spectroscopy (XPS; ThermoFisher, K-alpha), equipped with a monochromated Al K_α X-ray source. The steady-state fluorescence spectroscopic measurements of the solutions containing fluorescently labeled oligonucleotides were recorded using Fluorolog, Horiba Scientific instrument. All the fluorescence measurements were performed by keeping a constant slit width of 3 nm for both excitation and emission steps.

4.3 Results and Discussion

The schematic representation of the fluorescence-based dual oligo sensing using magnetite NPs is presented in Scheme 4, which depicts the following major steps: (i) APTES functionalization of magnetite NPs, (ii) anchoring of glutaraldehyde linker over the amine groups on the surface of magnetite NPs, (iii) immobilization of amine-tagged probe-1 over the magnetite NPs, and (iv) oligonucleotide sensing. Two target sequences (36-mers each) derived from HCV genotypes 1 and 3 were chosen for this proof-of-concept study. Against each target sequence, two probe sequences (probe-1 and probe-2) were designed in such a way that the 18-mer probe-1 was tagged with an amino group along with a 10-mer polyA linker at the 5' end, and the other 18-mer probe-2 was tagged with a fluorescent label at the 3' end. In the presence of the target,

probe- 1, probe-2, and the target shall be hybridized together, and therefore, the fluorescently-labeled probe-2 can be magnetically removed from the solution. The difference in the fluorescence intensity before and after magnetic removal of the NPs is used for the oligo sensing and quantitative analysis of the target sequence.

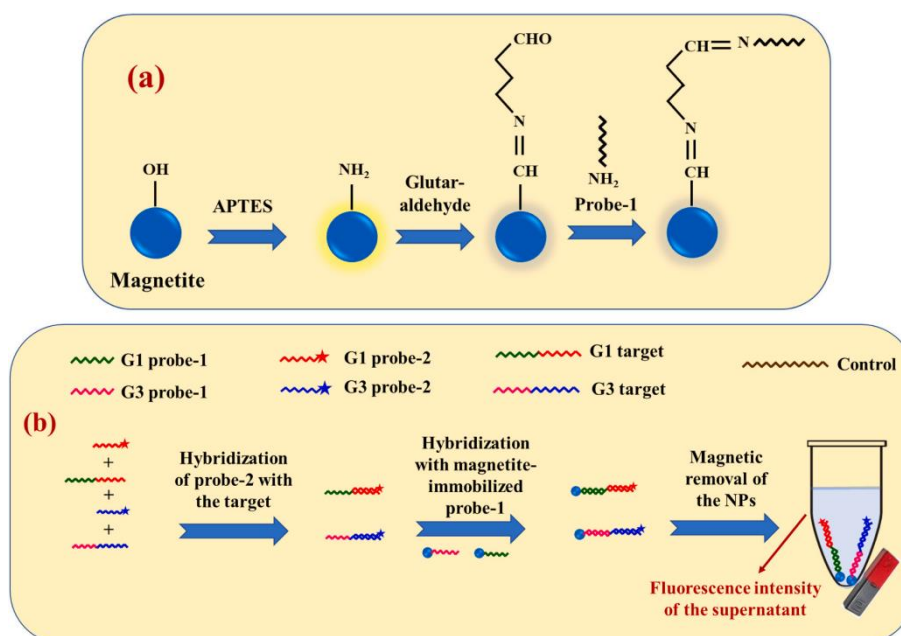


Figure 4.1 (a) Schematic representation of the surface-derivatization of magnetite NPs that comprise of APTES functionalization, glutaraldehyde anchoring, and amine-tagged probe-1 immobilization steps. (b) Pictorial representation of the two-step hybridization method of simultaneous dual oligo sensing, depicting the necessary steps such as hybridization of probe-2 with the target, followed by hybridization with the immobilized probe and finally magnetic removal of the hybrid.

XPS is a powerful surface-sensitive tool for elemental analysis. Therefore, the magnetite NPs were subjected to XPS measurements after each surface derivatization step. The XPS narrow scan spectra of Fe 2*p*, Si 2*p*, P 2*p*, and N 1*s* were recorded, and the results are presented in **Figure 4.2**. It can be seen from the figure that the pristine magnetite NPs exhibited the characteristic peaks of Fe, as evidenced by the respective 2*p*_{3/2} and 2*p*_{1/2} peaks at 710.3 and 724.2 eV arising from Fe³⁺, but no signals of other elements such as silicon, phosphorus, and nitrogen. After APTES functionalization, in addition to iron, the characteristic signals of Si 2*p* and N 1*s* were also observed at the binding energy values of 101.5 and 400.5 eV, respectively, which indicated the successful derivatization of amine groups. When glutaraldehyde was immobilized over these amine groups to make imine bonds, a slight shift in the N 1*s* signal

towards lower binding energy of 399.8 eV was observed, which clearly signified the conversion of amine to an imine [181]. With further immobilization of amine-tagged probes over the magnetite NPs, the intensity of the N $1s$ signal increased significantly, which could be attributed to the presence of nitrogen-rich nucleotides. Further, an intense signal arising from the P $2p$ level of phosphate moieties was observed that clearly proved the immobilization of the amine-tagged probe over the aldehyde derivatized surface.

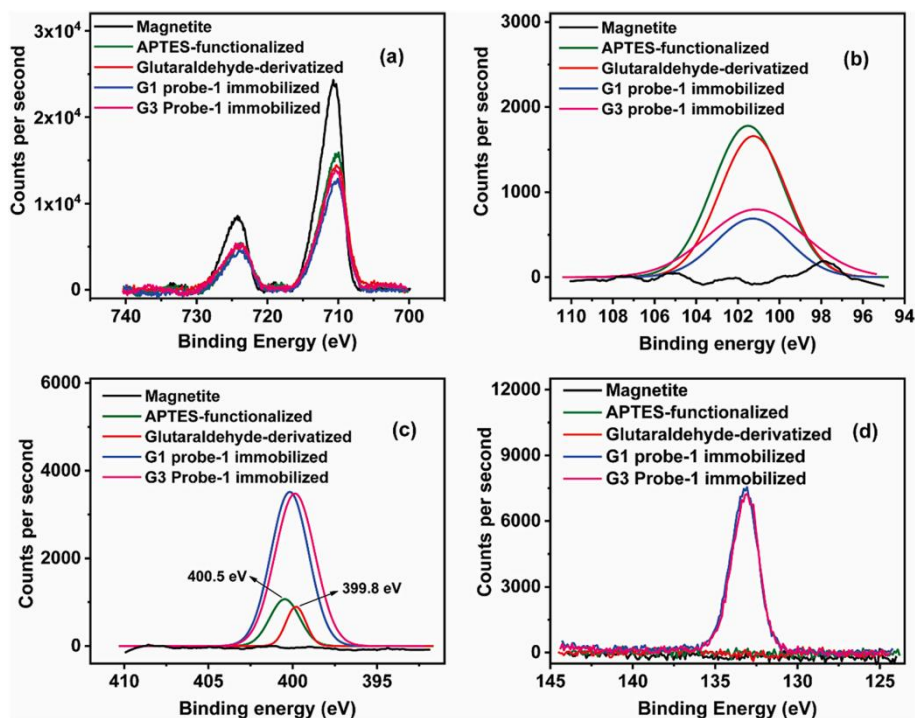


Figure 4.2 XPS narrow scan spectra of (a) Fe $2p$, (b) Si $2p$, (c) N $1s$, and (d) P $2p$ levels of magnetite NPs before and after each surface derivatization steps.

FE-SEM imaging and EDS mapping of the surface-derivatized samples were performed to ascertain the observations from the XPS analyses (**Figure 4.3**). The FE-SEM images of pristine magnetite NPs revealed particulates, predominantly cuboid-shaped, in the size range of 100–500 nm. The surface morphology of the particles vastly remained unaltered in the subsequent steps of APTES functionalization, anchoring of glutaraldehyde linker, and immobilization of the amine-tagged probes. EDS mapping was then performed on the representative samples, and the images revealed that the intensity of silicon and nitrogen was increased after APTES functionalization. Further, a significant enhancement in the signal of phosphorus was observed after the immobilization of amine-tagged probe-1. These

observations also confirmed the successful surface derivatization and corroborated XPS analyses' results.

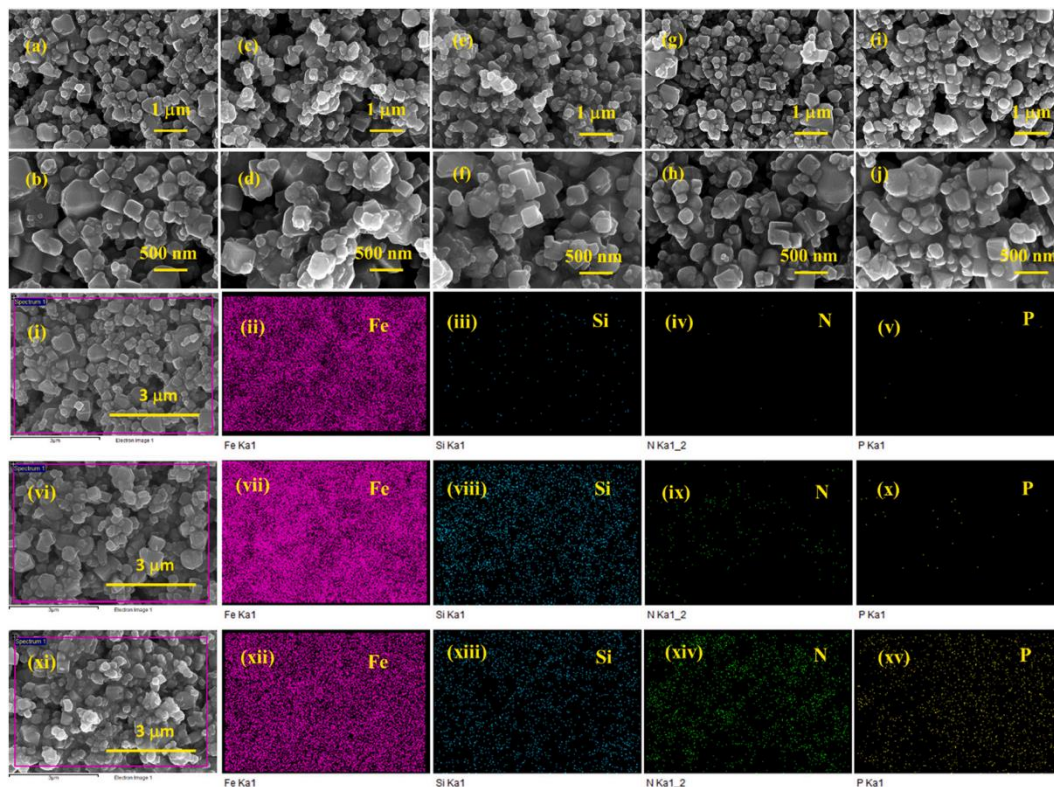


Figure 4.3 Top panel: FE-SEM images of magnetite NPs before and after surface derivatization steps at two different magnifications: **(a, b)** pristine, **(c, d)** APTES functionalized, **(e, f)** glutaraldehyde-derivatized, **(g, h)** G1 probe-1 immobilized, and **(i, j)** G3 probe-1 immobilized magnetite NPs. Bottom panel: EDS mapping of pristine **(i-v)**, glutaraldehyde-derivatized **(vi-x)**, and G1 probe-1 immobilized **(xi-xv)** magnetite NPs. The area employed in the mapping is highlighted in the FE-SEM images shown on the left-most column **(i, vi, and xi)**.

To quantitatively assess the amount of amine-tagged probe-1 immobilized over the glutaraldehyde-derivatized magnetite NPs, PAGE studies using the probe-1 solutions before and after the immobilization reaction were performed (**Figure 4.4**). It was seen from the gel pictures that the intensity of the bands corresponding to the probes before immobilization was very high. On the contrary, after immobilization over the magnetite NPs, the supernatant solutions obtained from the samples, G1 probe-1, G3 probe-1, and the mixture of these two exhibited a faint intensity in the gel picture. The quantification analysis of the gel bands revealed ~94% efficiency in the immobilization of the amine-tagged probe-1 over the glutaraldehyde-derivatized magnetite NPs.

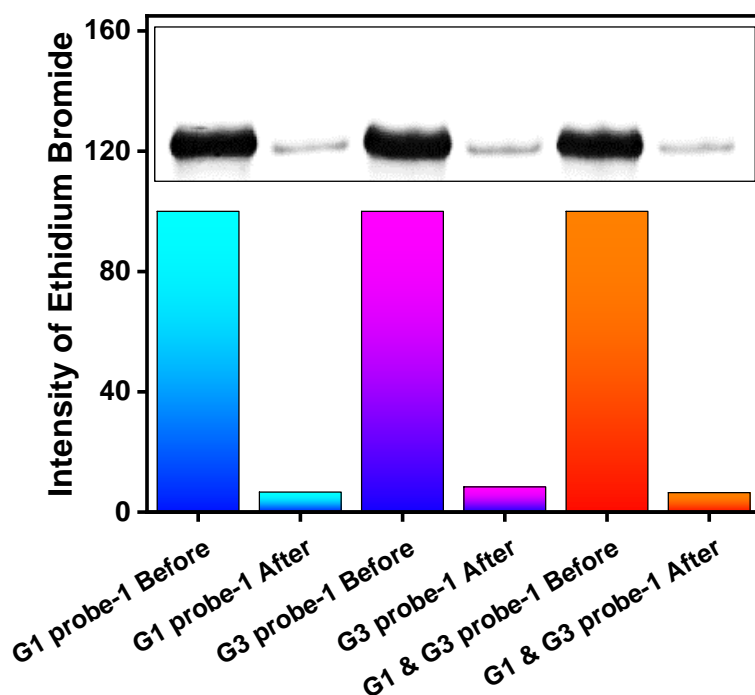


Figure 4.4 Digital photograph of the PAGE bands (shown in the inset) and their percentage intensity analyses of the amine-tagged probes in the supernatant solution before and after immobilization over the glutaraldehyde-derivatized magnetite NPs.

Before proceeding to the simultaneous dual oligo sensing, we performed the individual oligonucleotide detection to optimize the reaction conditions. For this, as mentioned in the experimental section, we explored two strategies, namely, one-step and two-step hybridization methods (**Figure 4.5**). In the one-step method, when the magnetite NPs immobilized with G1 probe-1 were hybridized together with G1 target and fluorescently-labeled G1 probe-2, the fluorescent intensity in the supernatant solution after magnetic removal of the NPs was found to be ~75% to that of the control. Whereas, in the two-step method, the fluorescently-labeled G1 probe-2 was separately hybridized with the G1 target in the first step and then subjected to hybridization with the G1 probe-1 immobilized over the magnetite NPs in the second step. In this case, the fluorescently-labeled G1 probe-2 was completely removed from the solution, and therefore, the supernatant solution exhibited negligible fluorescence intensity. This result indicated nearly 100% efficacy of the two-step method, as opposed to only ~25% efficacy of the one-step method. Since non-specific adsorption could be one potential reason for the poor efficacy of the one-step method, we attempted to minimize the same by incorporating EDTA

at two different concentrations (250 mM and 350 mM) in the reaction mixture and then carried out the hybridization [182]. However, no significant difference was observed in the results with the incorporation of EDTA. Hence, for the subsequent studies, we followed the two-step hybridization method.

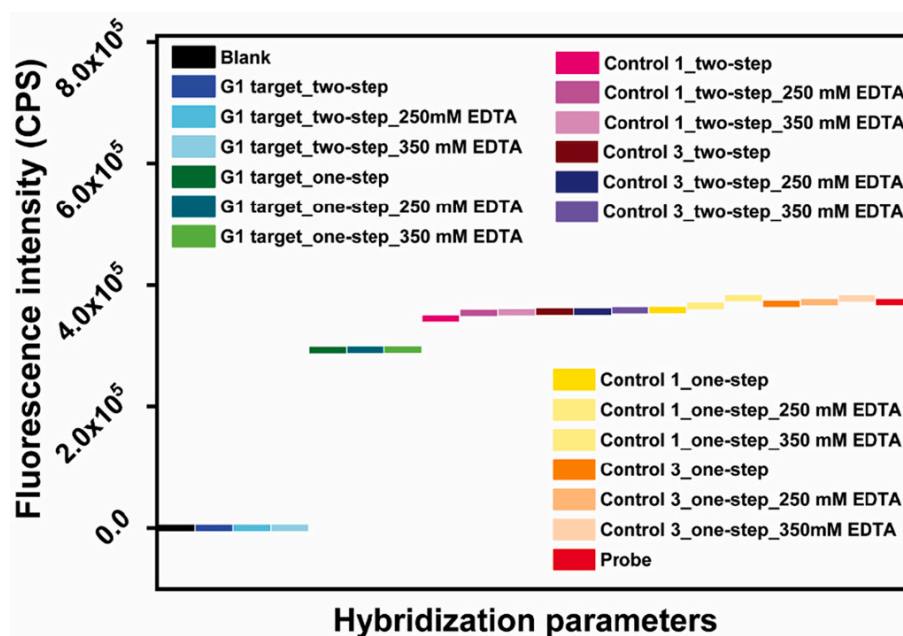


Figure 4.5 Optimization of the hybridization parameters for the dual oligo sensing by employing one-step and two-step hybridization methods using the oligos derived from HCV genotype 1. Two different controls, a poly A-poly G type (Control 1) and a random sequence (Control 3) were employed in the study to validate the selectivity.

The limit of detection (LOD) studies were then performed with the individual genotype samples and later with a mixture of the two in a simultaneous analysis, and the results are presented in **Figure 4.6**. Three different controls were chosen, out of which two were AG and AC rich oligos, and the third one was a random sequence. In the individual analysis with the genotype 1 and 3 samples, when the target concentration was varied from 1 nM to 100 nM, a linear trend in the fluorescence intensity was observed. The linear fitting of the data revealed the LOD of the G1 target and G3 target as 11 and 14 nM, respectively. A similar trend was also observed when both the probes corresponding to genotypes 1 and 3 were taken together. In this simultaneous detection, the LOD of the G1 target and G3 target was found to be 15 and 13 nM, respectively.

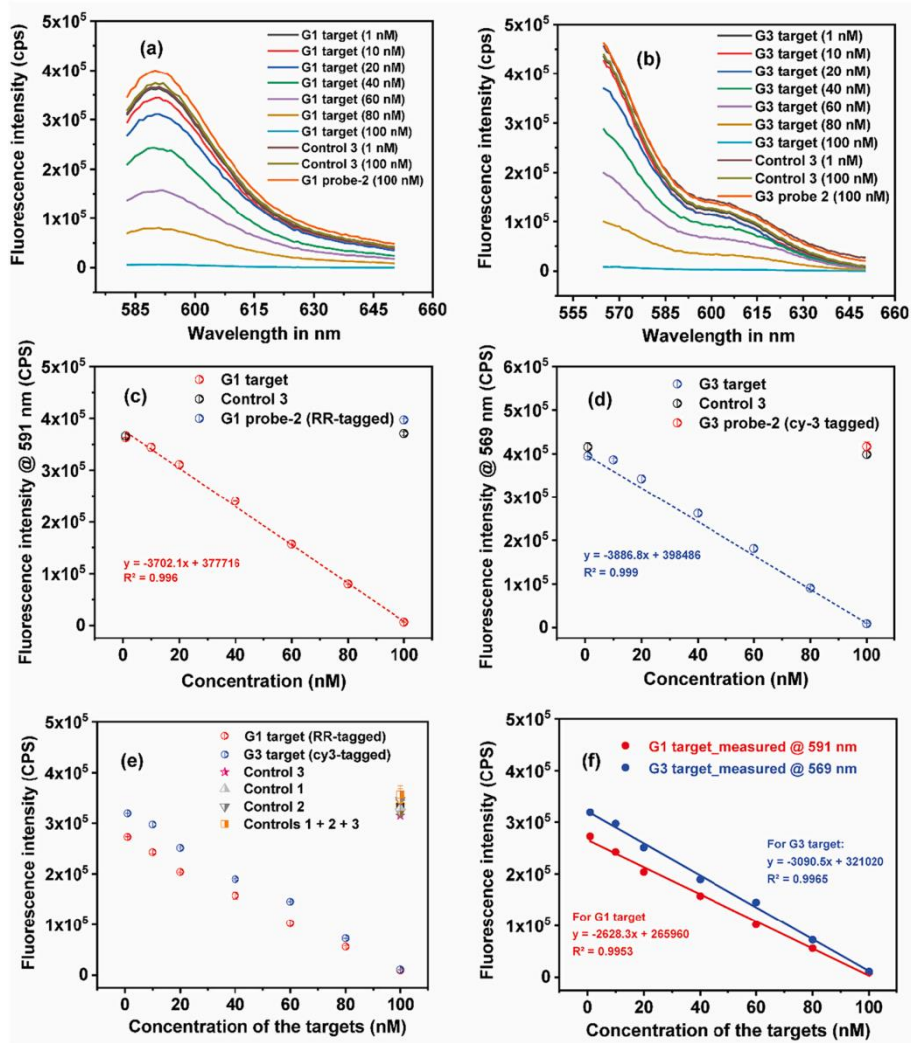


Figure 4.6 Quantitative oligo sensing of HCV genotypes 1 and 3 in an individual (c, d) and simultaneous (e, f) manner. The fluorescence spectra pertaining to the plots (c) and (d) are presented in (a) and (b), respectively.

It can be noted that the LOD can substantially be improved by further optimization and by developing hybrid strategies that employ strand displacement amplification. These experiments have also further ascertained the selectivity of the assay. To explore the shelf-life, the probe-immobilized magnetite NPs stored at 4 °C for 3 months were treated with the two extreme concentrations of the targets, and the results were compared with that of freshly-prepared ones (**Figure 4.7**). The variation in the results was found to be less than 2%, which showed the significant stability of the surface-derivatized NPs. The sensing studies were also performed in synthetic serum instead of water to ascertain the applicability in actual samples. In this case

also, the results were reproduced with less than 2% of the variation, which signified the high potential of the assay with the clinical samples.

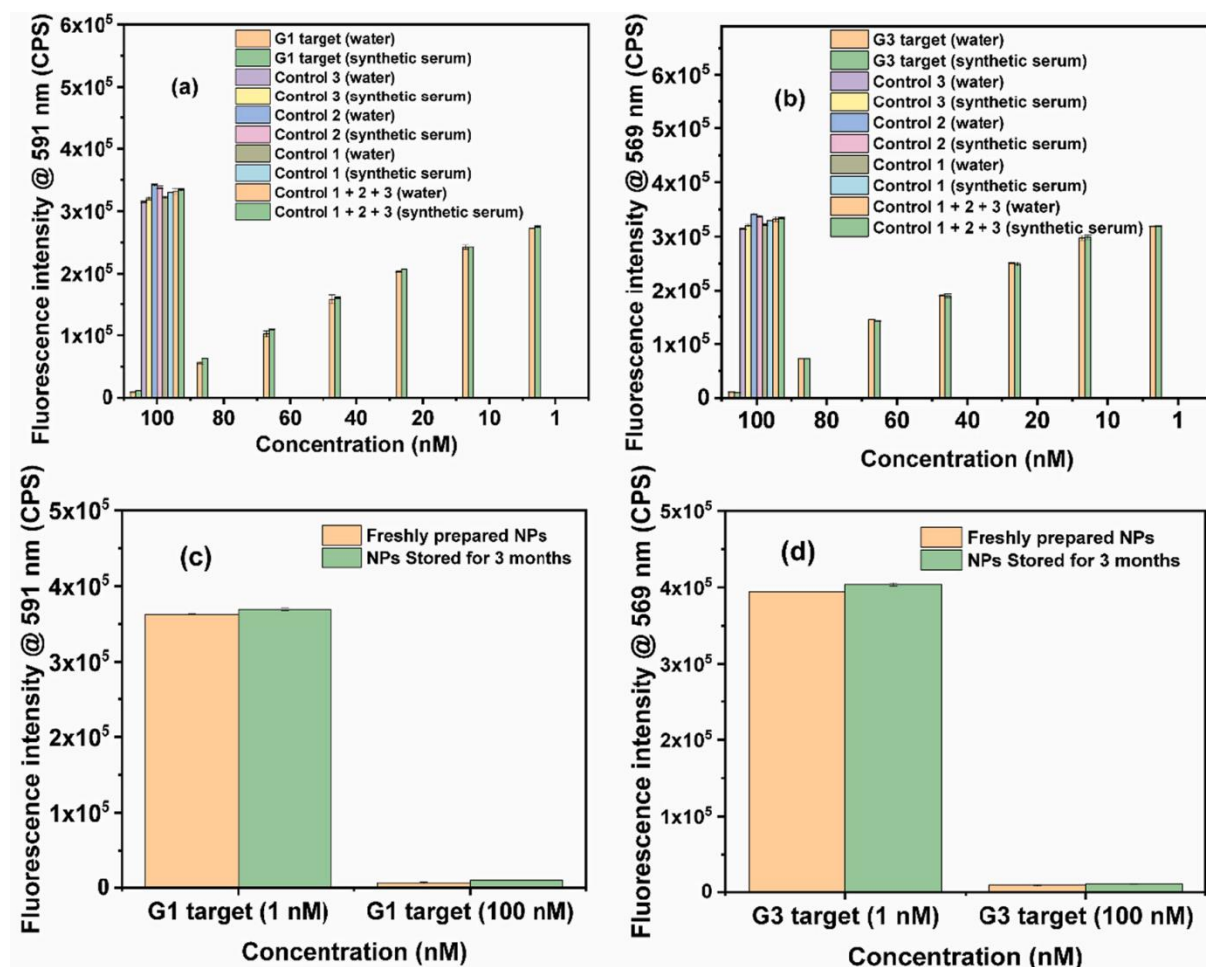


Figure 4.7. Stability analysis of the freshly prepared (a) and 3 months aged (b) probe-immobilized magnetite NPs. (c, d) Genotype sensing studies using synthetic serum in comparison to water.

4.4 Conclusions

Magnetite NPs-mediated fluorescence-based simultaneous dual oligo sensing was demonstrated by selecting two target sequences from HCV genotypes 1 and 3. To achieve this, the magnetite NPs were initially derivatized with APTES, followed by the glutaraldehyde linker. Two amine-tagged probes corresponding to the genotypes 1 and 3 were individually immobilized over the magnetite nanoparticles through imine bond formation in high efficiency by reacting with aldehyde groups, which was characterized using XPS and EDS analyses. Two approaches, such as one-step and two-step hybridization methods, were explored to understand the efficacy of the sensing assays. Among these, the two-step hybridization method, where the

fluorescently-tagged probe-2 and target were subjected to hybridization in a first step followed by hybridization with the probe-1 immobilized over magnetite NPs in a subsequent step, was found to be more efficient. The fluorescence intensity analysis after the magnetic removal of the NPs enabled the quantitative sensing of the targets with a LOD of < 15 nM. The LOD can substantially be enhanced by amalgamating with strategies that involve LAMP, HCR, RCA, etc. [183]–[185]. This strategy can potentially be extrapolated to multiplex sensing of various pathogens in a single go by immobilizing as many probes over the magnetite NPs.

Chapter 5

Boronic acid chemistry for fluorescence-based quantitative DNA sensing.

5.1 Introduction

Quantitative oligonucleotide detection is a sine qua non in various domains of biological studies and bio-based applications [186]. Several approaches, including fluorescence, colorimetric, electrochemical and surface-enhanced Raman scattering techniques, have been developed for this purpose [134], [136], [187], [188]. Despite the significant advancements in this domain, research efforts are ongoing to improve the selectivity, sensitivity, simplicity and potential multiplexing ability of the sensing assays. On a different note, boronic acid is a unique functional group, possessing a high degree of orthogonal reactivity, evident through its applications in multilayer surface functionalization approaches and materials science [189]–[195]. Owing to its high affinity to 1,2- and 1,3-diols to form a boronic ester, it has been vastly used in sensing and reactions with sugar moieties [196]–[198]. Besides, such selective interaction of boronic acid with the di-hydroxy group enabled its applications in siRNA delivery [199], [200], RNA sensing [201], [202], probing of DNA hydroxymethylation [203], and bioimaging [204]. However, little is known about its interaction with single and double-strand DNA (dsDNA). A study by Li et al., revealed electrostatic repulsion between single strand DNA and boronic acid, which was overcome at high salt concentration, presumed to be due to hydrogen bonding and hydrophobic interactions [205]. Another report on surface plasmon resonance-based strategy employed boronic acid derivatized Au nanoparticles in RNA sensing from pM to nM range, in which a certain degree of interference from DNA was observed, however not conclusive [201]. Thus, the exploration of the interaction of boronic acid in DNA-based studies is still in its infancy.

5.2 Methodology

In the present work, we probe the interaction of boronic acid with oligonucleotides towards quantitative DNA sensing by employing a fluorophore, 3-dansylaminophenyl-boronic acid (DAPBA) [206]. Three oligonucleotides, such as a thiolated DNA probe possessing 10-mer spacer A, a complementary DNA (cDNA) and a complementary RNA (cRNA), were designed from the 5' untranslated region of a model pathogen, Hepatitis C virus [135], [145]. A random

sequence as a non-complementary control (ncDNA) was also designed and used in the study. The strategy employed for the oligo sensing is presented in **Figure 5.1**.

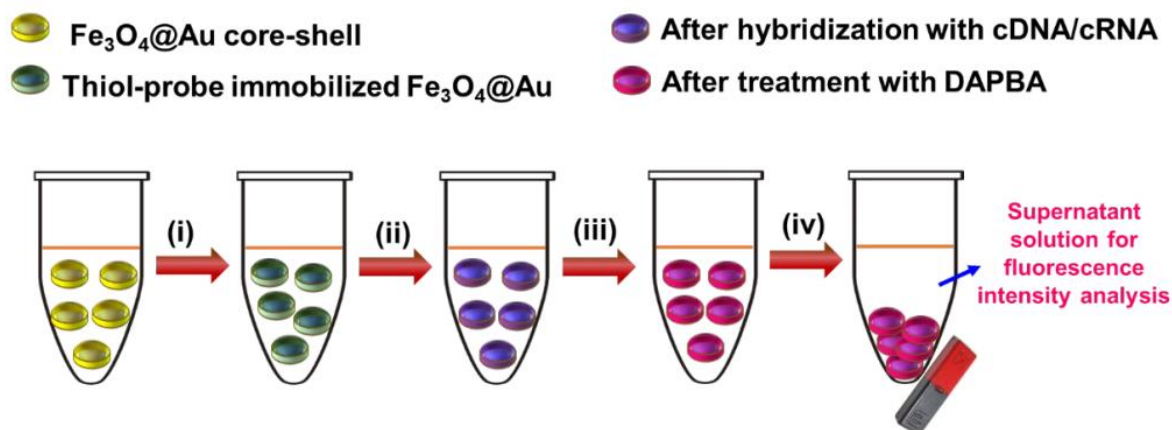


Figure 5.1. Diagrammatic representation of the boronic acid-mediated DNA sensing strategy. (i) treatment of $\text{Fe}_3\text{O}_4@Au$ with thiolated probe, (ii) hybridization of the immobilized probe with cDNA/cRNA/ncDNA (iii) treatment of the hybrid with DAPBA and (iv) removal of the core-shell nanostructures to obtain the supernatant solution for the fluorescence intensity measurements.

5.2.1 Materials

The reagents iron(II) sulfate heptahydrate and iron(III) chloride used in the synthesis of magnetite nanoparticles (MNPs) were procured from Sigma-Aldrich. Ammonia solution (25% v/v) was obtained from SD Fine Chemicals India Ltd. The gold(III) chloride trihydrate and tetraoctylammonium bromide (ToABr) for the synthesis of gold shell over the magnetite nanoparticles were procured from Sigma-Aldrich. The fluorescent molecule 3-dansylaminophenylboronic acid (DAPBA) was also purchased from Sigma-Aldrich. Methanol, toluene, dimethyl sulfoxide (DMSO), Tween 20, ethidium bromide (EtBr) and 1,4-dithiothreitol (DTT) were procured from Merck. All the oligonucleotides used in this study were purchased from Eurofins India Pvt. Ltd. A 6X loading buffer used in the gel electrophoresis study was procured from Takara.

Table 5.1 The sequences of the oligos.

Sample	Sequence (5'- 3')	GC content / Melting temp (°C)
Thiolated probe	SH-AAAAAAAAAAGCTGCACGACACTCATACT	34% / 55.9
cDNA	GCCATGGCGTTAGTATGAGTGTCGTGCAGC	57% / 65.7
cRNA	GCCAUGGCGUUAGUAUGAGUGUCGUGCAGC	57% / 65.7
ncDNA	GCGGAAGCTTCTACTTTTTTCTGCATCAAGC	47% / 66.8

5.2.2 Synthesis of Fe₃O₄@Au core-shell nanostructures

Fe₃O₄ NPs were synthesized through the co-precipitation method as per the literature protocol [180]. Briefly, 50 mL of water containing 0.5 M Fe²⁺ and 1.0 M Fe³⁺ salts were heated to 80 °C. To which about 35 mL of 25 % ammonia solution was added and stirred for 30 min. The obtained magnetite nanoparticles were washed thrice with water, twice with methanol, recovered and dried at 60 °C in a hot air oven. Fe₃O₄@Au core-shell nanostructures were synthesized using a recently developed solid-state synthesis route [207]. For this, gold-tetraoctylammonium bromide (Au-TOAB) precursor was synthesized by reacting HAuCl₄.3H₂O aqueous solution with tetraoctylammonium bromide, followed by phase transfer to toluene and drying the organic solvent. About 100 mg of Fe₃O₄ was mixed with 20 mg of Au-TOAB in a clean mortar and pestle and grounded well for 10 min. The contents were then transferred to a teflon-lined autoclave and calcined at 270 °C for 2 h. The obtained core-shell nanostructures were gently grounded and used for further studies.

5.2.3 Immobilization of thiolated probe over the core-shell nanostructures

The disulfide bond of the thiolated probe was reduced using DTT (in 100 mM sodium phosphate buffer, pH 8.3– 8.5) at a 1:5 ratio and incubated at room temperature for 1 h. After the treatment, the probe was precipitated using ethanol and column purified using DNA binding silica columns and eluted in sterile water. For immobilization, 100 µL of 20 µM of DTT treated

SH-Probe containing 18.82 μg DNA (188.2 $\text{ng}/\mu\text{L}$) was incubated with 50 mg of core-shell nanostructures at 37 $^{\circ}\text{C}$ for 2 h with continuous agitation in 20 mM citric acid (pH: 3.0). The citrate buffer was prepared by dissolving 25.08 mg of trisodium citrate in 5 mL of water and the final pH was adjusted to 3.0 using dilute HCl. After 2 h, the unbound probe was removed and further washed with 100 μL of 20 mM citric acid to wash away any loosely bound/adsorbed probe DNA over the gold surface. The collected fractions were collated and quantified using NanoDrop spectrophotometer. By subtracting the amount of unbound probe from the initial loading, the amount of probe bound to 50 mg of $\text{Fe}_3\text{O}_4@\text{Au}$ nanostructures was estimated to be 5.32 μg , which is equivalent to 106 ng/mg of the solid support. The core-shell nanostructures immobilized probe were dispersed in 500 μL of sterile water and stored at 4 $^{\circ}\text{C}$ till further use.

5.2.4 Oligonucleotide sensing

The probe-immobilized core-shell nanocomposite (100 nM w.r.t. the probe) was hybridized with single-stranded cDNA, cRNA or ncDNA. The concentration of the target and non-target oligos were varied from 5 nM to 100 nM in 100 μL reaction volume in water or synthetic serum. The synthetic serum was prepared using 2.2 g/L NaHCO_3 , 6.8 g/L NaCl , 0.2 g/L CaCl_2 , 0.1 g/L MgSO_4 , 0.4 g/L KCl , 0.126 g/L Na_2HPO_4 and 0.026 g/L NaH_2PO_4 at pH: 7.4. The hybridization was carried out by subjecting the mixture to a flash heating at 80 $^{\circ}\text{C}$ for 1 min, followed by 37 $^{\circ}\text{C}$ for 2 h [145]. The flash heating step was introduced to remove any secondary structures in the DNA or RNA strands and thereby enhance the hybridization efficacy. The core-shell nanostructures from the hybridization mixture were magnetically separated to remove any unbound oligos and resuspended in a 100 μL of 1% DMSO aqueous solution containing 100 nM DAPBA. The mixture was incubated further at 37 $^{\circ}\text{C}$ for 30 min, following

which the magnetic nanoparticles were once again magnetically removed. Additionally, the mixture was subjected to centrifugation at 12,000 RPM for 1 min to remove any suspended particulates and the fluorescence intensity of the supernatant solution was measured using a plate reader (SpectraMax[®] iD3, Molecular Devices, USA) at an excitation wavelength of 340 nm and monitoring the emission at 530 nm. The limit of detection (LOD) and limit of quantification (LOQ) were calculated using the formula given below.

$$LOD = 3.3 \times \text{standard deviation of intercept} \div \text{slope}$$

$$LOQ = 10 \times \text{standard deviation of intercept} \div \text{slope}$$

5.2.5 Agarose gel Electrophoresis

About 20 μ L of the hybridized solution was mixed with 4 μ L of 6X loading buffer. The obtained solution mixture was loaded onto a 3 % agarose gel and electrophoresed at 30 V for 3 h in 0.5X TBE buffer (540 mg of Tris base, 275 mg of Boric acid and 30 mg of EDTA; pH: 8.3). Following the gel run, it was stained using 0.5 μ g/mL of EtBr solution for 1 h with continuous rocking. After the staining, the EtBr solution was discarded and the gels were washed thrice with sterile distilled water for 10 min and visualized under a UV trans-illuminator.

5.3 Results & Discussion

Surface morphology of Fe₃O₄@Au core-shell nanostructures before and after immobilization of the thiolated probe were determined by Field emission scanning electron microscopy (FE-SEM). **Figure 5.2** reveals the surface morphology in both of these cases appear to be identical.

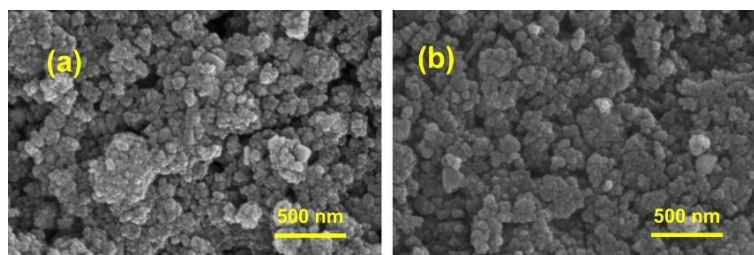


Figure 5.2 Field emission scanning electron microscopy images of $\text{Fe}_3\text{O}_4@Au$ core-shell nanostructures. (a) before and (b) after immobilization of the thiolated probe.

X-Ray photoelectron spectroscopy (XPS, K-Alpha, ThermoFisher) was employed to follow the immobilization of the thiolated probe over gold surface. **Figure 5.3** shows the P $2p$ and N $1s$ XPS core-level narrow scan spectra of the $\text{Fe}_3\text{O}_4@Au$ nanostructures before and after immobilization of thiolated probe. The narrow scan spectra of other elements such as Fe $2p$ and Au $4f$ are presented in **Figure 5.4**. While the Fe $2p$ and Au $4f$ narrow scans revealed the presence of these core and shell-forming elements, no signal pertaining to P $2p$ was observed in the as-synthesized $\text{Fe}_3\text{O}_4@Au$ nanostructures. Whereas, in addition to the presence of these elements, the nanostructures treated with the thiolated probe have shown the P $2p$ signal at 133.8 eV arising from the phosphate moieties of the DNA. The same characteristic signal was also observed in the nanostructures magnetically recovered from the probe-target hybrid but as a better-resolved and higher intensity peak. This has indicated the higher amount of phosphate on the surface, due to the formation of dsDNA. In the case of N $1s$ spectra, a characteristic signal at ~400 eV appeared with the pristine core-shell nanostructures, which could be attributed to the residual nitrogen from the Au-TOAB precursor complex deployed for the shell formation. Nevertheless, the intensity of the N $1s$ signal was clearly found to increase with the immobilization of the probe, which was further enhanced with the hybridization of cDNA/cRNA. These observations confirmed the stable binding of the hybridized oligonucleotides over the gold surface.

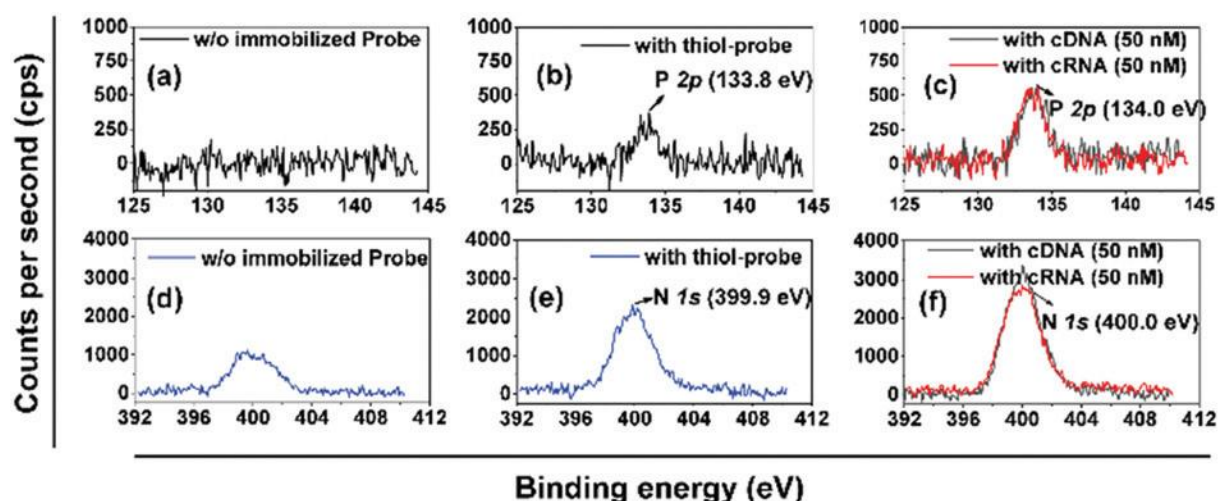


Figure 5.3 P 2*p* and N 1*s* narrow scan spectra of Fe₃O₄@Au core-shell nanostructures before probe immobilization (**a and d**), after immobilization of thiolated probe (**b and e**) and after hybridization with cDNA and cRNA (**c and f**).

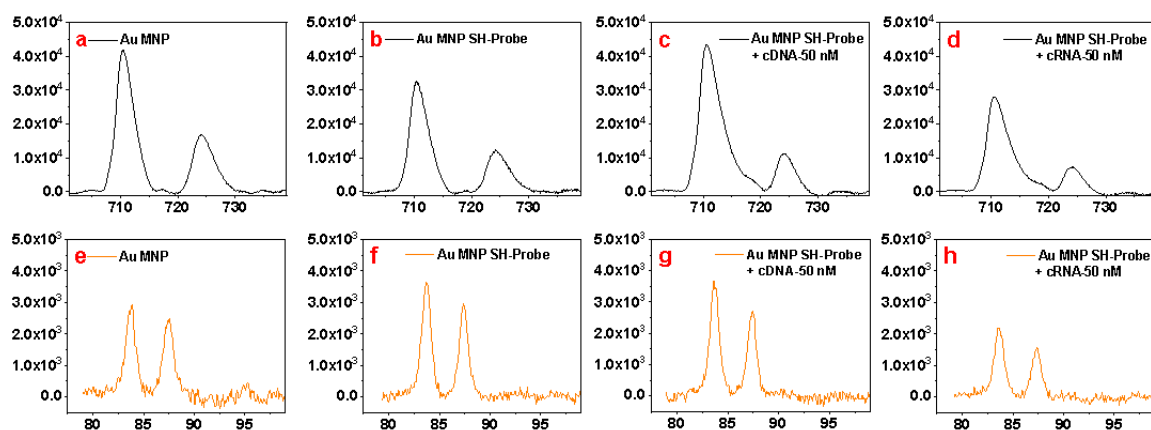


Figure 5.4 Fe 2*p* and Au 4*f* narrow scan spectra of Fe₃O₄@Au core-shell nanostructures before probe immobilization (**a and e**), after immobilization of thiolated probe (**b and f**) and after hybridization with cDNA (**c and g**), and cRNA (**d and h**).

For the sensing studies, the employed amount of probe (i.e., immobilized over the magnetic support) was fixed as 100 nM in a given 100 mL hybridization solution. Initially, the hybridization experiments were carried out in an aqueous solution containing 1% dimethyl sulfoxide (DMSO) since the same composition was used for the dissolution of DAPBA owing to its poor solubility in pure water. Further, we confirmed the hybridization efficiency in 1%

DMSO solution against Tris.EDTA (TE) buffer, as shown in the agarose gel electrophoresis **Figure 5.5**.

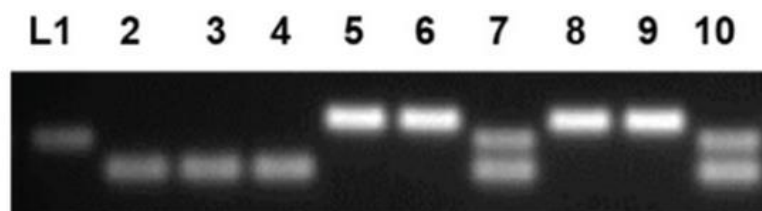


Figure 5.5 Digital photograph of the agarose gels depicting hybridization of probe and targets. In (a), the lanes 1, 2, 3 and 4 correspond to thiolated probe, cDNA, cRNA, and ncDNA, respectively. The lanes 5, 6 and 7 correspond to the hybridization of thiolated probe in TE buffer with cDNA, cRNA and ncDNA, respectively, while lanes 8, 9 and 10 also follow the similar order of the hybrids from 5 to 7, but in 1% DMSO solution.

The concentration of the cDNA, cRNA, or ncDNA for the sensing studies was varied in the range of 5 to 50 nM. After hybridization, the supernatant solution was removed, following which the nanostructures were resuspended in 100 nM DAPBA solution and further incubated for 30 min. The magnetic nanostructures were then removed from the DAPBA solution and the fluorescence intensity of the supernatant solution was measured to monitor the fluorophore’s binding over the hybridized oligos with reference to the standard curve **Figure 5.6**.

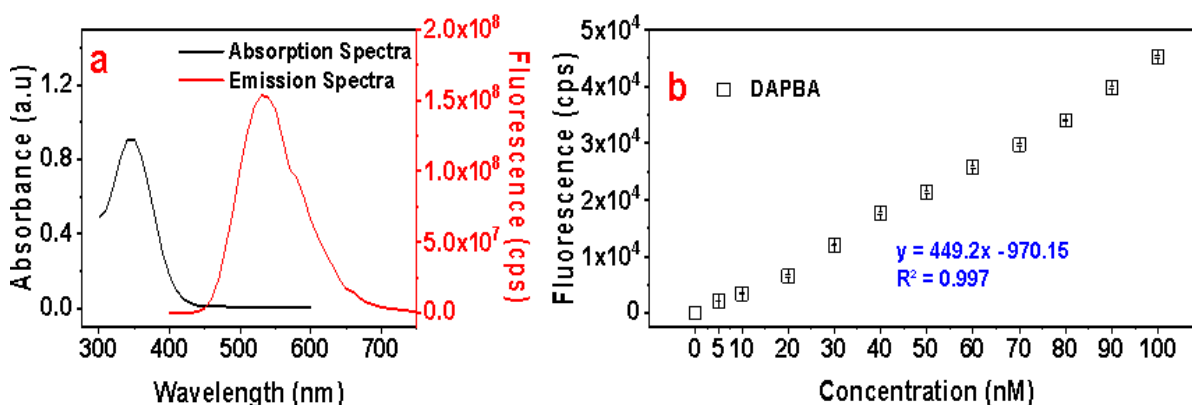


Figure 5.6 (a) Absorption and emission spectra of 1 mM DAPBA and (b) standard curve of DAPBA in aqueous solution containing 1% DMSO. Based on the absorption curve, 340 nm wavelength was used for the excitation and 530 nm was used for monitoring the emission.

Figure 5.7 (a) shows the change in fluorescence intensity as a function of target concentration in 1% DMSO solution. It was observed that cRNA was showing a rapid decrease in fluorescence intensity at lower concentrations, indicating the higher removal of DAPBA from the supernatant solution. It is known that DAPBA can bind to the di-hydroxy groups at the 3' position of the RNA and hence an equi molar removal of DAPBA was expected. However, the amount of DAPBA removed from the solution up to a cRNA concentration of 20 nM was almost 2 to 3 equivalents higher than the expected values. Interestingly, we also observed a near-linear trend in the removal of DAPBA from the supernatant solution of the cDNA sample, in which the reduction in DAPBA quantity was nearly equivalent to that of cDNA. This observation is counter-intuitive, as DNA has only a mono-hydroxy group at the 3' end. At concentrations higher than 35 nM, the removal of DAPBA from the solution both in cDNA and cRNA samples was found to be almost similar. In the case of ncDNA, ~10% of interference was observed, which was attributed to its non-specific binding over the probe-immobilized nanostructures. Therefore, the experiments were carried out in the hybridization mixture possessing 0.1% Tween-20, a non-ionic surfactant **Figure 5.7 (b)**. The introduction of Tween-20 was found to result in a substantial minimization of the ncDNA's non-specific binding. In addition, the trend in the decrease in fluorescence intensity with cDNA and cRNA was also modestly improved. On a different note, **Figure 5.8** shows the characteristic B 1s signals from the magnetite samples recovered from the DAPBA treatment step, which additionally corroborated the binding of boronic acid to the oligos. We further analyzed the fold decrease in the fluorescence intensity from the cRNA samples by taking cDNA samples as the reference. **Figure 5.7 (d)** reveals that up to 10 nM concentration of cRNA, the decrease in the fluorescence intensity is 3-fold compared to cDNA. Above this concentration, the fold change in the fluorescence intensity of the cRNA gradually decreased and became closer to that of cDNA from 30 nM onwards. This observation suggests that at higher concentrations of the oligonucleotide, the amount of DAPBA binding is nearly stoichiometric with DNA and RNA. To investigate the effect of duration on the binding of boronic acid with the oligos, we performed the DAPBA incubation step at three different time points, such as 5, 10, and 30 min, with three different concentrations of DNA and RNA as 20, 30 and 50 nM **Figure 5.7 (e)**. A significant amount of fluorophore was observed to bind to the oligos even at 5 min of duration,

which was modestly enhanced and saturated by 30 min of incubation. To probe the effect of longer incubation time on the degree of binding, the sensing studies were performed by incubating DAPBA overnight with 10 nM target. The results in **Figure 5.7 (f)** revealed no change in the fluorescence intensity of the supernatant solution, confirming the optimal duration as 30 min. Besides, the overnight incubation study also indicated the high selectivity and stability of boronic acid-oligo binding.

We additionally performed these sensing experiments in the synthetic serum to explore the applicability of the sensing strategy in clinical serum samples **Figure 5.7 (c)**. The results revealed a clear reproducibility of the data in comparison to the hybridization mixture that is devoid of electrolytes. Studies with varying concentration of DAPBA on fixed concentrations of the oligos revealed its optimal concentration as 100 nM **Figure 5.9**. Desorption of the bound DAPBA was studied at pH 3.0, which showed the reversibility of the boronate ester **Figure**

5.10.

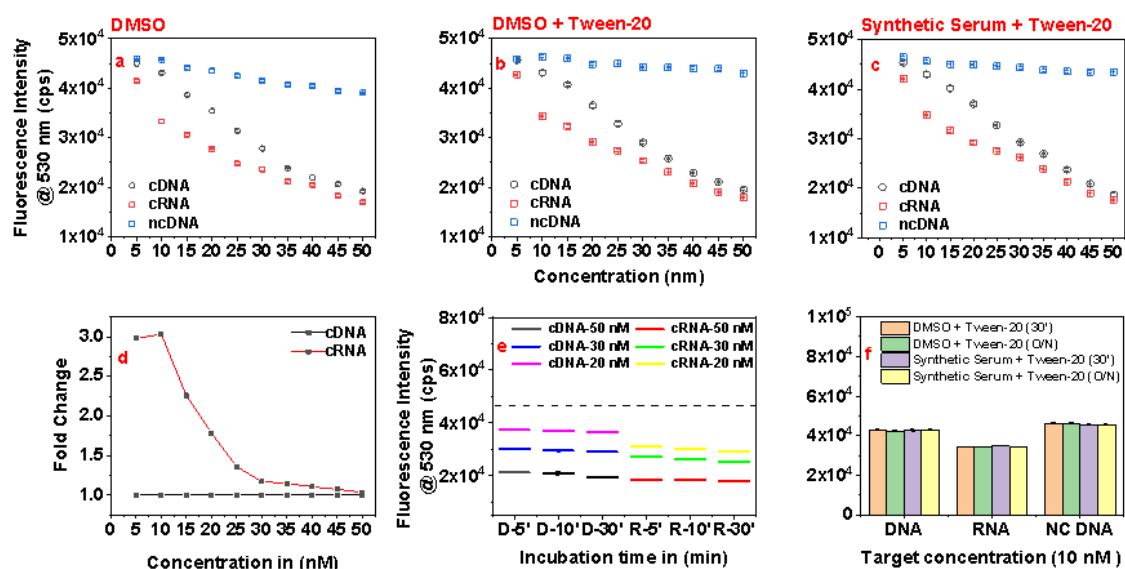


Figure 5.7 Fluorescence intensity profiles of DAPBA as a function of oligonucleotide concentration in aqueous solution containing (a) 1% DMSO (b) 1% DMSO+0.1% Tween-20 and (c) synthetic serum possessing 1% DMSO+0.1% Tween-20. (d) Comparison of the fluorescence intensity profiles of cDNA to cRNA from the data points shown in (b). (e) Fluorescence intensity profiles of DAPBA after incubation with cDNA and cRNA at three different time points such as 5, 10 and 30 min. The letters D and R in the X-axis legend represent DNA and RNA,

respectively. The dotted line represents the fluorescence intensity in the absence of a binding event. (f) Comparative fluorescence intensity profiles of DAPBA when treated with 10 nM cDNA, cRNA and ncDNA for 30 min and overnight (O/N) incubation.

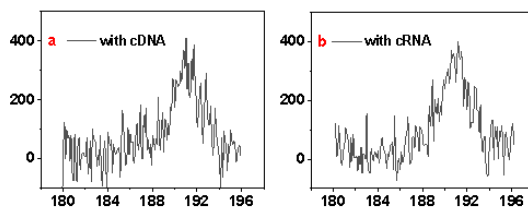


Figure 5.8 B 1s narrow scan spectra of Fe₃O₄@Au core-shell nano structures after hybridization with cDNA (a) and cRNA (b) at 50 nM concentration, followed by DAPBA incubation.

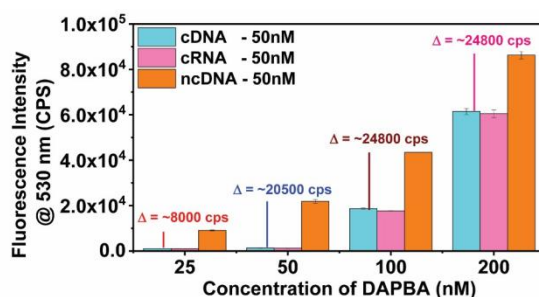


Figure 5.9 Fluorescence intensity profiles in the sensing study performed by varying the DAPBA concentration from 25 nM to 200 nM while maintaining the concentration of cDNA, cRNA and ncDNA at 50 nM. The difference in the intensities between the cDNA and ncDNA samples at a given DAPBA concentration is highlighted with a line profile.

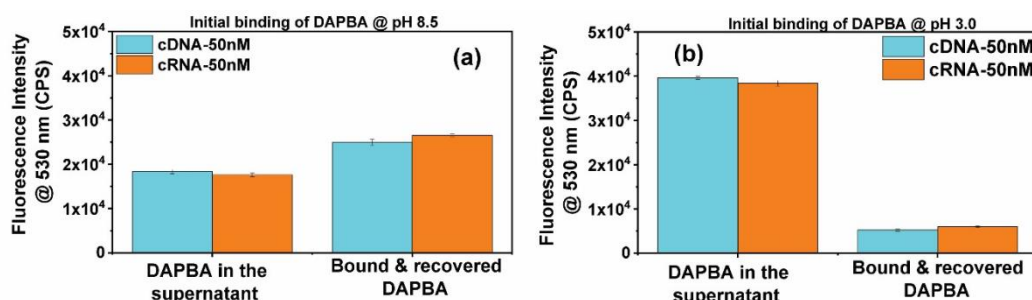


Figure 5.10 Reversibility studies of DAPBA at pH 3.0 (using citrate buffer): (a) Initial DAPBA binding with dsDNA immobilized over the core-shell nanostructures at pH 8.5, followed by desorption at pH 3.0 and (b) initial DAPBA binding with dsDNA immobilized over the core-shell nanostructures at pH 3.0, followed by desorption at pH 3.0. In both the cases, the final pH in the fluorescence intensity measurements was adjusted to 8.5.

Now, the question remains what the mode of interaction between boronic acid functionality and oligonucleotides is. For this, we consider two main possibilities: (i) intercalation of the DAPBA within the minor and major grooves of the double-strand and (ii) selective binding of boronic acid with 3' hydroxy groups in a bridging mode. To gain insights into this, we performed agarose gel electrophoresis experiments of oligos with and without DAPBA treatment after the hybridization step **Figure 5.11**. It can be noted that in all the gel experiments, the concentration of all the oligos was fixed at 100 nM. Interestingly, the gel bands corresponding to the DAPBA-treated samples revealed an increase in the molecular weight of the hybrids between the probe and cDNA/cRNA (lanes 5 and 6), as opposed to the hybrids that were not treated with DAPBA (lanes 2 and 3). It was further observed that the hybrid between the probe and cRNA (lane 6) exhibited an even higher molecular weight than that between the probe and cDNA (lane 5). Most strikingly, we observed a band with probe and ncDNA mixture (lane 7) equivalent to the hybrid between probe and cDNA (lane 5), although the binding was not quantitative. However, in this case also, the molecular weight equivalent to the dsDNA was observed, despite the fact that the two strands were completely non-complementary in nature (lane 7). This could be presumed as a result of the boronic acid-mediated bridging of the two different DNA strands. We then performed the gel electrophoresis of only ncDNA with and without treatment with DAPBA. The gel bands in lanes 8 and 9 clearly revealed the role of boronic acid in bridging even the same sequences, which supports the supposition that the boronic acid mediates the bridging between the two DNA strands *via* the mono-hydroxyl groups available at the 3' termini, and not through intercalation.

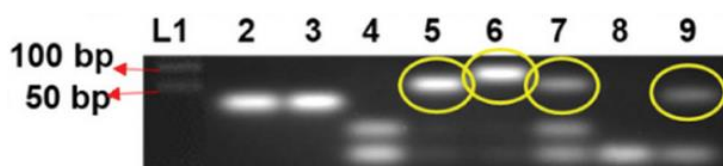


Figure 5.11 Digital photograph of the agarose gels depicting hybridization of probe and targets, followed by DAPBA incubation. (Lane 1)-ladder, (lanes 2-4) hybrids with cDNA, cRNA and ncDNA, respectively. (Lanes 5-7) hybrids with cDNA, cRNA and ncDNA, followed by 30 min of treatment with DAPBA. The (lanes 8-9) correspond to the ncDNA alone before and after treatment with DAPBA, respectively.

Figure 5.12 shows the plausible boronic acid-mediated bridging of the two different dsDNAs. It is clear from the gel electrophoresis studies that boronic acid bridges the oligos intermolecularly from two different double strands. Such an interaction has made quantitative detection possible with the strategy employed in this study. We speculate that the immobilized single strand probe DNAs experience electrostatic repulsion due to the negatively charged phosphate moieties, which do not permit bridging through boronic acid [205]. However, after hybridization with the target DNA, these phosphate moieties get hidden inside the grooves of the DNA, which minimizes the repulsion between the two dsDNAs, facilitating the bridging between the two by boronic acid. In the case of RNA, apart from such bridging at 3' terminal of the thiolated probe, the di-hydroxy group at the 3' terminal (closer to the poly A spacer of the immobilized probe) is also available for binding with boronic acid. Since each ribose unit of RNA has a free mono-hydroxy group at the 2' position in each nucleotide of each strand, we speculate that the boronic acid may bridge two different RNA strands through any of the hydroxyl groups at this position. However, the precise reasons for the variation in the binding stoichiometry from 3 to ~1, in this case, is unclear at the moment, and thereby warrants additional investigation.

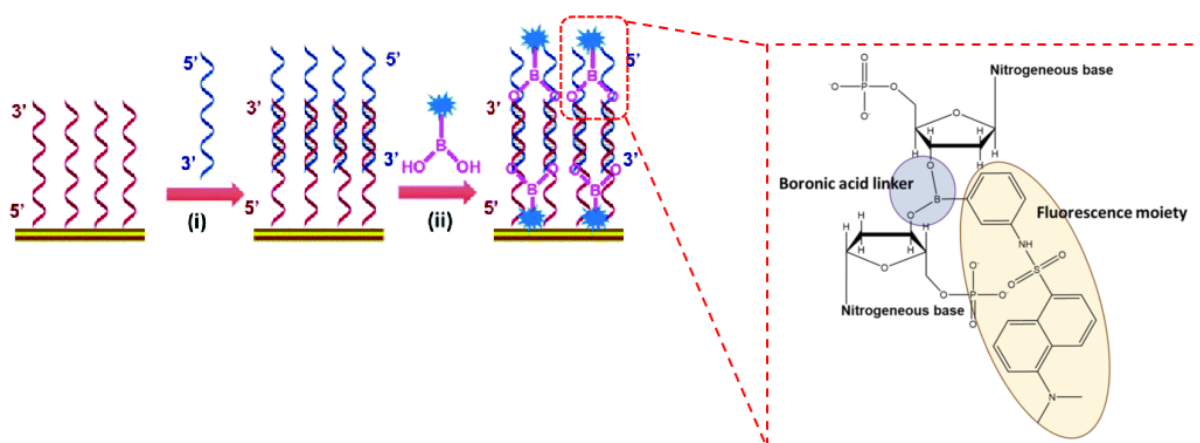


Figure 5.12 Plausible boronic acid-mediated bridging of the two different dsDNAs. In step (i) the cDNA is subjected to hybridization with thiolated probe immobilized over the gold surface. Step (ii) shows the plausible mechanism of boronic acid fluorophore bridging the two double strand DNAs via the mono-hydroxy groups at the 3' termini.

The limit of detection of the employed strategy with the adopted conditions was found to be 3.5 nM, while the limit of quantification was found to be 10.6 nM. Comparison of the LOD from a few representative literatures on the fluorescence-based DNA sensing are given below.

Table 5.2 Comparison of the LOD from a few representative literatures on the fluorescence-based DNA sensing.

Method	Linear range	LOD	<i>In situ</i> amplification	Reference
Activatable Ag nanoclusters beacon for DNA detection	10 – 100 nM	2 nM	No	[208]
DNA-templated Ag nanoclusters	0 – 200 nM	25 nM	No	[209]
Dual-probe fluorescent biosensor	5 pM – 5 nM	3.2 pM	Yes	[169]
Fluorometric detection of multiple oligonucleotides by using RNA-cleaving DNazymes	1 nM – 400 nM	70 pM	No	[172]
Dual oligosensing using magnetite Nanoparticles	10 nM – 100 nM	10 nM	No	[188]
Amyloid β oligomer assay based on abasic site-containing molecular beacon	0 – 70 nM	3.57 nM	No	[210]
A graphene oxide-based fluorescent platform for amyloid- β oligomers	10 nM – 2 mM	1 nM	No	[211]
Boronic acid-mediated fluorescence Sensing	5 nM – 50 nM	3.5 nM	No	This work

5.4 Conclusions

The current study offers certain unique advantages. First, in typical fluorescence-based DNA detection approaches, it is a prerequisite to tag the fluorophore to the oligos, which makes the process expensive and laborious [212]. Besides, for optimization processes where multiple sequences shall be employed, the tagging of the fluorophore over multiple probes or targets would substantially increase the cost. In contrast, the current study reveals the possibility of fluorescently tagging the oligos after the hybridization step in a rapid and facile manner [213]. Second, due to the reversible binding nature of the boronic acid, the oligonucleotides can be recovered by cleaving the fluorophore at acidic pH. Third, the possibility of detecting the cDNA and cRNA with a single probe DNA in a concentration dependent manner is hereby established. The present proof-of-concept study opens up several new opportunities for further exploration in this domain. First, thorough mechanistic details of the interaction through additional experimental, computational and theoretical works are required. Second, the detailed

probing on the dependence of the immobilized probe's packing density and its effect on the boronic acid binding response can be studied [214], [215]. Third, several strategies such as photo electrochemical, electro-generated chemiluminescence, hybridization chain reaction, etc., can explore the suitability of the boronic acid chemistry for DNA sensing to enhance the sensitivity to pM - fM range with a potential of multiplexing [216]–[218].

In summary, boronic acid chemistry has been successfully employed for the first time to quantitatively detect DNA alongside RNA. Fe₃O₄@Au core–shell nanostructures were derivatized with thiolated probe DNA, which was then separately subjected to hybridization with cDNA, cRNA and ncDNA. After removal of the unbound oligos, treatment of the surface immobilized ones with DAPBA resulted in its binding to the target hybrid in a concentration-dependent manner. This was monitored through the loss in fluorescence intensity in the supernatant solution upon magnetic removal of the DAPBA bound to the hybrid. Finally, the agarose gel electrophoresis experiments revealed the role of boronic acid in bridging the two dsDNA duplexes through boronic ester formation by reacting with their hydroxy groups at the 3' ends. The study opens up numerous avenues in the arena of DNA sensing and DNA-based fundamental and therapeutic studies.

Chapter 6

**Efficient biodiesel production from rice bran oil using magnetite
immobilized-recombinant lipase from probiotic *Bacillus licheniformis***

6.1 Introduction

Sustainable energy is a major domain that attracts vast attention among researchers working in the academic and industrial sectors. In particular, the quest for alternative energy to fossil fuels is ever-increasing, which can be met through a multimodal approach that includes various sources like biodiesel, hydrogen, nuclear energy, *etc* [176], [219]–[222]. The concept of circular economy highlights the necessity to adopt green principles to approach a problem with a 360° perspective starting from production and consumption to recycling [223]. Besides adhering to the circular economy principles, it is important that the process of persuading people to use alternative energy sources that should not generate hazardous elements, which otherwise could potentially be an environmental burden in future [224], [225].

Biodiesel is one of the promising alternative energy sources, it has been obtained through transesterification of several fresh and waste cooking oils such as rice bran, wheat germ, sunflower, olive, palm, *Spirulina* algae oil, *etc* [226]–[228]. Apart from these, animal fats from poultry waste are also considered to be potential sources of biofuel [229]. Among several candidates of vegetable oils, rice bran oil (RBO) has been chosen in the current study for enzymatic biodiesel production, as it has not been used for cooking purposes in most parts of the world [230]. It is also cost-effective and available in abundance. Besides, it has been found that the biodiesel from RBO can be blended with petrodiesel in a ratio of 20 : 80 for direct use in the current diesel engines, a combination that also substantially mitigates pollutant emissions [230]. Lipases belonging to the hydrolase class of enzymes are commonly employed in various sectors like food, detergent, cosmetic, bioenergy, bioplastic and other environmental applications [32], [60], [102], [109], [231]–[233]. It is evident from the literature that lipases obtained from fungal sources are commonly employed for various applications due to their high yield, stability and specific activity. However, it can be noted that the mycotoxins produced by many such species could be detrimental to the environment and human health. In contrast, enzymes derived from probiotic bacterial sources are attractive owing to their beneficial role in the gut microbiome in enhancing the immune response [108]. Nevertheless, there exist challenges to improving the specific activity of lipases derived from probiotic

sources to make the process economically sustainable [234]. On a different note, alkali-catalyzed biodiesel production from triacylglycerides has been popular in the industrial sector due to its easy operation and low cost. However, the formation of free fatty acids, in this case, leads to saponification, which warrants additional downstream processing to improve the biodiesel quality [235]–[237].

Extracellularly secreted lipases are produced by microbes upon incubation with an inducer like olive oil [102]. Such native lipases typically show low specific activity due to the presence of other unpurifiable proteins. To circumvent this, recombinant protein through heterologous expression is produced to obtain the desired enzymes with high purity and stability [231]. The specific activity of the enzymes, in many cases, is further enhanced through immobilization over various matrices such as alginate, metal–organic frameworks, magnetite, *etc* [231], [238], [239]. Such an immobilization process is also reported to enhance the stability and recyclability of the enzymes [240]. Recently, Zhao *et al.* reported lipase production from the *Bacillus licheniformis* NCU CS-5 strain—isolated from *Cinnamomum camphora* seed kernel—and showed its potential in the detergent industry [241]. The same group further reported heterologous expression of the lipase and demonstrated its application in the cheese industry for flavor enhancement [242]. This lipase was found to show a specific activity in the range of $\sim 350\text{--}400\text{ U mg}^{-1}$, which is one of the highest values derived from probiotic bacterial sources. Therefore, in the current work, we produced extracellular lipase from a different strain of *B. licheniformis* (MTCC 429) and performed heterologous expression. The activity of the lipase in these two cases has been compared for biodiesel conversion efficacy. Furthermore, the obtained lipases have been immobilized over magnetite for their facile recovery and reusability.

6.2 Methodology

6.2.1 Materials

The bacterial strain of *B. licheniformis* (MTCC 429) was procured from the Institute of Microbial Technology, Chandigarh, India. The reagents such as ammonium sulfate, ammonium persulfate, *p*-nitrophenol (*p*-NP), *p*-nitrophenyl palmitate (*p*-NPP), Factor X Activated (Xa) from bovine plasma, bovine serum albumin (BSA), magnetite, (3-

aminopropyl)triethoxysilane (APTES) and glutaraldehyde were procured from Sigma Aldrich, India. A Sephacryl G-250 column for lipase purification was obtained from Sigma Aldrich, India. The solvents ethanol and methanol were purchased from Merck, India. While the pMAL-c5x expression vector was procured from New England Biolabs, USA, the cloning (*E. coli* DH5 α) and expression host cells (*E. coli* BL21 DE3) were purchased from ThermoFisher Scientific, USA. The Phusion DNA polymerase for the polymerase chain reaction (PCR) was obtained from Agilent Technologies, USA, whereas the template DNA and primer were procured from Eurofins, India. RBO (Brand name: Priya) and olive oil (Brand name: Farrell Premium) were bought from the local shop. The common laboratory reagents, namely, nutrient agar, tris(hydroxymethyl)aminomethane, glycine, glycerol, Bradford's reagent, acrylamide, bisacrylamide, Luria broth, ampicillin sodium salt, isopropyl- β -D-thiogalactoside (IPTG), tributyrin, phenylmethylsulfonyl fluoride and bovine serum albumin were supplied by Himedia, India Pvt. Ltd.

6.2.2 Production of native lipase (NL) from *B. licheniformis*

B. licheniformis pure cultures obtained as dry pellets in sterile ampoules were added into 0.5 mL of nutrient medium and the bacterial culture was suspended by gentle pipetting [241]. The bacterial culture was then streaked onto a nutrient agar on a Petri plate and incubated at 37 °C for 24 h. A single bacterial colony from agar plates was cultivated in a nutrient medium for lipase production. This medium was supplemented with sources for nitrogen, carbon and divalent cations (Ca²⁺ and Mg²⁺) at pH 8.0 and then induced with 1% glycerol or olive oil or tributyrin for 144 h at 37 °C with continuous agitation at 200 RPM. The cells were separated by centrifugation at 7150 RPM for 20 min and the cell-free supernatant was precipitated by 50% ammonium sulfate at 4 °C overnight. The precipitated protein was separated by centrifugation at 8000 RPM for 30 min while maintaining the temperature at 4 °C. The precipitate was then dissolved in Tris-HCl buffer (50 mM, pH 8.0) and further dialyzed overnight using a dialysis membrane of 10 kDa molecular weight cut-off. The dialyzed fraction was concentrated using a 15 mL ultrafiltration tube containing an Amicon-Ultra-15 filter (MWCO 10 kDa, Millipore, USA). The concentration process was performed by centrifuging the solution taken in the

ultrafiltration tube at 8000g for 5 min and the obtained concentrated supernatant solution was then loaded onto a Sephacryl G-250 column. The protein concentration of the eluted fractions was measured spectrophotometrically and the target fractions were pooled and stored at $-20\text{ }^{\circ}\text{C}$ for further analysis. The protein concentration of the pooled fraction was measured by Bradford's method. The purity and molecular mass were determined by sodium dodecyl sulfate-polyacrylamide gel electrophoresis (SDS-PAGE).

6.2.3 Production of recombinant lipase (EL)

The *B. licheniformis* lipase gene sequence was subjected to codon optimization and the obtained sequence was custom synthesized by Eurofins (see the **Table 6.1**) [242]. The forward primer (5'-AAGTTGGCCATGTTGTGACC-3') was used for the asymmetric amplification of the lipase coding sequence.

Table 6.1: The codon optimized lipase gene sequence from *B. licheniformis*.

```

ATGGGCAGCAGCCATCATCATCATCACAGCAGCGGCCTGGTGCCGCGGGCAGCCATATGCGTCCTAGCG
CAGCAAGTGCCGCCAGCCATAATCCGGTGGTTATGGTGCATGGCATTGGTGGTGCAGATTATAATTTTATTGG
TATTAAGAGCTACCTGCAGAGCCAGGGCTGGACCAGTAGTGAAGTGTATGCAATTAATTTTATCGACAAGACC
GGTAATAACATTAATAATGCCCCGCGCCTGAGCGAATATATTAAGCGTGTGCTGAATCAGACCGGTGCAAGCA
AAGTTGATATTGTTGCCCATAGCATGGGCGGTGCCAATACCCTGTATTATATTAAGAATCTGGACGGTGCAGA
TAAAGTTGGCCATGTTGTGACCCTGGGCGGTGCCAACCGTCTGGTTACCAATACCGCCCCGAGAATGATAAA
ATTAGCTATAACCAGTATCTACAGTACCAGTGATTATATTGTTCTGAATAGTCTGAGTAAGCTGGATGGTGCAA
ATAATGTGCAGATTAGCGGCGTTAGCCATGTGGGTCTGCTGTTTAGCAGTAAAGTTAATGCCCTGATTAAGGA
TGGCCTGACCGCAAGCGGTAAATAACTCGAG

```

The recombinant lipase was cloned into a pMAL-c5x expression vector, harboring a maltose-binding protein tag (MBP), for overexpression and subsequent affinity chromatography-based purification. Freshly transformed *E. coli* BL21 (DE3) cells with the recombinant plasmid were then inoculated in 5 mL of LB medium with ampicillin ($100\text{ }\mu\text{g mL}^{-1}$) and cultured overnight at $37\text{ }^{\circ}\text{C}$ and 200 RPM. After incubation, the primary bacterial culture was inoculated in 1 L of LB medium with ampicillin and further incubated at $37\text{ }^{\circ}\text{C}$ to reach an optical density (OD) at 600 nm (OD_{600}) of about 0.6. Protein expression was induced by the addition of IPTG at a final concentration of 1 mM and cultured at $37\text{ }^{\circ}\text{C}$ for 4 h. The cells were obtained by centrifugation

at 6000 RPM at 4 °C for 30 min and then resuspended in cold lysis/binding buffer (50 mM Tris–HCl, 10% glycerol and 1% PMSF at pH: 8). The bacterial suspensions were sonicated on ice for 30 min (5 s pulse and 10 s resting, 40% amplitude). The supernatant and precipitate in suspensions were separated by centrifugation at 8000 RPM, 4 °C for 30 min. The gravity-flow-based amylose resin (~2 mL) was packed in a sterile column and equilibrated by ten column volumes of binding buffer. The supernatant containing the soluble fraction of recombinant lipase was loaded onto the amylose resin for recombinant protein binding. The column was washed with 10 column volumes of wash buffer (50 mM Tris–HCl, pH: 8) to remove the non-specific proteins. Finally, the recombinant protein was eluted with the elution buffer containing 10 mM maltose. The MBP tag from the target protein was removed by subjecting the eluent to proteolytic cleavage with Factor Xa at 37 °C overnight. After incubation, the contents were passed through an amylose resin. The target protein devoid of the MBP tag was collected in the flow-through and supplemented with 10% glycerol for long-term storage. The total protein content and purity were analyzed by Bradford's method and SDS-PAGE, respectively.

6.2.4 Lipase activity

The lipase activity was determined using the conventional *p*-NP assay, where *p*-NPP was used as the substrate [243]. The reaction mixture contained 0.01 mL of *p*-NPP (0.1 mM, methanol solution), 0.01 mL of enzyme extract and 0.08 mL of Tris–HCl buffer (0.05 M, pH 8.0). The reaction mixture was incubated at 37 °C for 30 min and stopped by keeping it in ice water for 10 min. The absorbance of the reaction mixture was measured at 410 nm using a spectrophotometer. Lipase activity was measured by comparing the absorbance from the *p*-NP standard curve generated. Based on this, the lipase activity was mapped with the generation of 1 μmol *p*-NP per min (1 U) under standard conditions and expressed as U mg⁻¹ of protein.

6.2.5 Lipase immobilization over magnetite nanoparticles (MNPs)

6.2.5.1 Fe₃O₄@lipase

Commercial MNPs were initially functionalized with amine groups using APTES following the literature protocol [188]. Briefly, 500 mg of MNPs dispersed in 25 mL of absolute ethanol was treated with 5 mL of APTES and incubated under shaking conditions for 24 h at 30 °C. After incubation, the MNPs were magnetically separated, washed thrice with ethanol and dried in a vacuum oven. The amine-functionalized MNPs were suspended in 20 mL of phosphate saline buffer solution (0.1 M, pH 7.4), supplemented with 5 mL of 25% glutaraldehyde solution and the surface derivatization reaction was performed for 2 h under shaking conditions. Following this, the unbound glutaraldehyde was removed by washing the MNPs thrice with sterile water. The enzyme immobilization was carried out by adding 10 mL of buffer solution (0.05 M Tris–HCl pH 8.0) containing 10 mg of the purified lipase to aldehyde-derivatized MNPs followed by subjecting the reaction mixture to shaking for 2 h. The magnetite NPs were then recovered using a magnet, washed twice with sterile water and used for subsequent studies.

6.2.5.2 Fe₃O₄@lipase@BSA.

A portion of the Fe₃O₄@lipase obtained above was further immobilized with BSA. For this, an aqueous solution containing 5 mg mL⁻¹ of BSA was incubated with Fe₃O₄@lipase (400 µg; w.r.t the lipase) for 30 min with constant agitation. The obtained Fe₃O₄@lipase@BSA assembly was then magnetically recovered, washed gently with 500 µL of methanol and used for further studies.

6.2.5.3 Fe₃O₄@BSA@lipase.

About 500 mg of the aldehyde-derivatized MNPs, as mentioned earlier, were added to 20 mg of BSA taken in 10 mL of Tris–HCl (0.05 M, pH 8.0). The immobilization reaction was performed for 2 h under shaking at room temperature, followed by magnetically removing the MNPs and washing twice with sterile water. To immobilize the second layer containing BSA and lipase, the BSA-coated MNPs (Fe₃O₄@BSA) were treated with glutaraldehyde in the same

manner as mentioned above. Following this, 15 mg of lipase was added to Fe₃O₄@BSA and incubated further for 2 h at room temperature. After this time, about 30 μL of 25% glutaraldehyde was added to the solution and allowed to incubate in a shaker for another 30 min. Thus the obtained Fe₃O₄@BSA@lipase was once again magnetically separated from the reaction mixture, washed with Tris–HCl (0.05 M, pH 8.0) and stored at 4 °C for further use. The supernatant was analyzed for the quantity of unbound enzyme through Bradford's method at each step, whereas the activity of the immobilized lipase was studied using the *p*-NP assay. By calculating the difference between the enzyme quantity in the solution phase before and after immobilization, the immobilized enzyme content was estimated.

6.2.6 Effect of temperature and pH on lipase activity

The effect of temperature on the activity of lipase was investigated by measuring its specific activity using a *p*-NP assay at different temperatures ranging from 37 to 75 °C in Tris–HCl buffer (0.05 M, pH 8.0). After mixing the reagents, the tubes were incubated at different temperatures such as 37, 45, 52, 60 and 75 °C in a heating block for 30 min and cooled using an ice bath for 10 min to stop the reaction. In a similar fashion, the effect of pH on lipase activity was studied in various buffers at different pH values ranging from 4.0 to 12.0 for 30 min at 37 °C. In this case, four different buffers were used for different pH ranges, namely, sodium acetate (0.05 M, pH 4.0), sodium phosphate monobasic (0.05 M, pH 6.0), Tris–HCl (0.05 M, pH 8.0) and glycine/NaOH (0.05 M, pH 10.0–12.0).

6.2.7 Transesterification reaction

Biodiesel production was performed through transesterification of RBO with methanol using free and immobilized lipases [237]. The oil and methanol mixture was heated to 60 °C before adding the catalyst and cooled to room temperature. In a typical initial reaction, about 25 μg of free or immobilized lipase was added per 100 μL of oil (~91 mg) and the reaction was carried out for 2 h. The immobilized catalyst was separated using an external magnet, whereas any unreacted oil was separated by centrifugation at 12 000 RPM for 10 min, followed by the removal of the upper layer. Excess methanol from the reaction was evaporated by heating the sample to 65 °C for 30 min. The obtained biodiesel was kept at 4 °C overnight to form two

layers: the upper ester layer and the bottom glycerol layer. The slight yellowish fatty acid methyl ester (FAME) in the upper layer was carefully pipetted out and its yield was determined gravimetrically.

6.2.9 Optimization of the transesterification reaction parameters

Various reaction parameters such as the amount of catalyst loading, oil to methanol ratio, temperature, stirring rate and incubation time were optimized by varying one parameter at a time. **Table 6.2** summarizes the different parameters employed in the optimization reactions.

Table 6.2 Summary of the reaction parameters in the optimization of the transesterification reaction

Optimizing parameter	Oil to methanol ratio	Catalyst loading (μg)	Temperature ($^{\circ}\text{C}$)	Stirring rate (rpm)	Reaction time (h)
Catalyst loading	1 : 6	25 to 400	37	120	2
Oil to methanol ratio	1 : 3 to 1 : 9	100	37	120	2
Temperature	1 : 6	100	25 to 60	120	2
Stirring rate	1 : 6	100	37	80 to 240	2
Reaction time	1 : 6	100	37	120	2 to 24

6.2.10 Recyclability studies of the catalyst

To test the recyclability of the enzyme, about 400 μg of the immobilized catalyst (w.r.t lipase loading) was added to the reaction mixture. The reaction was performed under optimal conditions of oil to methanol ratio (1 : 6), temperature (37 $^{\circ}\text{C}$), stirring rate (120 rpm) and incubation time (2 h). At the end of each cycle, the immobilized lipase was captured at the bottom of the reaction vessel by placing an external magnet underneath, followed by decanting the supernatant solution. The magnetic particles were gently washed with 500 μL of methanol and then proceeded with the subsequent cycle by adding fresh oil to the same container and vortexing the same.

6.2.11 Characterization

The secondary structure of the native and codon-optimized lipase was studied using circular dichroism (CD) spectrophotometer (Jasco J-1500). The UV-visible absorbance measurements in the *p*-NPP assay were performed using SpectraMax® iD3 plate reader (Make: Molecular Devices). The enzyme coverage over the magnetite support was characterized using X-ray photoelectron spectroscopy (XPS; Thermofisher K-Alpha) fitted with an Al K α X ray source. On the other hand, field-emission scanning electron microscopy (FE-SEM; FEI, Apreo S) was employed for verifying any morphological changes during the surface derivatization processes over the magnetite particles. Gas chromatography (GC; GC-2010 Plus, Shimadzu) analyses were performed using the biodiesel with a mixture of nitrogen and air as the carrier gas under a constant pressure of 98.5 kPa and the obtained peaks of methyl esters were compared against the standards. The GC run was performed with the following parameters: injection port temperature – 200 °C; column temperature – 100 °C; total carrier gas flow rate – 60.9 mL/min; split ratio – 1:20; flame ionization detector – 250 °C. Nuclear magnetic resonance (NMR) analyses of the RBO and biodiesel were recorded using Bruker (AV NEO 400 MHz) NMR spectrophotometer. The thermal analysis of the biodiesel was carried out in thermogravimetric analyser (Shimadzu DTG-60) at a ramping rate of 10 °C/min and a nitrogen flow rate of 100 mL/min.

6.3 Results and discussion

6.3.1 Induction and purification of the NL

At first, pure cultures of *B. licheniformis* were induced separately with 1% glycerol/olive oil/tributyryn to obtain the NL secreted by the probiotic source. All three inductions resulted in

the secretion of extracellular lipase, which was confirmed by a distinct band at around 27 kDa shown in the SDS-PAGE analysis of the supernatant solution (**Figure 6.1**). The yield of purified lipase obtained through induction by glycerol, olive oil and tributyrin was found to be ~57, 40 and 41 mg L⁻¹ of bacterial culture, respectively. The *p*-NP assay (*vide infra*) using the NLs obtained through glycerol, olive oil and tributyrin induction showed specific activities as 236.9 ± 2.3, 184.4 ± 4.3 and 208.7 ± 3.5 U mg⁻¹, respectively. Since the lipase obtained using glycerol induction was found to be advantageous in yield, activity and cost-effectiveness, the same was then employed for further large-scale enzyme production.

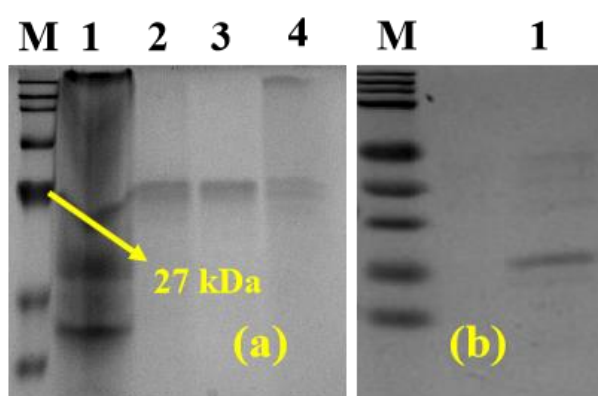


Figure 6.1 (a). SDS-PAGE of lipase induction from *B. liceniformis* using different inducers (Lanes: M – marker; 1 – uninduced control; 2 – glycerol; 3 – tributyrin; 4 – olive oil). (b) SDS-PAGE of purified NL (Lanes: M – marker; 1 – NL).

6.3.2 Cloning, expression and purification of recombinant lipase

Following the production of NL, recombinant lipase production was performed using the codon-optimized gene sequence. For this, the lipase encoding gene with an open reading frame of 615 bp was amplified by asymmetric PCR **Figure 6.2 (a)**. The PCR fragment was ligated into EcoRV digested pMAL-c5x expression vector and then transformed in DH5 α competent cells **Figure 6.2 (b)**. The transformed colonies of pMAL-c5x were grown on ampicillin supplemented LB agar plates. Agarose gel electrophoresis and restriction analysis of plasmids from positive colonies indicated the expected size of the plasmid construction gene **Figure 6.2 (c)**.

The expression of the lipase gene was then carried out in *E. coli* BL21 (DE3) host cells. SDS-PAGE analysis of cellular lysates showed that the target protein was successfully

expressed from pMAL-c5x clones with 1 mM IPTG induction for 4 h at 37 °C **Figure 6.2 (d)**. The purified recombinant lipase with the MBP tag displayed a single band on SDS-PAGE with a molecular weight of approximately 70 kDa **Figure 6.2 (e)**. The MBP tag was cleaved from the recombinant protein using Factor Xa enzymatic treatment, showing the detachment of the tag, which was confirmed through a clear band of 27 kDa corresponding to lipase **Figure 6.2 (f)**.

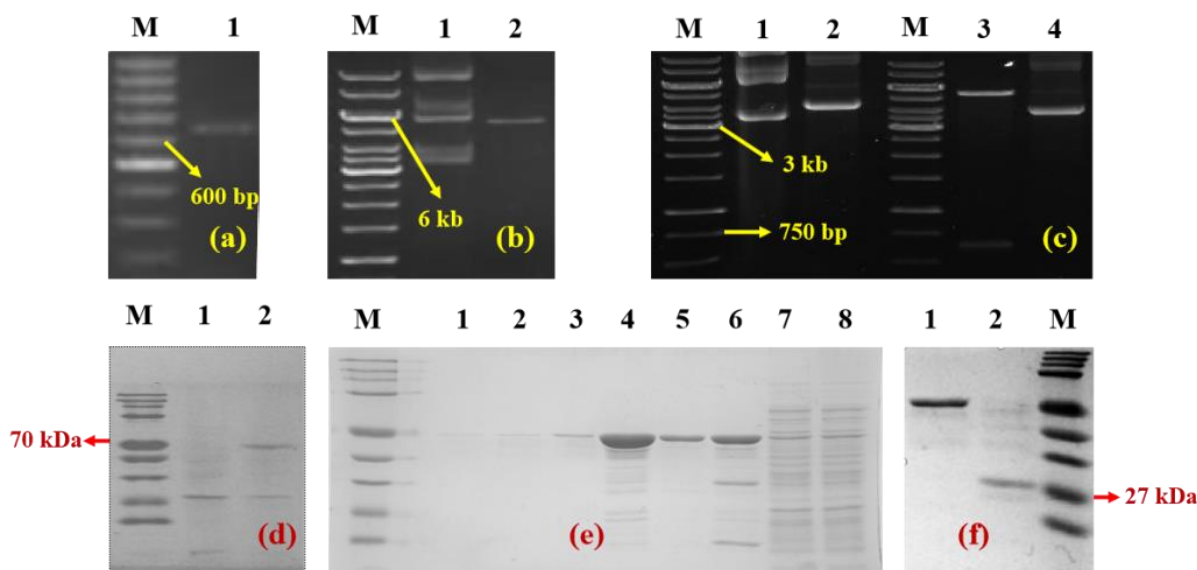


Figure 6.2 (a) Agarose gel of the PCR product of expressed lipase (Lanes: M – marker; 1 – PCR product (615 bp)). **(b)** Agarose gel of pMAL-c5X digestion with EcoRV (Lanes: M – marker; 1 – uncut plasmid; 2 – cut plasmid). **(c)** Agarose gel of the positive clone obtained from DH5α transformation (Lanes: M – marker; 1 – pMALc-5X; 2 – with lipase insert; 3 – restriction digested positive clone releasing lipase gene insert; 4 – positive clone). **(d)** SDS-PAGE of IPTG induced *E. coli* BL21 (DE3) with lipase clone (Lanes: M – marker; 1 – uninduced, 2 – IPTG induced). **(e)** SDS-PAGE of amylose resin-based purification of EL (Lanes: M – marker; lanes 1 to 5 – elutions; 6 – wash; 7 – flow-through; 8 – lysate). **(f)** SDS-PAGE of the purified EL (Lanes: M – marker; 1 – MBP tagged lipase; 2 – CL).

6.3.3 Circular dichroism (CD) study

Far UV CD spectra of NL and expressed lipase (EL) were recorded to probe their secondary structure **Figure 6.3 (a)**. The background noise was subtracted from the sample spectrum prior to secondary structure analysis using the *in silico* Beta Structure Selection (BeStSel) online tool [244], [245]. Both native and EL exhibited a similar CD spectral profile, despite specific

differences in molar ellipticity and the peak position. While the negative band of the NL was noticed at 208 nm, the value was slightly shifted to 210 nm in the case of EL. Besides, another band corresponding to the α -helix appeared as a clear shoulder at the characteristic 222 nm with NL. In contrast, the same appeared as a prominent negative band in EL, thereby signifying its higher activity. In line with these observations, BeStSel analyses revealed the total content of α -helices in NL and EL as 23% and 34.2%, respectively **Figure 6.3 (b)**. Furthermore, the full β -sheet contents in NL and EL were found to be 11.2% and 19.4%, respectively. The detailed break of the analyses is presented in **Table 6.3**. Overall, the higher α -helical and lesser β -sheet content along with more molar ellipticity revealed potentially higher activity and enhanced purity of the EL compared to the native one [246].

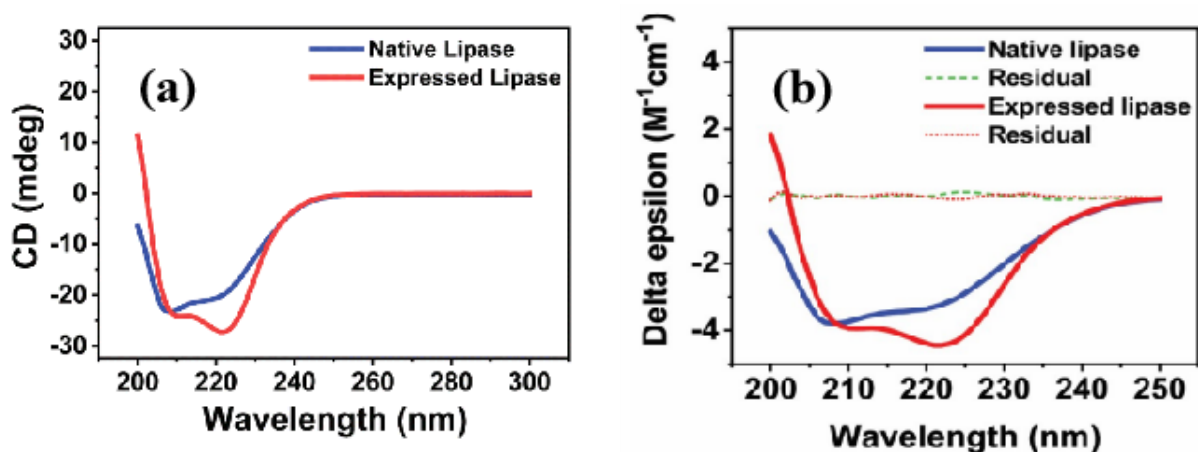


Figure 6.3 (a). Circular dichroism spectral profiles of NL and EL. **(b).** CD spectra of native and expressed lipases analyzed using BeStSel online tool.

Table 6.3 Parameters of secondary structure corresponding to **Figure 6.3 (b)**.

Secondary structure content (%)	Native lipase	Expressed lipase
<i>Helix (regular)</i>	13.9	21.4
<i>Helix (distorted)</i>	9.1	12.8
<i>Antiparallel (left twisted)</i>	0	0
<i>Antiparallel (relaxed)</i>	0	0
<i>Antiparallel (right twisted)</i>	13	4
<i>Parallel</i>	6.4	7.2
<i>Turn</i>	15.3	13.5
<i>Others</i>	42.3	41.1
<i>Total</i>	100	100

6.3.4 Immobilization of lipase over magnetite nanoparticles

It is typically known that the stability and activity of enzymes are generally enhanced with appropriate immobilization strategies. In this work, we employed magnetite as the support that facilitates easy magnetic recoverability and reusability. Initially, the magnetite support was derivatized with amine functional groups using APTES, which gets anchored over the magnetite surface through Fe–O–Si linkage while leaving the amine groups available for further immobilization. Excess glutaraldehyde, which has an aldehyde group at both ends, was added to the amine-functionalized magnetite to enable the Schiff's base reaction to occur at one end of the chain. In the subsequent step, lipase was added to the aldehyde derivatized magnetite to facilitate its covalent immobilization *via* the imine bonds formed by the reaction between amine groups of lipase and free aldehyde groups available at the surface of the support. The reaction steps and the finally obtained Fe₃O₄@lipase were characterized using X-ray photoelectron spectroscopy (XPS) and field-emission scanning electron microscopy (FE-SEM).

Figure 6.4 (i & ii) show the XPS spectra of magnetite nanoparticles before and after subjecting to the surface derivatization steps. While the adventitious C *1s* peak was observed at 284.5 eV, the characteristic O *1s*, Fe *2p*_{3/2} and Fe *2p*_{1/2} signals from magnetite nanoparticles were observed in the narrow scan XPS spectra at binding energy values of 529.9, 710.7 and 724.5 eV, respectively [177], [247]. After APTES functionalization, the core level N *1s* signal corresponding to the amino group could be distinguished at ~400.0 eV (ref. [188] and [248]) alongside the characteristic signals from Fe₃O₄. Besides, the O *1s* narrow scan showed additional features at slightly higher binding energy values, indicating the effective anchoring and crosslinking of alkoxy silane, resulting in the formation of Si–O–Si and Si–O–Fe bonds. Though the glutaraldehyde treatment did not result in any significant difference, a clear intensification of the N *1s* signal and the appearance of a new signal at 163.5 eV corresponding to the S *2p* level were observed after the immobilization of both NL and EL [249]. These results clearly showed the successful immobilization of the enzymes over glutaraldehyde-derivatized magnetite nanoparticles.

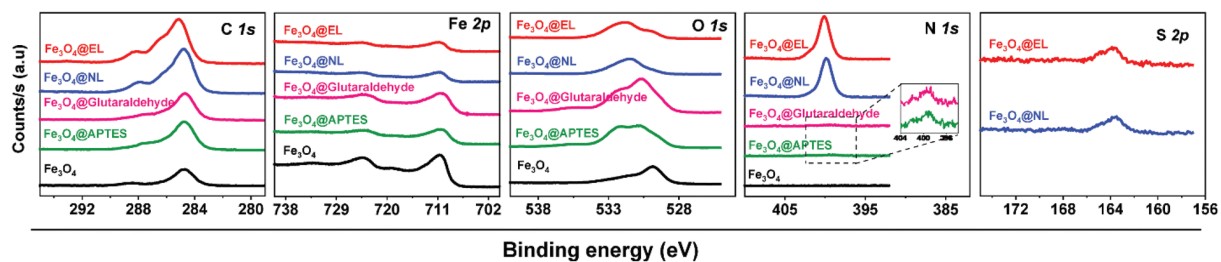


Figure 6.4 (i). C $1s$, Fe $2p$, O $1s$, N $1s$ and S $2p$ XPS narrow scan spectra of commercial Fe_3O_4 and its surface derivatized products such as APTES-functionalized ($\text{Fe}_3\text{O}_4@APTES$), glutaraldehyde-functionalized ($\text{Fe}_3\text{O}_4@glutaraldehyde$), $\text{Fe}_3\text{O}_4@NL$ and $\text{Fe}_3\text{O}_4@EL$. Selected regions of the N $1s$ narrow scan spectrum of $\text{Fe}_3\text{O}_4@APTES$ and $\text{Fe}_3\text{O}_4@glutaraldehyde$ are magnified and presented as an inset.

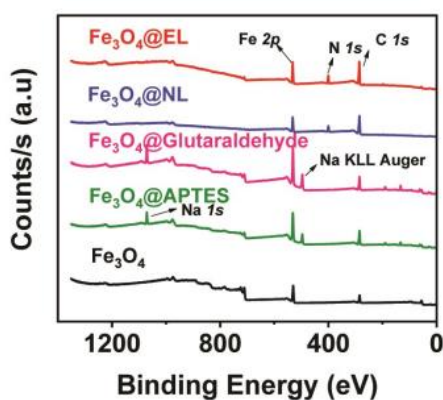


Figure 6.4 (ii). XPS survey scan spectra of commercial Fe_3O_4 , and its surface derivatized products.

FE-SEM imaging showed that the commercial magnetite particles were found to consist of cuboids in the size range of 150 to 300 nm (**Figure 6.5**). With the surface derivatization steps, the morphology and size of the particles were not altered significantly, suggesting that functionalization has taken place only at the very surface.

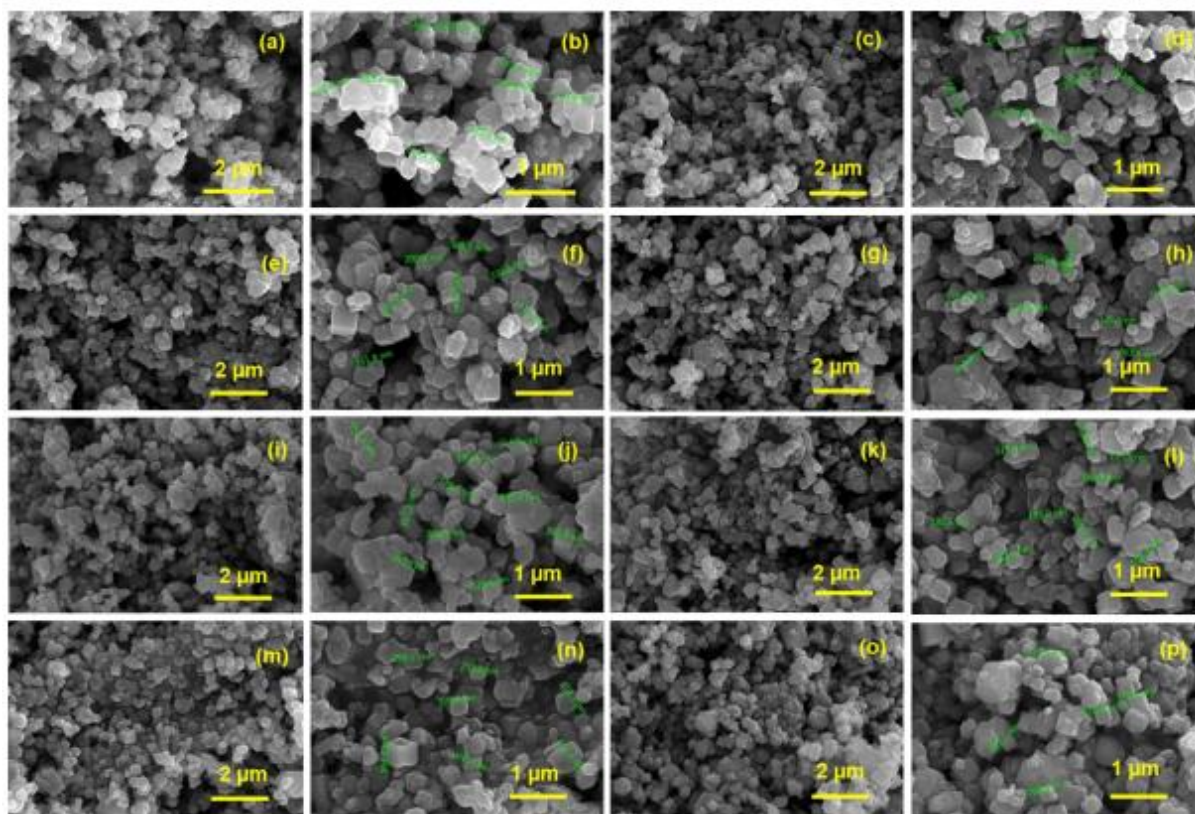


Figure 6.5 Composite FE-SEM images of commercial magnetite before functionalization (**a, b**), and after derivatization with APTES (**c, d**), glutaraldehyde (**e, f**) NL immobilization (**g, h**), and EL immobilization (**i, j**). The set of two different magnification images shown in (**k, l**), (**m, n**), and (**o, p**) correspond to $\text{Fe}_3\text{O}_4\text{@BSA}$, $\text{Fe}_3\text{O}_4\text{@BSA@NL}$, and $\text{Fe}_3\text{O}_4\text{@BSA@EL}$, respectively.

6.3.5 Lipase activity by the *p*-NP assay

Before proceeding with the biodiesel production, the obtained free- and immobilized lipases were screened for their specific activities using the gold standard *p*-NP assay **Figure 6.6**. It was found that the maximum specific activity values of the free (not immobilized) NL and EL were $236.9 \pm 2.3 \text{ U mg}^{-1}$ and $363.7 \pm 7 \text{ U mg}^{-1}$, respectively, at 37°C and pH 8.0. The higher activity of the EL was thus in line with the CD spectral observations. In a similar line, the $\text{Fe}_3\text{O}_4\text{@lipase}$ samples of native and expressed enzymes exhibited specific activity values of $279.3 \pm 9.8 \text{ U mg}^{-1}$ and $396.6 \pm 4.4 \text{ U mg}^{-1}$, respectively. When the temperature was increased sequentially up to 75°C , the specific activity of free- and immobilized lipases gradually decreased yet retained ~ 55 to 65% of the highest activity. This observation has shown the moderate thermos tolerant property of the employed lipase. The effect of pH on the specific activity of lipase was

then studied by keeping the temperature constant at 37 °C but varying the pH in the range of 4 to 12. The results exhibited a Gaussian-type distribution of the activity with the maximum value obtained at pH 8.0. The free lipases were found to retain ~50–55% of the specific activity at extreme pH values compared to the optimal pH, while those after immobilization over magnetite were found to retain ~74% of the activity under extreme pH conditions. These results confirmed the beneficial role of the immobilization process. The higher specific activity of the lipase after immobilization could be due to the interfacial activation, which results in a better micro-aqueous environment of opening the α -helix lid to facilitate the accessibility of the active catalytic sites to the substrate. Furthermore, the interfacial activity could have played a positive role in avoiding agglomeration as a result of better dispersion of the enzyme over the support [250].

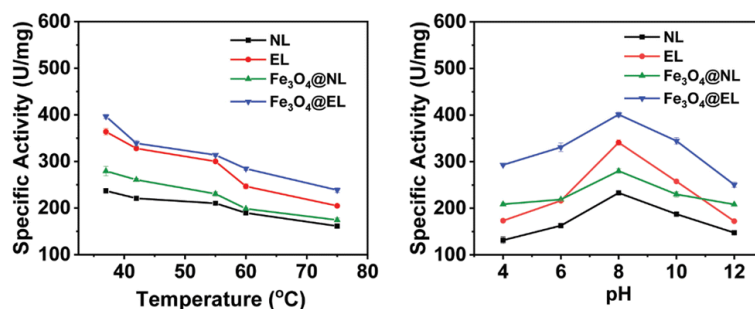


Figure 6.6 The specific activity analyses of the free and immobilized lipases using the *p*-NP assay depicting the effects of (a) temperature, and (b) pH.

6.3.6 Biodiesel production through transesterification of RBO

The enzymatic production of biodiesel through transesterification of RBO was then performed using NL and EL both in free and immobilized forms. Various reaction parameters such as catalyst dosage, oil-to-methanol ratio, temperature, incubation time and stirring rate were sequentially studied to obtain the optimal conditions (**Table 6.2 and Figure 6.7**). When the enzyme loading was varied from 25 to 400 μ g by doubling the catalyst concentration, a clear trend of increasing the biodiesel yield was observed. At a fixed loading of lipase, the biodiesel production efficacy followed the order of free NL < immobilized NL < free EL < immobilized EL. The yields of biodiesel obtained with 25, 50, 100, 200 and 400 μ g of immobilized EL were found to be 59.3, 69.8, 80.6, 87.4 and 94.5%, respectively. For further

optimization studies, we proceeded with 100 μg of the enzyme since a higher loading showed modest yield enhancement. The oil-to-methanol ratio is considered to be one of the critical parameters since the optimal concentration of the reactant influences the direction and magnitude of the equilibrium reaction. Stoichiometrically, a minimum of 3 equivalents of methanol would be required for one equivalent of triglyceride. Though a higher concentration of methanol could enhance product formation, it could also be detrimental to lipase activity. Therefore, we studied the effect of the oil-to-methanol ratio by varying it from 1 : 3 to 1 : 9. In this case too, the trend in the activity between the free and immobilized lipases followed the same order as was found with the catalyst loading. Importantly, when the oil-to-methanol ratio was taken as 1 : 3, only about 31.1% of biodiesel yield was obtained with the immobilized EL. However, the yield was significantly increased when the methanol content was increased further and attained a near-saturation value of $\sim 81\%$ when a ratio of 1 : 6 was employed, which therefore was used in further reactions.

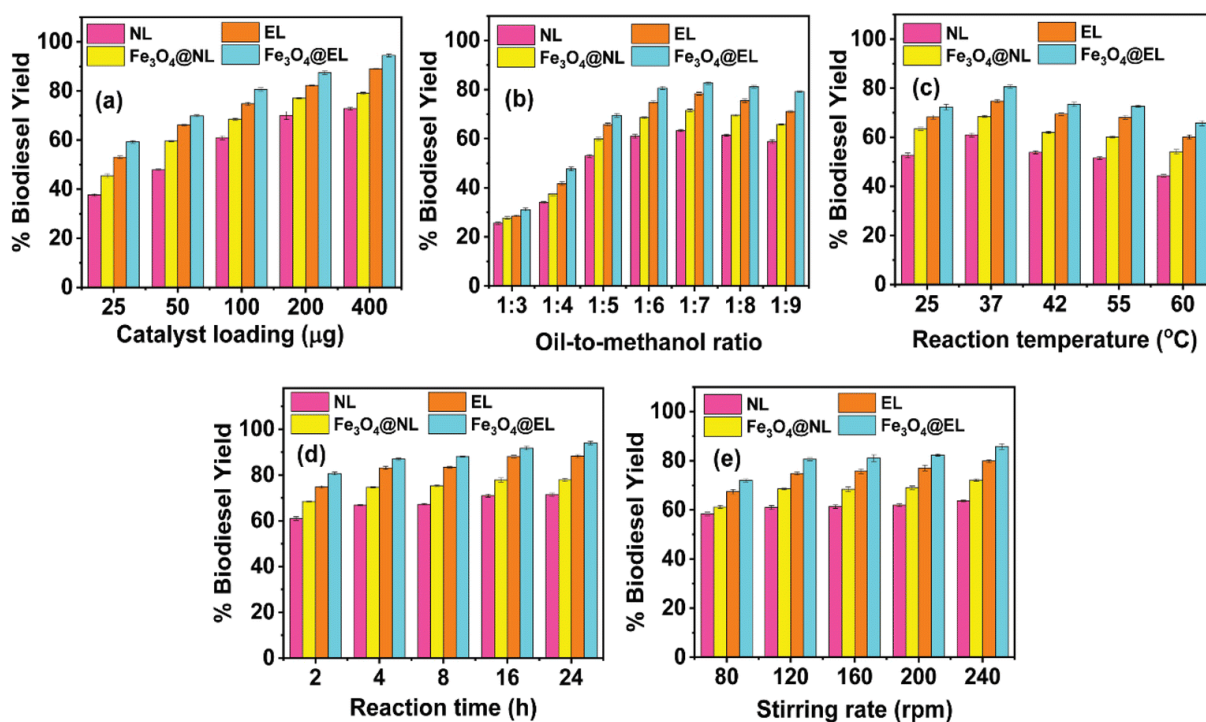


Figure 6.7 Optimization of reaction parameters, namely, catalyst loading (a), oil-to-methanol ratio (b), reaction temperature (c), incubation time (d) and stirring rate (e) for efficient biodiesel production with free and immobilized lipases.

The study on the effect of the reaction temperature revealed 37 °C as the optimal, while a significant biodiesel conversion (~72%) was observed even at 25 °C and 42–55 °C, indicating the stability of the enzyme in this temperature range. However, when the temperature was increased to 60 °C, the yield slightly decreased to 65.7%, which showed a similar trend to the *p*-NP assay. With respect to incubation time, a modest increment of ~3–4% yield was observed at every time interval, when the duration was varied as 2, 4, 8, 16 and 24 h. Thus, the yield reached a maximum of ~94% at 24 h. Pertaining to the stirring rate, the yield was increased from 72% to ~81% when the stirring rate was increased from 80 rpm to 120 rpm. With a further increase in the stirring rate, no significant enhancement in the biodiesel yield was observed. Based on these studies, 100 µg of catalyst, 1 : 6 oil to methanol ratio, 2 h incubation time, 37 °C reaction temperature and 120 rpm stirring rate were chosen as the optimal parameters for further studies. A comparative table for enzymatic biodiesel production using lipases from various sources is summarized in **Table 6.4**. It can be seen from the table that the probiotically-derived lipase employed in this work exhibited superior performance to several of the reported lipases, including the ones derived from fungi, when a combinatorial indicator of catalyst-to-oil ratio, reaction time and yield was considered.

Table 6.4 Salient parameters employed in the enzymatic biodiesel production using lipases from various sources

Catalyst	Substrate	Catalyst-to-oil ratio (wt %)	Reaction time (h)	Biodiesel yield (%)	Method	Reference
<i>Thermomyces lanuginosus</i> lipase	Canola oil	0.02	24	90	GC	[251]
<i>Thermomyces lanuginosus</i> lipase	Sunflower oil	1	24	97	GC	[252]
Lipozyme TL IM & Novozyme 435	Rapeseed oil	3 & 1	12	95	GC	[253]
<i>Pseudomanas cepacia</i> lipase	Jatropha oil	10	8	98	Gravimetry, GC	[254]
<i>Candida rugosa</i> lipase	Soybean oil	60	60	87	Hydroxyl content	[255]
Lipozyme TL IM	Palm oil	24.7	3	79.5	GC	[256]
TransZyme A	Sunflower oil	23	6	>95	¹ H NMR	[257]
<i>Thermomyces lanuginosus</i> lipase	Soybean oil	9	28	82.2	GC	[258]
Novozyme	Castor oil	5	3.8	94	HPLC	[259]

<i>Thermomyces lanuginosus</i> lipase	Soybean oil	0.7	8	97.1	GC	[260]
<i>Rhizopus stolonifera</i> & <i>Aspergillus tamarii</i> lipase	Mixed oil	10	48	92.3	GC	[261]
<i>Penicillium cyclopium</i> lipase	Soybean oil	20	20	60	GC	[262]
<i>Lactobacillus brevis</i> & <i>L. plantarum</i> lipase	Olive oil	5	2	67 to 81	Gravimetry	[234]
<i>Bacillus subtilis</i> lipase	Olive oil	2.62	1	45	Gravimetry	[240]
<i>Bacillus thermocatenulatus</i> lipase	Rapeseed oil	1.6	36	86	GC	[263]
<i>Bacillus licheniformis</i> lipase	Rice Bran oil	0.11	2	81	Gravimetry	This work
<i>Bacillus licheniformis</i> lipase	Rice Bran oil	0.44	2	94	Gravimetry	This work

6.3.7 Characterization of the biodiesel

The chemical structure of the obtained biodiesel against the RBO was studied using nuclear magnetic resonance (NMR) spectroscopy (**Figure 6.8** and **6.9**). The ^1H NMR of RBO exhibited several peaks corresponding to saturated alkyl protons in the range of 0.8 to 3 ppm. In addition, the presence of unsaturation was confirmed by the olefinic proton signals at 5.4 ppm, while the glycerol protons were observed at chemical shifts of 4.2–4.4 and 5.25 ppm. After enzymatic transesterification, the biodiesel obtained by NL and EL yielded identical NMR spectra [264], [265]. These spectra were found to show a new signal at 3.6 ppm, corresponding to methyl protons of the methyl ester. On the other hand, other protons corresponding to the saturated alkyl (0.8 to 3 ppm) and the olefinic protons (5.4 ppm) were found to be intact, whereas the glycerol protons majorly disappeared, which confirmed the clean reaction [266]. In the case of biodiesel obtained with the native lipase (NLB), a small amount of residual glycerol/glyceride was found in the final product. However, the biodiesel obtained with the expressed lipase (ELB) was found to be of higher purity. A small peak at 3.5 ppm was observed in both cases, which could be attributed to the methyl protons of methanol. The same was also found in minor quantities in the commercial RBO as well.

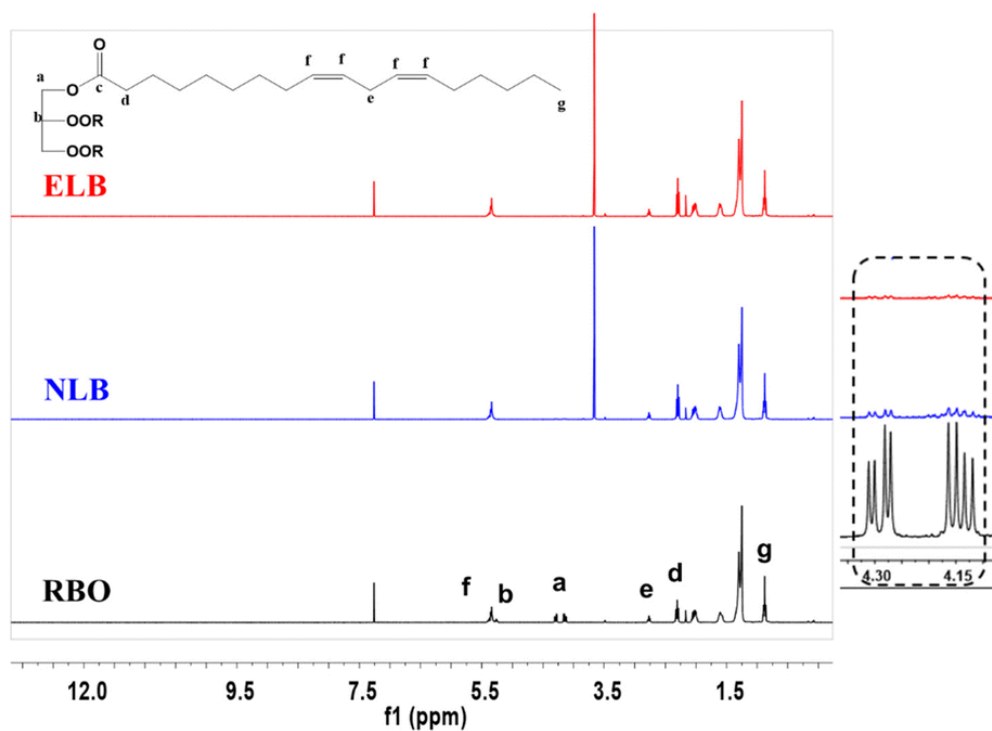


Figure 6.8 ^1H NMR spectra of RBO, NLB and ELB. Salient signals are assigned using linoleate as the representative compound.

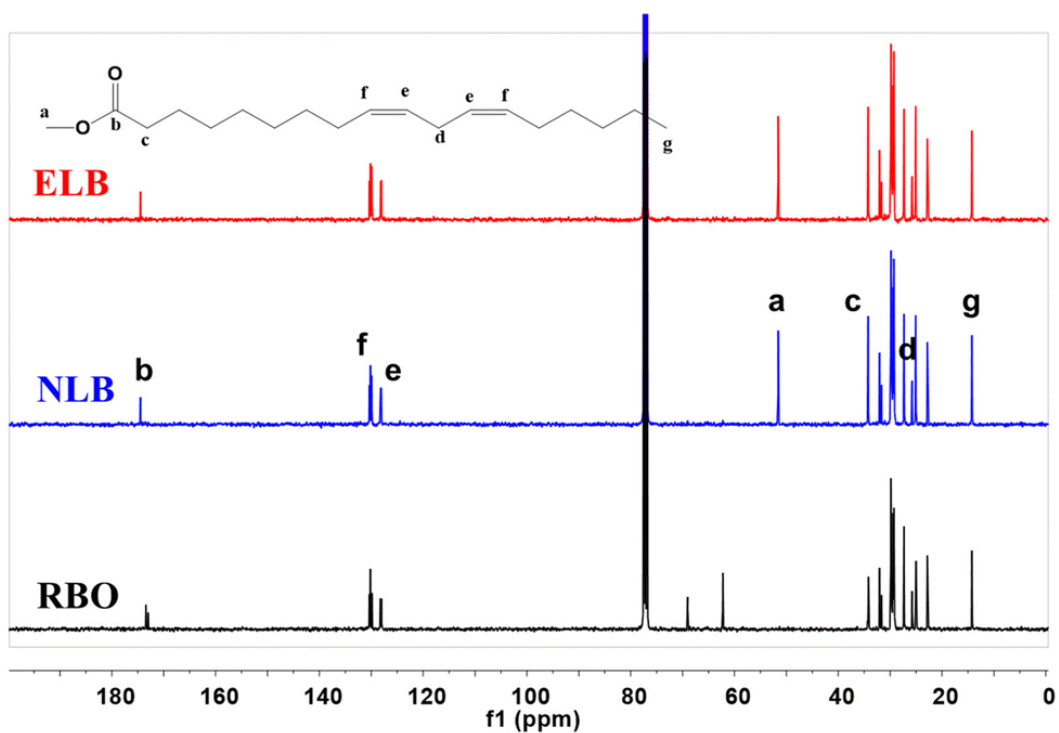


Figure 6.9 ^{13}C NMR spectra of RBO, NLB and ELB. Salient signals are assigned using linoleate as the representative compound.

^{13}C NMR analyses were additionally performed (**Figure 6.9**) to corroborate the observations from ^1H NMR. The spectrum of RBO exhibited characteristic carbonyl, olefinic, ester (of glycerol moiety) and alkyl carbons at the chemical shift values of 173–173.5, 128–131, 62–69 and 14–32 ppm, respectively. It is noteworthy that two signals corresponding to carbonyl carbons were observed in RBO due to the primary and secondary adjacent carbons of the glycerol moiety. On the other hand, in NLB and ELB samples, only a single signal of carbonyl carbon at a slight downfield of 174 ppm was observed, indicating methyl ester formation, which was additionally confirmed by the appearance of a new signal of methyl carbon at 52 ppm. Furthermore, the absence of carbon peaks at 62 and 69 ppm – originating from the glycerol moiety – reiterated the observations from ^1H NMR on the formation of the biodiesel.

The ester content in fatty acid methyl esters (FAME) was determined by Gas chromatography (GC) using a test method EN 14103 2020. The internal standard (IS) of biodiesel include is methyl heptadecanoate (MHD). The biodiesel obtained using both lipases showed nearly identical GC profiles with a similar composition. Three major eluent signals observed at 20.2, 26.6 and 27.9 min retention values were assigned to methyl palmitate, methyl oleate and methyl linoleate, respectively (**Figure 6.10**). A small peak observed at 26.1 min was attributed to methyl stearate. Minute portions of other methyl esters like methyl arachidate (retention time: 29.7) and methyl linolenate (retention time: 32.8) were also observed to the tune of less than 0.7%. The proportions of the palmitate, stearate, oleate and linoleate were quantified to be 19.8%, 1.9%, 45.1% and 32.5%, respectively, which are in line with the literature reports [267]. Since these studies revealed a near similar biodiesel composition with a slight glyceride impurity in NLB (as indicated by ^1H NMR), further FAME studies were performed using ELB.

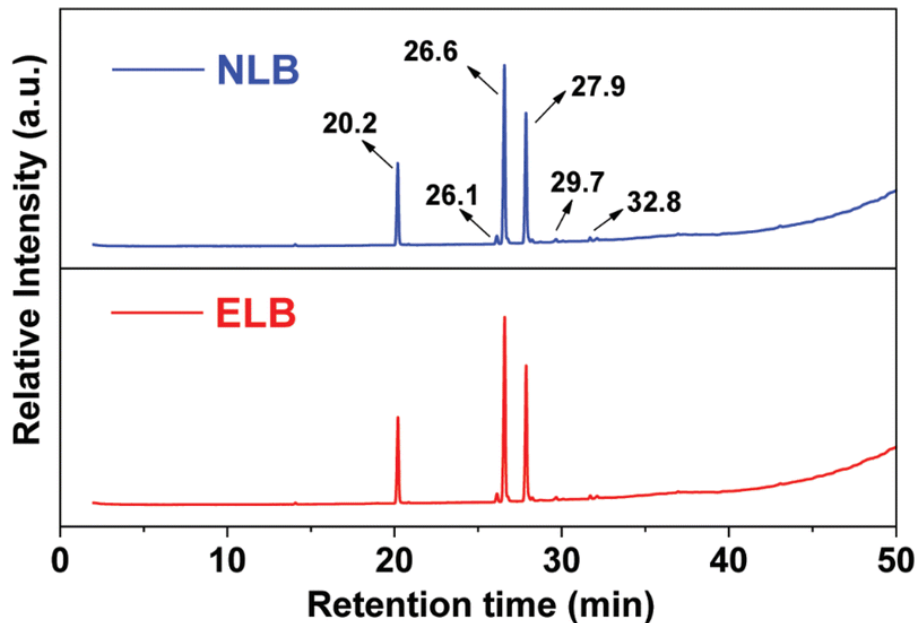


Figure 6.10 GC profiles of NLB and ELB

Thermogravimetric analysis (TGA) of RBO was compared with ELB in order to derive insights into the decomposition profile as a function of temperature (Figure 6.11 (a)). Considering 5 wt% mass loss as the onset of thermal decomposition of the substance, RBO was found to exhibit a decomposition temperature of 356 °C and the process followed a single step decomposition profile that was completed by 470 °C. On the other hand, the onset of thermal decomposition of ELB was found to be 182 °C, which is nearly half the value of RBO. In this case, a two-step decomposition pattern was observed, in which 91% of mass loss was observed by 255 °C in the first step and the residual portion was wholly decomposed by ~405 °C [268].

Rheological studies were performed to find the viscoelastic properties of RBO and ELB and the results are shown in Figure 6.11 (b) and (c). Initially, the absolute viscosity was measured as a function of shear rate at two different temperatures of 25 °C and 40 °C [269]. At 25 °C, RBO exhibited an increasing trend in viscosity in the shear rate range of 5–50 s⁻¹, above which a constant value of ~67 mPa s was reached. At 40 °C, the viscosity was found to be ~36.3 mPa s at a shear rate of 5 s⁻¹, which remained constant up to 300 s⁻¹. In the case of ELB, at both temperatures, the viscosity values were found to be stable in the measured shear rate range. At 25 °C, the viscosity of ELB was found to be ~7 mPa s, whereas the value was found to be ~5.3 mPa s at 40 °C, which showed a substantial decrease in comparison with RBO. The shear

stress *versus* shear rate studies revealed the Newtonian behavior of both RBO and ELB at both temperatures, as signified by a linear increase in shear stress with an increase in shear rate. It is worth noting that the shear stress exhibited by ELB was significantly lower than that of RBO. Other physicochemical properties such as FAME content and density of the ELB were determined to be >99% and 0.86 g cm^{-3} , respectively.

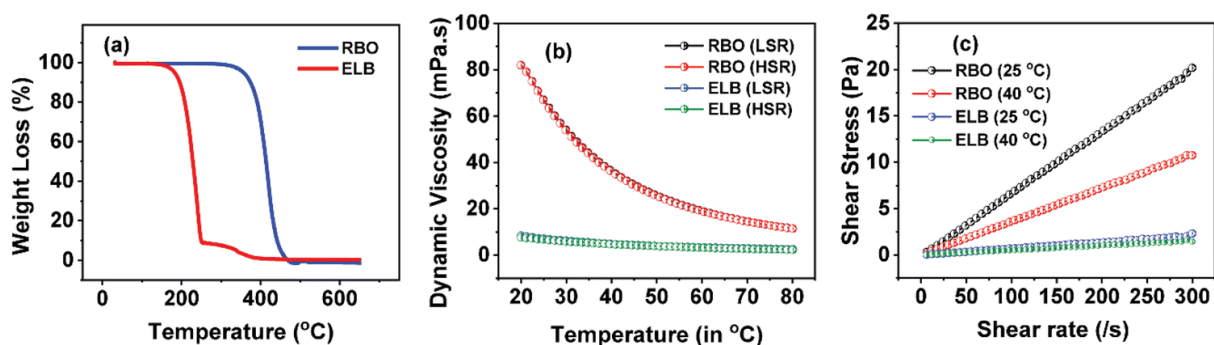


Figure 6.11 TGA (a) and rheological behavior (b and c) of ELB in comparison with RBO. The LSR and HSR in (b) represent the low shear rate (50 s^{-1}) and high shear rate (300 s^{-1}), respectively.

6.3.8 Recyclability studies

The facile recyclability of the catalyst is an important parameter both in terms of environmental concern and economic viability. A recent report showed that BSA was beneficial for preserving the activity of the enzymes when co-immobilized [270]. It has been postulated that BSA is a major component in serum and therefore can act as a universal stabilizer for a variety of proteins. BSA was proven to present a protein-friendly neighborhood to provide stability and high-retention of enzyme activity. Therefore, we employed two more immobilization strategies of lipase over magnetite to find out the best possible approach. In one case, BSA was wrapped over Fe_3O_4 @lipase to yield Fe_3O_4 @lipase@BSA, whereas in the other case, BSA at first was immobilized over Fe_3O_4 to yield Fe_3O_4 @BSA, over which lipase was then immobilized to obtain Fe_3O_4 @BSA@lipase. The recyclability studies with both NL and EL subjected to three different immobilization strategies towards biodiesel production up to 8 cycles *via* magnetic recovery were performed and the results are compared in **Figure 6.12 (a)**. As expected, EL exhibited higher activity and stability at every cycle, when compared to the native one. Among the different immobilization strategies, the ones with BSA co-immobilization were superior to those without BSA and almost comparable until five cycles, above which Fe_3O_4 @BSA@lipase

exhibited better retention of the activity than Fe₃O₄@lipase@BSA. We speculate that the optimal orientation of lipase in between the void pockets provided by BSA could have resulted in > 50 % retention of relative activity with Fe₃O₄@BSA@lipase even at the eighth cycle.

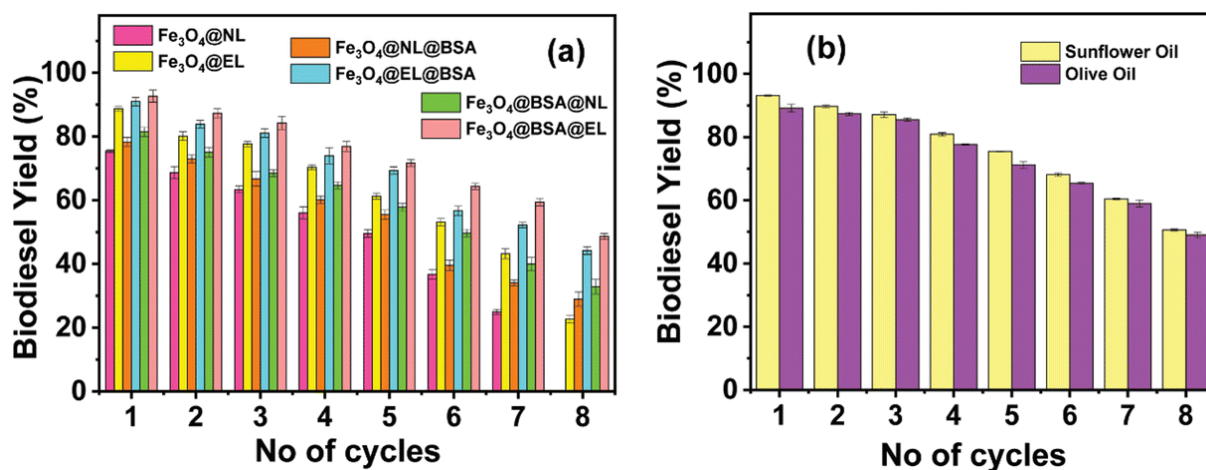


Figure 6.12 (a) Recyclability studies up to 8 cycles using both NL and EL anchored over magnetite using three different immobilization approaches with RBO. (b) Comparative biodiesel production with sunflower and olive oils using the optimal Fe₃O₄@BSA@EL catalyst up to 8 cycles.

The XPS analyses of the recovered catalysts showed sulfur contents nearly comparable to those of fresh ones, which signified the presence of immobilized proteins even after 8 cycles (**Figure 6.13 a & b**). This has been confirmed through Bradford's assay with the supernatant solution, which revealed no significant protein leaching. Therefore, the loss of activity over successive cycles could be attributed to the gradual deactivation of the enzyme or any aggregation among the magnetite nanoparticles. It can be noted that the spent catalyst after each cycle was captured using a magnet underneath the reaction vessel, washed with methanol and then re-suspended through vortexing after adding fresh oil to it. This could have caused a certain degree of aggregation among the magnetite nanoparticles, which in turn could have resulted in the gradual loss of activity. Thus, there exists further room to improve the stability during cyclability experiments by minimizing particle aggregation or selecting suitable hydrophobic surfaces for immobilization to regain the activity [239]. To probe the wide-range scope of the optimal catalyst composition for other vegetable oils, biodiesel production in a recyclable manner was performed using sunflower and olive oils as well (**Figure 6.12 b**). The

biodiesel production and recyclability performance with these two oils were found to be quite similar to that of RBO. These results additionally confirmed the high potential of the enzyme catalytic system presented herein for biodiesel production from various oil sources.

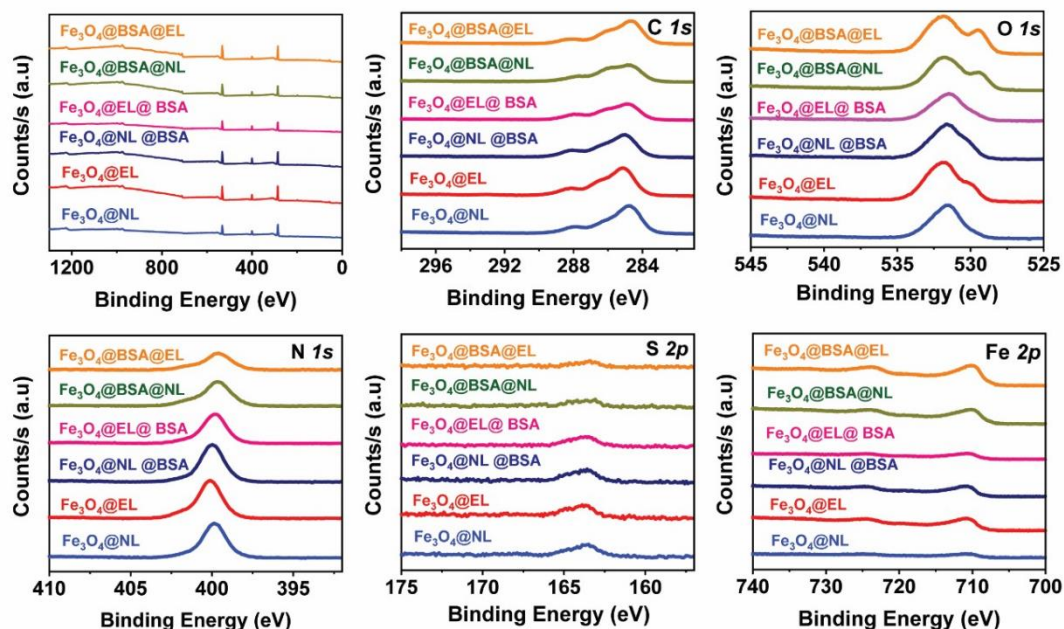


Figure 6.13 (a). XPS survey scan (top left panel) and narrow scan (elements quoted in the respective panels) spectra of the fresh catalysts before subjecting to the recyclability experiments.

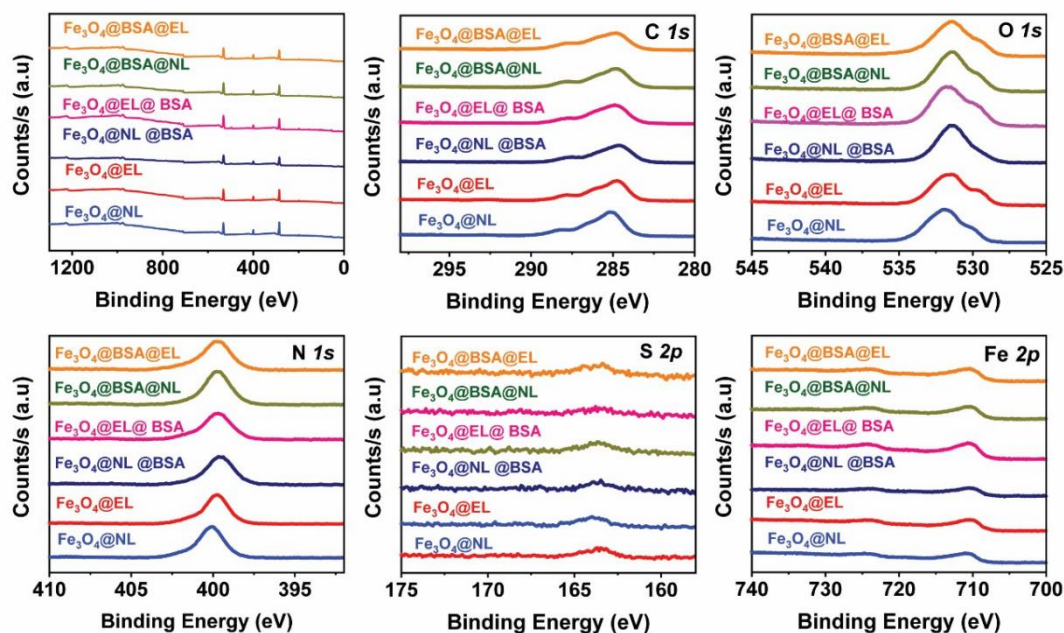


Figure 6.13 (b). XPS survey scan (top left panel) and narrow scan (elements quoted in the respective panels) spectra of the spent catalysts recovered after eighth cycles.

6.4 Conclusions

Native and expressed lipases from a probiotic source, *B. licheniformis*, were produced and characterized using Bradford assay, SDS-PAGE and CD studies. The benchmark *p*-NP assay revealed higher activity of EL than the native enzyme. The lipases were then immobilized over magnetite support to yield Fe₃O₄@lipase, which was characterized using XPS and FE-SEM techniques. The prepared catalysts were studied for their efficacy towards biodiesel production from RBO, which revealed the optimal catalyst loading, oil-to-methanol ratio, stirring rate, temperature and time as 100 µg, 1:6, 120 rpm, 37 °C and 2 h, respectively. Under optimal reaction conditions, the yield was found to be ~81% in 2 h of incubation time, which increased to ~94 % either by increasing the catalyst loading to 400 µg or extending the reaction time to 24 h. NMR, GC and FAME content analyses revealed > 99 % purity of the biodiesel, while other physicochemical properties like density and viscosity were ascertained to be well within the acceptable range. Among the three immobilization approaches employed in this work, Fe₃O₄@BSA@lipase exhibited retention of ~50 % relative activity at the eighth cycle. The optimized biocatalyst developed in this study by far has shown superior activity in terms of the combinatorial factors of catalyst-to-oil and reaction time. Besides, contrary to popular opinion, the work has also shown higher performance of the lipase derived from a probiotic source than the one obtained from fungal sources. The remarkable activity of the reported biocatalyst can further be enhanced by combining it with strategies like employing ionic liquids, continuous reactor setup *etc* [257], [271], [272]. The present study has thus shown biodiesel production in an eco-friendly and benign-by-design fashion.

Chapter 7

Summary and Conclusions

7.1 Summary

Surface functionalization of polymers and nanoparticles opens avenues in the field of biotechnology. The new functional properties of as-derived materials have huge applications. Hence, the present study aims to derive new functions to the biomaterial and explore the potential for different applications. Based on the gaps available from the existing literature, the objectives of the present work can thus be broadly divided into the following aspects:

- Probiotic lipase-mediated silver derivatization over biopolymer towards antimicrobial coatings.
- Enhancing the sensitivity of ratiometric genosensing using plasmonic gold nanoparticles.
- Fluorescence-based simultaneous dual oligo-sensing of genotypes using magnetite nanoparticles.
- Boronic acid chemistry for fluorescence-based quantitative DNA/RNA sensing.
- Efficient biodiesel production from cooking oils using magnetite immobilized-recombinant lipase from probiotic bacteria.

7.2 Conclusions

In conclusion the following observations are made about the results obtained in this study.

Probiotic lipase-mediated silver derivatization over biopolymer towards antimicrobial coatings:

Towards this objective, we primarily employed a probiotically derived lipase from *Lactobacillus amylovorus* to derivatize the PCL film surface with silver. Two facile surface derivatization approaches were developed, (i) lipase-capped Ag NPs' immobilization over EDC/NHS-activated PCL films and (ii) dip-coating over lipase-immobilized PCL films. The success of surface derivatization was chemically probed using XPS and morphologically examined using FE-SEM. The antimicrobial studies revealed that the PCL films immobilized with the probiotically derived lipase-capped Ag NPs exhibited remarkable bactericidal efficacy as opposed to the samples obtained through the dip-coating method. The cytotoxicity studies using mouse fibroblast SNL 76/7 cells revealed the high cell compatibility of PCL films immobilized with the lipase-capped Ag NPs.

Enhancing the sensitivity of ratiometric genosensing using plasmonic gold nanoparticles:

To improve the hybridization between an ASO and target DNA, we employed a flash heating of oligos at 95 °C for 120 s before the hybridization at 65 °C for 20 min. From the PAGE analysis, a 7.5% increase in the hybridization than without flash heating. The effect was further analyzed in the Au NPs based DNA sensing to ascertain the usefulness of flash heating in practical applications. The DNA sensing studies using thiol-tagged synthetic oligonucleotide, derived from the core region of the HCV viral genome revealed that the ASO-target DNA

hybrid subjected to the flash heating stabilized the Au NPs more than the case without flash heating, as evidenced by the lesser ratiometric absorbance values for the former. Furthermore, the use of citrate buffer has shown to be beneficial in the efficient conjugation between the thiolated probe and the Au NPs, even when the DNA to Au NPs ratio is as low as 3.5:1 and 7:1. These results may find potential in employing the appropriate hybridization conditions in the DNA bio-sensing studies.

Fluorescence-based simultaneous dual oligo-sensing of genotypes using magnetite nanoparticles:

Magnetite NPs-mediated fluorescence-based simultaneous dual oligo sensing was demonstrated by selecting two target sequences from HCV genotypes 1 and 3. To achieve this, the magnetite NPs were initially derivatized with APTES, followed by the glutaraldehyde linker. Two amine-tagged probes corresponding to the genotypes 1 and 3 were individually immobilized over the magnetite nanoparticles through imine bond formation in high efficiency by reacting with aldehyde groups, which was characterized using XPS and EDS analyses. Two approaches, such as one-step and two-step hybridization methods, were explored to understand the efficacy of the sensing assays. Among these, the two-step hybridization method, where the fluorescently-tagged probe-2 and target were subjected to hybridization in a first step followed by hybridization with the probe-1 immobilized over magnetite NPs in a subsequent step, was found to be more efficient. The fluorescence intensity analysis after the magnetic removal of the NPs enabled the quantitative sensing of the targets with a LOD of <15 nM. This strategy

can potentially be extrapolated to multiplex sensing of various pathogens in a single go by immobilizing as many probes over the magnetite NPs.

Boronic acid chemistry for fluorescence-based quantitative DNA/RNA sensing:

First, in typical fluorescence-based DNA detection approaches, it is a prerequisite to tag the fluorophore to the oligos, tagging the fluorophore over multiple probes or targets would substantially increase the cost. The current study reveals the possibility of fluorescently tagging the oligos after the hybridization step in a rapid and facile manner. Second, due to the reversible binding nature of the used tag, boronic acid, the oligonucleotides can be recovered by cleaving the fluorophore at acidic pH. Third, the possibility of detecting the cDNA and cRNA with a single probe DNA is established in a concentration-dependent manner. The present proof-of-concept study opens up several new opportunities for further exploration in this domain. Several strategies such as photo electrochemical, electro-generated chemiluminescence, hybridization chain reaction, etc., can explore the suitability of the boronic acid chemistry for DNA/RNA sensing to enhance the sensitivity to picomolar to femtomolar (pM-fM) range.

Efficient biodiesel production from cooking oils using magnetite immobilized-recombinant lipase from probiotic bacteria:

The lipases from a probiotic bacteria (*B. licheniformis*) were then immobilized over magnetite support to yield Fe₃O₄@lipase, characterized using XPS and FE-SEM techniques. The prepared catalysts were studied for their efficacy towards biodiesel production from RBO, which revealed the optimal catalyst loading, oil-to-methanol ratio, stirring rate, temperature,

and time as 100 µg, 1:6, 120 rpm, 37 °C and 2 h, respectively. Under optimal reaction conditions, the yield was found to be ~81% in 2 h of incubation time, which increased to ~94 % either by increasing the catalyst loading to 400 µg or extending the reaction time to 24 h. NMR, GC, and FAME content analyses revealed > 99 % purity of the biodiesel, while other physicochemical properties like density and viscosity were ascertained to be within the acceptable range. By employing BSA in the derivatization process ($\text{Fe}_3\text{O}_4@\text{BSA}@lipase$) ~50 % relative activity retention was achieved at the eighth cycle. The optimized biocatalyst developed in this study has shown superior activity in terms of the combinatorial factors of catalyst-to-oil and reaction time. Besides, contrary to popular opinion, the work has also shown the higher performance of the lipase derived from a probiotic source than the one obtained from fungal sources. The remarkable activity of the reported biocatalyst can further be enhanced by combining it with strategies like employing ionic liquids, continuous reactor setup, *etc.* The present study has thus shown biodiesel production in an eco-friendly and benign-by-design fashion.

7.3 Major contributions of the work

The following are the major contributions from the above work.

- PCL films immobilized with the probiotically derived lipase-capped Ag NPs exhibited remarkable bactericidal efficacy, high cell compatibility.
- The ASO-target DNA hybrid, designed for HCV detection, when subjected to the flash heating stabilized the Au NPs more than the case without flash heating, as a result increasing the sensitivity of ratio metric sensing. The use of citrate buffer has shown to

be beneficial in the efficient conjugation between the thiolated probe and the Au NPs even at low concentrations

- We demonstrate a facile fluorescence-based simultaneous dual oligo sensing of genotypes 1 and 3 by employing two target sequences (36-mers each) derived from the NS4B and NS5A regions of HCV genome, with the detection limit in the range of 10–15 nM.
- “Boronic acid chemistry for fluorescence-based quantitative DNA/RNA sensing” has successfully shown the feasibility to quantitatively detect DNA and RNA in the concentration range of 5 to 50 nM.
- Native and expressed lipases from *B. licheniformis* with higher activity was achieved. Magnetite-immobilized lipases showed high efficacy in biodiesel conversion (~81%) even at a minimal enzyme loading of 0.11 wt% with respect to the oil in 2 h of duration. The nuclear magnetic resonance, gas chromatography and FAME analysis revealed >99% purity of biodiesel. BSA mediated immobilization of lipases over magnetite, retained >50% relative activity even at the eighth cycle.

7.4 Future scope of the work

The future possibilities arising from the results of the present work are as given below:

- Our study on the PCL films derivatized with biogenically synthesized Ag NPs could potentially serve as infection-free implantable materials with high bio-compatibility.

- By employing flash heating in efficient hybridization, and the use of citrate buffer for rapid and effective thiol tagging over the Au NPs is proven to be advantageous in enhancing the sensitivity of ratio metric genosensing.
- “Fluorescence-based simultaneous dual oligo sensing using magnetite nanoparticles”, strategy towards multiplex detection of analytes in a single assay would lead to high throughput analysis, substantial benefits in terms of time, infrastructure, labor, and cost.
- “Boronic acid chemistry for fluorescence-based quantitative DNA sensing” is proof-of-concept study opens up several new opportunities for further exploration in this domain. First, thorough mechanistic details of the interaction through additional experimental, computational and theoretical works are required. Second, the detailed probing on the dependence of the immobilized probe’s packing density and its effect on the boronic acid binding response can be studied. Third, several strategies such as photo electrochemical, electrogenerated chemiluminescence, hybridization chain reaction, etc., can explore the suitability of the boronic acid chemistry for DNA sensing to enhance the sensitivity to pM-fM range with a potential of multiplexing.
- Our strategy employing “magnetite immobilized-recombinant lipase from probiotic *Bacillus licheniformis*”, opens up numerous possibilities in amalgamating various benign biotechnological approaches with enzymes derived from probiotic sources for diverse applications.

References

- [1] P. Chaudhary, F. Fatima, and A. Kumar, "Relevance of Nanomaterials in Food Packaging and its Advanced Future Prospects," *J. Inorg. Organomet. Polym. Mater.*, vol. 30, no. 12, pp. 5180–5192, 2020, doi: 10.1007/s10904-020-01674-8.
- [2] G. Sanità, B. Carrese, and A. Lamberti, "Nanoparticle Surface Functionalization: How to Improve Biocompatibility and Cellular Internalization," *Frontiers in Molecular Biosciences*, vol. 7, 2020. [Online]. Available: <https://www.frontiersin.org/articles/10.3389/fmolb.2020.587012>
- [3] H. Heinz *et al.*, "Nanoparticle decoration with surfactants: Molecular interactions, assembly, and applications," *Surf. Sci. Rep.*, vol. 72, no. 1, pp. 1–58, 2017, doi: <https://doi.org/10.1016/j.surfrep.2017.02.001>.
- [4] M. H. Jazayeri, H. Amani, A. A. Pourfatollah, H. Pazoki-Toroudi, and B. Sedighimoghaddam, "Various methods of gold nanoparticles (GNPs) conjugation to antibodies," *Sens. Bio-Sensing Res.*, vol. 9, pp. 17–22, 2016, doi: <https://doi.org/10.1016/j.sbsr.2016.04.002>.
- [5] J. Balcucho, D. M. Narváez, and J. L. Castro-Mayorga, "Antimicrobial and Biocompatible Polycaprolactone and Copper Oxide Nanoparticle Wound Dressings against Methicillin-Resistant Staphylococcus aureus," *Nanomaterials*, vol. 10, no. 9, 2020. doi: 10.3390/nano10091692.
- [6] A. K. Pearce and R. K. O'Reilly, "Polymers for Biomedical Applications: The Importance of Hydrophobicity in Directing Biological Interactions and Application Efficacy," *Biomacromolecules*, vol. 22, no. 11, pp. 4459–4469, Nov. 2021, doi: 10.1021/acs.biomac.1c00434.
- [7] Z. Zhang *et al.*, "Synthesis and antibacterial activity of polymer–antibiotic conjugates incorporated into a resin-based dental adhesive," *Biomater. Sci.*, vol. 9, no. 6, pp. 2043–2052, 2021, doi: 10.1039/D0BM01910K.
- [8] R. P. Babu, K. O'Connor, and R. Seeram, "Current progress on bio-based polymers and their future trends," *Prog. Biomater.*, vol. 2, no. 1, p. 8, 2013, doi: 10.1186/2194-0517-

- 2-8.
- [9] G. Picardi, F. J. Colas, R. Gillibert, and M. L. de la Chapelle, “Spectral Shift of the Plasmon Resonance Between the Optical Extinction and Absorption of Gold and Aluminum Nanodisks,” *J. Phys. Chem. C*, vol. 120, no. 45, pp. 26025–26033, Nov. 2016, doi: 10.1021/acs.jpcc.6b09000.
- [10] S. A. Nepijko, H. J. Elmers, and G. Schönhense, “Emission Properties of Metal Nanoparticles BT - Handbook of Nanoparticles,” M. Aliofkhazraei, Ed. Cham: Springer International Publishing, 2016, pp. 521–547. doi: 10.1007/978-3-319-15338-4_25.
- [11] G. V Hartland, L. V Besteiro, P. Johns, and A. O. Govorov, “What’s so Hot about Electrons in Metal Nanoparticles?,” *ACS Energy Lett.*, vol. 2, no. 7, pp. 1641–1653, Jul. 2017, doi: 10.1021/acsenerylett.7b00333.
- [12] B. Sutens *et al.*, “Tunability of Size and Magnetic Moment of Iron Oxide Nanoparticles Synthesized by Forced Hydrolysis,” *Materials*, vol. 9, no. 7. 2016. doi: 10.3390/ma9070554.
- [13] I. Khan, K. Saeed, and I. Khan, “Nanoparticles: Properties, applications and toxicities,” *Arab. J. Chem.*, vol. 12, no. 7, pp. 908–931, 2019, doi: <https://doi.org/10.1016/j.arabjc.2017.05.011>.
- [14] Y. N. Slavin, J. Asnis, U. O. Häfeli, and H. Bach, “Metal nanoparticles: understanding the mechanisms behind antibacterial activity,” *J. Nanobiotechnology*, vol. 15, no. 1, p. 65, 2017, doi: 10.1186/s12951-017-0308-z.
- [15] X. Hu, Y. Zhang, T. Ding, J. Liu, and H. Zhao, “Multifunctional Gold Nanoparticles: A Novel Nanomaterial for Various Medical Applications and Biological Activities ,” *Frontiers in Bioengineering and Biotechnology* , vol. 8. 2020. [Online]. Available: <https://www.frontiersin.org/articles/10.3389/fbioe.2020.00990>
- [16] A. Ali *et al.*, “Review on Recent Progress in Magnetic Nanoparticles: Synthesis, Characterization, and Diverse Applications ,” *Frontiers in Chemistry* , vol. 9. 2021. [Online]. Available: <https://www.frontiersin.org/articles/10.3389/fchem.2021.629054>
- [17] J. Kudr *et al.*, “Magnetic Nanoparticles: From Design and Synthesis to Real World Applications,” *Nanomaterials*, vol. 7, no. 9. 2017. doi: 10.3390/nano7090243.
- [18] K. S. Khoo, W. Y. Chia, D. Y. Tang, P. L. Show, K. W. Chew, and W.-H. Chen,

- “Nanomaterials Utilization in Biomass for Biofuel and Bioenergy Production,” *Energies*, vol. 13, no. 4. 2020. doi: 10.3390/en13040892.
- [19] D. Goldberg, “A review of the biodegradability and utility of poly(caprolactone),” *J. Environ. Polym. Degrad.*, vol. 3, no. 2, pp. 61–67, 1995, doi: 10.1007/BF02067481.
- [20] F. Ahmad *et al.*, “Unique Properties of Surface-Functionalized Nanoparticles for Bio-Application: Functionalization Mechanisms and Importance in Application,” *Nanomaterials*, vol. 12, no. 8. 2022. doi: 10.3390/nano12081333.
- [21] L. Guerrini, R. A. Alvarez-Puebla, and N. Pazos-Perez, “Surface Modifications of Nanoparticles for Stability in Biological Fluids.,” *Mater. (Basel, Switzerland)*, vol. 11, no. 7, Jul. 2018, doi: 10.3390/ma11071154.
- [22] P. Sengupta and B. L. V Prasad, “Surface Modification of Polymers for Tissue Engineering Applications: Arginine Acts as a Sticky Protein Equivalent for Viable Cell Accommodation,” *ACS Omega*, vol. 3, no. 4, pp. 4242–4251, Apr. 2018, doi: 10.1021/acsomega.8b00215.
- [23] W. Sun, W. Liu, Z. Wu, and H. Chen, “Chemical Surface Modification of Polymeric Biomaterials for Biomedical Applications,” *Macromol. Rapid Commun.*, vol. 41, no. 8, p. 1900430, Apr. 2020, doi: <https://doi.org/10.1002/marc.201900430>.
- [24] C. Adlhart *et al.*, “Surface modifications for antimicrobial effects in the healthcare setting: a critical overview,” *J. Hosp. Infect.*, vol. 99, no. 3, pp. 239–249, 2018, doi: <https://doi.org/10.1016/j.jhin.2018.01.018>.
- [25] C. Y. Flores, A. G. Miñán, C. A. Grillo, R. C. Salvarezza, C. Vericat, and P. L. Schilardi, “Citrate-Capped Silver Nanoparticles Showing Good Bactericidal Effect against Both Planktonic and Sessile Bacteria and a Low Cytotoxicity to Osteoblastic Cells,” *ACS Appl. Mater. Interfaces*, vol. 5, no. 8, pp. 3149–3159, Apr. 2013, doi: 10.1021/am400044e.
- [26] M. J. Hajipour *et al.*, “Antibacterial properties of nanoparticles,” *Trends Biotechnol.*, vol. 30, no. 10, pp. 499–511, 2012, doi: <https://doi.org/10.1016/j.tibtech.2012.06.004>.
- [27] G. Franci *et al.*, “Silver Nanoparticles as Potential Antibacterial Agents,” *Molecules*, vol. 20, no. 5. pp. 8856–8874, 2015. doi: 10.3390/molecules20058856.
- [28] S. Jaiswal, K. Bhattacharya, P. McHale, and B. Duffy, “Dual effects of β -cyclodextrin-

- stabilised silver nanoparticles: enhanced biofilm inhibition and reduced cytotoxicity,” *J. Mater. Sci. Mater. Med.*, vol. 26, no. 1, p. 52, 2015, doi: 10.1007/s10856-014-5367-1.
- [29] S. Zhang, Y. Tang, and B. Vlahovic, “A Review on Preparation and Applications of Silver-Containing Nanofibers,” *Nanoscale Res. Lett.*, vol. 11, no. 1, p. 80, 2016, doi: 10.1186/s11671-016-1286-z.
- [30] M. Guilger-Casagrande *et al.*, “Influence of the capping of biogenic silver nanoparticles on their toxicity and mechanism of action towards *Sclerotinia sclerotiorum*,” *J. Nanobiotechnology*, vol. 19, no. 1, p. 53, 2021, doi: 10.1186/s12951-021-00797-5.
- [31] A. Banerjee, K. Chatterjee, and G. Madras, “Enzymatic degradation of polymers: a brief review,” *Mater. Sci. Technol.*, vol. 30, no. 5, pp. 567–573, May 2014, doi: 10.1179/1743284713Y.0000000503.
- [32] P. A. Maraju, P. Tata, A. Balapure, J. Ray Dutta, and R. Ganesan, “*Lactobacillus amylovorus* derived lipase-mediated silver derivatization over poly(ϵ -caprolactone) towards antimicrobial coatings,” *Enzyme Microb. Technol.*, vol. 150, p. 109888, 2021, doi: <https://doi.org/10.1016/j.enzmictec.2021.109888>.
- [33] P. N. Manoudis and I. Karapanagiotis, “Modification of the wettability of polymer surfaces using nanoparticles,” *Prog. Org. Coatings*, vol. 77, no. 2, pp. 331–338, 2014, doi: <https://doi.org/10.1016/j.porgcoat.2013.10.007>.
- [34] L. Castillo-Henríquez, M. Brenes-Acuña, A. Castro-Rojas, R. Cordero-Salmerón, M. Lopretti-Correa, and J. R. Vega-Baudrit, “Biosensors for the Detection of Bacterial and Viral Clinical Pathogens,” *Sensors*, vol. 20, no. 23. 2020. doi: 10.3390/s20236926.
- [35] J. I. Cutler, E. Auyeung, and C. A. Mirkin, “Spherical Nucleic Acids,” *J. Am. Chem. Soc.*, vol. 134, no. 3, pp. 1376–1391, Jan. 2012, doi: 10.1021/ja209351u.
- [36] J. J. Storhoff, R. Elghanian, R. C. Mucic, C. A. Mirkin, and R. L. Letsinger, “One-Pot Colorimetric Differentiation of Polynucleotides with Single Base Imperfections Using Gold Nanoparticle Probes,” *J. Am. Chem. Soc.*, vol. 120, no. 9, pp. 1959–1964, Mar. 1998, doi: 10.1021/ja972332i.
- [37] X. Zhang, M. R. Servos, and J. Liu, “Instantaneous and Quantitative Functionalization of Gold Nanoparticles with Thiolated DNA Using a pH-Assisted and Surfactant-Free Route,” *J. Am. Chem. Soc.*, vol. 134, no. 17, pp. 7266–7269, May 2012, doi:

- 10.1021/ja3014055.
- [38] Y. Hao, Y. Li, L. Song, and Z. Deng, “Flash Synthesis of Spherical Nucleic Acids with Record DNA Density,” *J. Am. Chem. Soc.*, vol. 143, no. 8, pp. 3065–3069, Mar. 2021, doi: 10.1021/jacs.1c00568.
- [39] P. A. Sharp, “The Centrality of RNA,” *Cell*, vol. 136, no. 4, pp. 577–580, 2009, doi: <https://doi.org/10.1016/j.cell.2009.02.007>.
- [40] Y. Liu and W. D. Wilson, “Quantitative Analysis of Small Molecule–Nucleic Acid Interactions with a Biosensor Surface and Surface Plasmon Resonance Detection BT - Drug-DNA Interaction Protocols,” K. R. Fox, Ed. Totowa, NJ: Humana Press, 2010, pp. 1–23. doi: 10.1007/978-1-60327-418-0_1.
- [41] D. Li, Y. Chen, and Z. Liu, “Boronate affinity materials for separation and molecular recognition: structure, properties and applications,” *Chem. Soc. Rev.*, vol. 44, no. 22, pp. 8097–8123, 2015, doi: 10.1039/C5CS00013K.
- [42] E. Kianfar, “Magnetic Nanoparticles in Targeted Drug Delivery: a Review,” *J. Supercond. Nov. Magn.*, vol. 34, no. 7, pp. 1709–1735, 2021, doi: 10.1007/s10948-021-05932-9.
- [43] M. Holzinger, A. Le Goff, and S. Cosnier, “Nanomaterials for biosensing applications: a review,” *Frontiers in Chemistry*, vol. 2, 2014. [Online]. Available: <https://www.frontiersin.org/articles/10.3389/fchem.2014.00063>
- [44] C. Martin-Rios, C. Demen-Meier, S. Gössling, and C. Cornuz, “Food waste management innovations in the foodservice industry,” *Waste Manag.*, vol. 79, pp. 196–206, Sep. 2018, doi: 10.1016/j.wasman.2018.07.033.
- [45] S. M. Andler and J. M. Goddard, “Transforming food waste: how immobilized enzymes can valorize waste streams into revenue streams,” *npj Sci. Food*, vol. 2, no. 1, p. 19, 2018, doi: 10.1038/s41538-018-0028-2.
- [46] B. Thangaraj, P. R. Solomon, B. Muniyandi, S. Ranganathan, and L. Lin, “Catalysis in biodiesel production—a review,” *Clean Energy*, vol. 3, no. 1, pp. 2–23, Feb. 2019, doi: 10.1093/ce/zky020.
- [47] P. Chandra, Enespa, R. Singh, and P. K. Arora, “Microbial lipases and their industrial applications: a comprehensive review,” *Microb. Cell Fact.*, vol. 19, no. 1, p. 169, 2020,

doi: 10.1186/s12934-020-01428-8.

- [48] R. DiCosimo, J. McAuliffe, A. J. Poulouse, and G. Bohlmann, “Industrial use of immobilized enzymes,” *Chem. Soc. Rev.*, vol. 42, no. 15, pp. 6437–6474, 2013, doi: 10.1039/C3CS35506C.
- [49] S. Datta, L. R. Christena, and Y. R. S. Rajaram, “Enzyme immobilization: an overview on techniques and support materials,” *3 Biotech*, vol. 3, no. 1, pp. 1–9, 2013, doi: 10.1007/s13205-012-0071-7.
- [50] S. K. Sehmi *et al.*, “Antibacterial Surfaces with Activity against Antimicrobial Resistant Bacterial Pathogens and Endospores,” *ACS Infect. Dis.*, vol. 6, no. 5, pp. 939–946, May 2020, doi: 10.1021/acsinfecdis.9b00279.
- [51] J. Cui, Y. Shao, H. Zhang, H. Zhang, and J. Zhu, “Development of a novel silver ions-nanosilver complementary composite as antimicrobial additive for powder coating,” *Chem. Eng. J.*, vol. 420, p. 127633, 2021, doi: <https://doi.org/10.1016/j.cej.2020.127633>.
- [52] B. Deore *et al.*, “Direct printing of functional 3D objects using polymerization-induced phase separation,” *Nat. Commun.*, vol. 12, no. 1, p. 55, 2021, doi: 10.1038/s41467-020-20256-3.
- [53] H. Ishihama *et al.*, “An antibacterial coated polymer prevents biofilm formation and implant-associated infection,” *Sci. Rep.*, vol. 11, no. 1, p. 3602, 2021, doi: 10.1038/s41598-021-82992-w.
- [54] M. Moradi, J. T. Guimarães, and S. Sahin, “Current applications of exopolysaccharides from lactic acid bacteria in the development of food active edible packaging,” *Curr. Opin. Food Sci.*, vol. 40, pp. 33–39, 2021, doi: <https://doi.org/10.1016/j.cofs.2020.06.001>.
- [55] V. Ständert, K. Borcharding, N. Bormann, G. Schmidmaier, I. Grunwald, and B. Wildemann, “Antibiotic-loaded amphora-shaped pores on a titanium implant surface enhance osteointegration and prevent infections,” *Bioact. Mater.*, vol. 6, no. 8, pp. 2331–2345, 2021, doi: <https://doi.org/10.1016/j.bioactmat.2021.01.012>.
- [56] M. T. Bartling, S. Thümecke, J. H. Russert, A. Vilcinskas, and K.-Z. Lee, “Exposure to low doses of pesticides induces an immune response and the production of nitric oxide

- in honeybees,” *Sci. Rep.*, vol. 11, no. 1, p. 6819, 2021, doi: 10.1038/s41598-021-86293-0.
- [57] A. Balapure, Y. Nikhariya, N. S. Sriteja Boppudi, R. Ganesan, and J. Ray Dutta, “Highly Dispersed Nanocomposite of AgBr in g-C3N4 Matrix Exhibiting Efficient Antibacterial Effect on Drought-Resistant *Pseudomonas putida* under Dark and Light Conditions,” *ACS Appl. Mater. Interfaces*, vol. 12, no. 19, pp. 21481–21493, May 2020, doi: 10.1021/acsami.0c05158.
- [58] C. A. Arias and B. E. Murray, “Antibiotic-Resistant Bugs in the 21st Century — A Clinical Super-Challenge,” *N. Engl. J. Med.*, vol. 360, no. 5, pp. 439–443, Jan. 2009, doi: 10.1056/NEJMp0804651.
- [59] V. Zarghami, M. Ghorbani, K. Pooshang Bagheri, and M. A. Shokrgozar, “Melittin antimicrobial peptide thin layer on bone implant chitosan-antibiotic coatings and their bactericidal properties,” *Mater. Chem. Phys.*, vol. 263, p. 124432, 2021, doi: <https://doi.org/10.1016/j.matchemphys.2021.124432>.
- [60] I. Khan, N. Sivasankaran, R. Nagarjuna, R. Ganesan, and J. R. Dutta, “Extracellular probiotic lipase capped silver nanoparticles as highly efficient broad spectrum antimicrobial agents,” *RSC Adv.*, vol. 8, no. 55, pp. 31358–31365, 2018, doi: 10.1039/C8RA05999C.
- [61] V. Gopinath *et al.*, “Biogenic synthesis, characterization of antibacterial silver nanoparticles and its cell cytotoxicity,” *Arab. J. Chem.*, vol. 10, no. 8, pp. 1107–1117, 2017, doi: <https://doi.org/10.1016/j.arabjc.2015.11.011>.
- [62] M. Eltarahony, M. Abu-Serie, H. Hamad, S. Zaki, and D. Abd-El-Haleem, “Unveiling the role of novel biogenic functionalized CuFe hybrid nanocomposites in boosting anticancer, antimicrobial and biosorption activities,” *Sci. Rep.*, vol. 11, no. 1, p. 7790, 2021, doi: 10.1038/s41598-021-87363-z.
- [63] P. Dhandapani *et al.*, “Biological mediated synthesis of RGO-ZnO composites with enhanced photocatalytic and antibacterial activity,” *J. Hazard. Mater.*, vol. 409, p. 124661, 2021, doi: <https://doi.org/10.1016/j.jhazmat.2020.124661>.
- [64] H. Barabadi *et al.*, “Penicillium Family as Emerging Nanofactory for Biosynthesis of Green Nanomaterials: A Journey into the World of Microorganisms,” *J. Clust. Sci.*, vol.

- 30, no. 4, pp. 843–856, 2019, doi: 10.1007/s10876-019-01554-3.
- [65] H. Barabadi *et al.*, “Nanobiotechnology as an emerging approach to combat malaria: A systematic review,” *Nanomedicine Nanotechnology, Biol. Med.*, vol. 18, pp. 221–233, 2019, doi: <https://doi.org/10.1016/j.nano.2019.02.017>.
- [66] A. Khatua *et al.*, “Phytosynthesis, Characterization and Fungicidal Potential of Emerging Gold Nanoparticles Using Pongamia pinnata Leave Extract: A Novel Approach in Nanoparticle Synthesis,” *J. Clust. Sci.*, vol. 31, no. 1, pp. 125–131, 2020, doi: 10.1007/s10876-019-01624-6.
- [67] H. Barabadi *et al.*, “Emerging Theranostic Silver Nanomaterials to Combat Lung Cancer: A Systematic Review,” *J. Clust. Sci.*, vol. 31, no. 1, pp. 1–10, 2020, doi: 10.1007/s10876-019-01639-z.
- [68] H. Barabadi *et al.*, “Emerging Theranostic Gold Nanomaterials to Combat Lung Cancer: A Systematic Review,” *J. Clust. Sci.*, vol. 31, no. 2, pp. 323–330, 2020, doi: 10.1007/s10876-019-01650-4.
- [69] H. Barabadi *et al.*, “Emerging Theranostic Silver and Gold Nanomaterials to Combat Prostate Cancer: A Systematic Review,” *J. Clust. Sci.*, vol. 30, no. 6, pp. 1375–1382, 2019, doi: 10.1007/s10876-019-01588-7.
- [70] H. Vahidi, H. Barabadi, and M. Saravanan, “Emerging Selenium Nanoparticles to Combat Cancer: a Systematic Review,” *J. Clust. Sci.*, vol. 31, no. 2, pp. 301–309, 2020, doi: 10.1007/s10876-019-01671-z.
- [71] H. Barabadi *et al.*, “Emerging Theranostic Silver Nanomaterials to Combat Colorectal Cancer: A Systematic Review,” *J. Clust. Sci.*, vol. 31, no. 2, pp. 311–321, 2020, doi: 10.1007/s10876-019-01668-8.
- [72] H. Barabadi, H. Vahidi, K. Damavandi Kamali, M. Rashedi, O. Hosseini, and M. Saravanan, “Emerging Theranostic Gold Nanomaterials to Combat Colorectal Cancer: A Systematic Review,” *J. Clust. Sci.*, vol. 31, no. 4, pp. 651–658, 2020, doi: 10.1007/s10876-019-01681-x.
- [73] M. Saravanan, H. Barabadi, B. Ramachandran, G. Venkatraman, and K. Ponmurugan, “Chapter Eleven - Emerging plant-based anti-cancer green nanomaterials in present scenario,” in *Engineered Nanomaterials and Phytonanotechnology: Challenges for*

- Plant Sustainability*, vol. 87, S. K. Verma and A. K. B. T.-C. A. C. Das, Eds. Elsevier, 2019, pp. 291–318. doi: <https://doi.org/10.1016/bs.coac.2019.09.001>.
- [74] H. Barabadi, H. Vahidi, K. Damavandi Kamali, M. Rashedi, and M. Saravanan, “Antineoplastic Biogenic Silver Nanomaterials to Combat Cervical Cancer: A Novel Approach in Cancer Therapeutics,” *J. Clust. Sci.*, vol. 31, no. 4, pp. 659–672, 2020, doi: [10.1007/s10876-019-01697-3](https://doi.org/10.1007/s10876-019-01697-3).
- [75] J. Markus *et al.*, “Intracellular synthesis of gold nanoparticles with antioxidant activity by probiotic *Lactobacillus kimchicus* DCY51T isolated from Korean kimchi,” *Enzyme Microb. Technol.*, vol. 95, pp. 85–93, 2016, doi: <https://doi.org/10.1016/j.enzmictec.2016.08.018>.
- [76] M. L. Ermini and V. Voliani, “Antimicrobial Nano-Agents: The Copper Age,” *ACS Nano*, vol. 15, no. 4, pp. 6008–6029, Apr. 2021, doi: [10.1021/acsnano.0c10756](https://doi.org/10.1021/acsnano.0c10756).
- [77] E. Ozkan, E. Allan, and I. P. Parkin, “White-Light-Activated Antibacterial Surfaces Generated by Synergy between Zinc Oxide Nanoparticles and Crystal Violet,” *ACS Omega*, vol. 3, no. 3, pp. 3190–3199, Mar. 2018, doi: [10.1021/acsomega.7b01473](https://doi.org/10.1021/acsomega.7b01473).
- [78] A. S. Montaser, K. Jlassi, M. A. Ramadan, A. A. Sleem, and M. F. Attia, “Alginate, gelatin, and carboxymethyl cellulose coated nonwoven fabrics containing antimicrobial AgNPs for skin wound healing in rats,” *Int. J. Biol. Macromol.*, vol. 173, pp. 203–210, 2021, doi: <https://doi.org/10.1016/j.ijbiomac.2021.01.123>.
- [79] S. Azlin-Hasim, M. C. Cruz-Romero, M. A. Morris, E. Cummins, and J. P. Kerry, “Spray coating application for the development of nanocoated antimicrobial low-density polyethylene films to increase the shelf life of chicken breast fillets,” *Food Sci. Technol. Int.*, vol. 24, no. 8, pp. 688–698, Jul. 2018, doi: [10.1177/1082013218789224](https://doi.org/10.1177/1082013218789224).
- [80] F. Ohashi and A. Shibahara, “Antibacterial and antifungal properties of clear coating film containing silver–cytokinin complex as a filler,” *J. Coatings Technol. Res.*, vol. 17, no. 6, pp. 1619–1623, 2020, doi: [10.1007/s11998-020-00399-0](https://doi.org/10.1007/s11998-020-00399-0).
- [81] K. S. Siddiqi, A. Husen, and R. A. K. Rao, “A review on biosynthesis of silver nanoparticles and their biocidal properties,” *J. Nanobiotechnology*, vol. 16, no. 1, p. 14, 2018, doi: [10.1186/s12951-018-0334-5](https://doi.org/10.1186/s12951-018-0334-5).
- [82] M. Rafique, I. Sadaf, M. S. Rafique, and M. B. Tahir, “A review on green synthesis of

- silver nanoparticles and their applications,” *Artif. Cells, Nanomedicine, Biotechnol.*, vol. 45, no. 7, pp. 1272–1291, Oct. 2017, doi: 10.1080/21691401.2016.1241792.
- [83] G. Şeker Karatoprak, G. Aydın, B. Altinsoy, C. Altinkaynak, M. Koşar, and I. Ocsoy, “The Effect of *Pelargonium endlicherianum* Fenzl. root extracts on formation of nanoparticles and their antimicrobial activities,” *Enzyme Microb. Technol.*, vol. 97, pp. 21–26, 2017, doi: <https://doi.org/10.1016/j.enzmictec.2016.10.019>.
- [84] M. Shivakumar, K. L. Nagashree, S. Yallappa, S. Manjappa, K. S. Manjunath, and M. S. Dharmaprakash, “Biosynthesis of silver nanoparticles using pre-hydrolysis liquor of *Eucalyptus* wood and its effective antimicrobial activity,” *Enzyme Microb. Technol.*, vol. 97, pp. 55–62, 2017, doi: <https://doi.org/10.1016/j.enzmictec.2016.11.006>.
- [85] R. M. Ganesan and H. Gurumalles Prabu, “Synthesis of gold nanoparticles using herbal *Acorus calamus* rhizome extract and coating on cotton fabric for antibacterial and UV blocking applications,” *Arab. J. Chem.*, vol. 12, no. 8, pp. 2166–2174, 2019, doi: <https://doi.org/10.1016/j.arabjc.2014.12.017>.
- [86] M. A. Woodruff and D. W. Hutmacher, “The return of a forgotten polymer—Polycaprolactone in the 21st century,” *Prog. Polym. Sci.*, vol. 35, no. 10, pp. 1217–1256, 2010, doi: <https://doi.org/10.1016/j.progpolymsci.2010.04.002>.
- [87] E. B. Schlesinger *et al.*, “Device design methodology and formulation of a protein therapeutic for sustained release intraocular delivery,” *Bioeng. Transl. Med.*, vol. 4, no. 1, pp. 152–163, Jan. 2019, doi: <https://doi.org/10.1002/btm2.10121>.
- [88] L. Mei *et al.*, “A novel mifepristone-loaded implant for long-term treatment of endometriosis: In vitro and in vivo studies,” *Eur. J. Pharm. Sci.*, vol. 39, no. 5, pp. 421–427, 2010, doi: <https://doi.org/10.1016/j.ejps.2010.01.012>.
- [89] T. K. Dash and V. B. Konkimalla, “Poly-ε-caprolactone based formulations for drug delivery and tissue engineering: A review,” *J. Control. Release*, vol. 158, no. 1, pp. 15–33, 2012, doi: <https://doi.org/10.1016/j.jconrel.2011.09.064>.
- [90] Z.-M. Miao, S.-X. Cheng, X.-Z. Zhang, Q.-R. Wang, and R.-X. Zhuo, “Degradation and drug release property of star poly(ε-caprolactone)s with dendritic cores,” *J. Biomed. Mater. Res. Part B Appl. Biomater.*, vol. 81B, no. 1, pp. 40–49, Apr. 2007, doi: <https://doi.org/10.1002/jbm.b.30634>.

- [91] H. Pakalapati, M. A. Tariq, and S. K. Arumugasamy, "Optimization and modelling of enzymatic polymerization of ϵ -caprolactone to polycaprolactone using *Candida Antartica* Lipase B with response surface methodology and artificial neural network," *Enzyme Microb. Technol.*, vol. 122, pp. 7–18, 2019, doi: <https://doi.org/10.1016/j.enzmictec.2018.12.001>.
- [92] E. Gámez, G. Mendoza, S. Salido, M. Arruebo, and S. Irusta, "Antimicrobial Electrospun Polycaprolactone-Based Wound Dressings: An In Vitro Study About the Importance of the Direct Contact to Elicit Bactericidal Activity," *Adv. Wound Care*, vol. 8, no. 9, pp. 438–451, Mar. 2019, doi: [10.1089/wound.2018.0893](https://doi.org/10.1089/wound.2018.0893).
- [93] M. M. Lim and N. Sultana, "In vitro cytotoxicity and antibacterial activity of silver-coated electrospun polycaprolactone/gelatine nanofibrous scaffolds," *3 Biotech*, vol. 6, no. 2, p. 211, 2016, doi: [10.1007/s13205-016-0531-6](https://doi.org/10.1007/s13205-016-0531-6).
- [94] Z. Zhou *et al.*, "Antimicrobial Activity of 3D-Printed Poly(ϵ -Caprolactone) (PCL) Composite Scaffolds Presenting Vancomycin-Loaded Poly(lactic Acid-Glycolic Acid) (PLGA) Microspheres," *Med. Sci. Monit.*, vol. 24, pp. 6934–6945, 2018, doi: <https://dx.doi.org/10.12659/MSM.911770>.
- [95] Y. Gao, A. M. Hassanbhai, J. Lim, L. Wang, and C. Xu, "Fabrication of a silver octahedral nanoparticle-containing polycaprolactone nanocomposite for antibacterial bone scaffolds," *RSC Adv.*, vol. 7, no. 17, pp. 10051–10056, 2017, doi: [10.1039/C6RA26063B](https://doi.org/10.1039/C6RA26063B).
- [96] Z. Gounani, S. Pourianejad, M. A. Asadollahi, R. L. Meyer, J. M. Rosenholm, and A. Arpanaei, "Polycaprolactone-gelatin nanofibers incorporated with dual antibiotic-loaded carboxyl-modified silica nanoparticles," *J. Mater. Sci.*, vol. 55, no. 36, pp. 17134–17150, 2020, doi: [10.1007/s10853-020-05253-7](https://doi.org/10.1007/s10853-020-05253-7).
- [97] S. García-Salinas *et al.*, "Efficiency of Antimicrobial Electrospun Thymol-Loaded Polycaprolactone Mats In Vivo," *ACS Appl. Bio Mater.*, vol. 3, no. 5, pp. 3430–3439, May 2020, doi: [10.1021/acsabm.0c00419](https://doi.org/10.1021/acsabm.0c00419).
- [98] J. S. Lyu, J.-S. Lee, and J. Han, "Development of a biodegradable polycaprolactone film incorporated with an antimicrobial agent via an extrusion process," *Sci. Rep.*, vol. 9, no. 1, p. 20236, 2019, doi: [10.1038/s41598-019-56757-5](https://doi.org/10.1038/s41598-019-56757-5).

- [99] S. Radhakrishnan *et al.*, “Fabrication of 3D printed antimicrobial polycaprolactone scaffolds for tissue engineering applications,” *Mater. Sci. Eng. C*, vol. 118, p. 111525, 2021, doi: <https://doi.org/10.1016/j.msec.2020.111525>.
- [100] O. Sánchez-Aguinagalde, E. Meaurio, A. Lejardi, and J.-R. Sarasua, “Amorphous solid dispersions in poly(ϵ -caprolactone)/xanthohumol bioactive blends: physicochemical and mechanical characterization,” *J. Mater. Chem. B*, vol. 9, no. 20, pp. 4219–4229, 2021, doi: [10.1039/D0TB02964E](https://doi.org/10.1039/D0TB02964E).
- [101] I. Choi, D. S. Yoo, Y. Chang, S. Y. Kim, and J. Han, “Polycaprolactone film functionalized with bacteriophage T4 promotes antibacterial activity of food packaging toward *Escherichia coli*,” *Food Chem.*, vol. 346, p. 128883, 2021, doi: <https://doi.org/10.1016/j.foodchem.2020.128883>.
- [102] S. Ramyasree and J. R. Dutta, “The effect of process parameters in enhancement of lipase production by co-culture of lactic acid bacteria and their mutagenesis study,” *Biocatal. Agric. Biotechnol.*, vol. 2, no. 4, pp. 393–398, 2013, doi: <https://doi.org/10.1016/j.bcab.2013.08.002>.
- [103] R. Ganesan, H.-J. Lee, and J.-B. Kim, “Photoactive Diazoketo-Functionalized Self-Assembled Monolayer for Biomolecular Patterning,” *Langmuir*, vol. 25, no. 16, pp. 8888–8893, Aug. 2009, doi: [10.1021/la901870a](https://doi.org/10.1021/la901870a).
- [104] G. Amokrane *et al.*, “Electrospun Poly(ϵ -caprolactone) Fiber Scaffolds Functionalized by the Covalent Grafting of a Bioactive Polymer: Surface Characterization and Influence on in Vitro Biological Response,” *ACS Omega*, vol. 4, no. 17, pp. 17194–17208, Oct. 2019, doi: [10.1021/acsomega.9b01647](https://doi.org/10.1021/acsomega.9b01647).
- [105] M. S. Tabatabaei, R. Islam, and M. Ahmed, “Applications of gold nanoparticles in ELISA, PCR, and immuno-PCR assays: A review,” *Anal. Chim. Acta*, vol. 1143, pp. 250–266, 2021, doi: <https://doi.org/10.1016/j.aca.2020.08.030>.
- [106] H. Jin, Z. Sun, Y. Sun, and R. Gui, “Dual-signal ratiometric platforms: Construction principles and electrochemical biosensing applications at the live cell and small animal levels,” *TrAC Trends Anal. Chem.*, vol. 134, p. 116124, 2021, doi: <https://doi.org/10.1016/j.trac.2020.116124>.
- [107] F. Li, Y. Zhou, H. Yin, and S. Ai, “Recent advances on signal amplification strategies

- in photoelectrochemical sensing of microRNAs,” *Biosens. Bioelectron.*, vol. 166, p. 112476, 2020, doi: <https://doi.org/10.1016/j.bios.2020.112476>.
- [108] I. Khan, S. K. Vishwakarma, A. A. Khan, G. Ramakrishnan, and J. R. Dutta, “In vitro hemocompatibility evaluation of gold nanoparticles capped with *Lactobacillus plantarum* derived lipase,” *Clin. Hemorheol. Microcirc.*, vol. 69, pp. 197–205, 2018, doi: 10.3233/CH-189117.
- [109] I. Khan, R. Nagarjuna, J. Ray Dutta, and R. Ganesan, “Towards single crystalline, highly monodisperse and catalytically active gold nanoparticles capped with probiotic *Lactobacillus plantarum* derived lipase,” *Appl. Nanosci.*, vol. 9, no. 5, pp. 1101–1109, 2019, doi: 10.1007/s13204-018-0735-7.
- [110] S. Patil and R. Chandrasekaran, “Biogenic nanoparticles: a comprehensive perspective in synthesis, characterization, application and its challenges,” *J. Genet. Eng. Biotechnol.*, vol. 18, no. 1, p. 67, 2020, doi: 10.1186/s43141-020-00081-3.
- [111] L. De Sio *et al.*, “Photo-thermal effects in gold nanorods/DNA complexes,” *Micro Nano Syst. Lett.*, vol. 3, no. 1, p. 8, 2015, doi: 10.1186/s40486-015-0025-z.
- [112] S. Nakamura, H. Mitomo, Y. Yonamine, and K. Ijiri, “Salt-triggered Active Plasmonic Systems Based on the Assembly/Disassembly of Gold Nanorods in a DNA Brush Layer on a Solid Substrate,” *Chem. Lett.*, vol. 49, no. 7, pp. 749–752, Apr. 2020, doi: 10.1246/cl.200185.
- [113] R. Ota, Y. Fukushima, Y. Araki, K. Sasaki, T. Waku, and A. Kobori, “Ratiometric SERS Assays for Reliable and Automatic Quantification of Nucleic Acids,” *Chem. Lett.*, vol. 50, no. 3, pp. 513–517, Dec. 2020, doi: 10.1246/cl.200798.
- [114] A. Mobed, M. Hasanzadeh, M. Aghazadeh, A. Saadati, S. Hassanpour, and A. Mokhtarzadeh, “The bioconjugation of DNA with gold nanoparticles towards the spectrophotometric genosensing of pathogenic bacteria,” *Anal. Methods*, vol. 11, no. 33, pp. 4289–4298, 2019, doi: 10.1039/C9AY01339C.
- [115] C. Fournier-Wirth and J. Coste, “Nanotechnologies for pathogen detection: Future alternatives?,” *Biologicals*, vol. 38, no. 1, pp. 9–13, 2010, doi: <https://doi.org/10.1016/j.biologicals.2009.10.010>.
- [116] S. Khanna *et al.*, “A Simple Colorimetric Method for Naked-Eye Detection of

- Circulating Cell-Free DNA Using Unlabelled Gold Nanoparticles,” *ChemistrySelect*, vol. 3, no. 41, pp. 11541–11551, Nov. 2018, doi: <https://doi.org/10.1002/slct.201802671>.
- [117] A. Galdamez *et al.*, “DNA probe functionalization on different morphologies of ZnO/Au nanowire for bio-sensing applications,” *Mater. Lett.*, vol. 235, pp. 250–253, 2019, doi: <https://doi.org/10.1016/j.matlet.2018.10.026>.
- [118] Q. Xiao, Y. Zheng, J. Liu, S. Wang, and B. Feng, “Enzyme–antibody dual-film modified gold nanoparticle probe for ultrasensitive detection of alpha fetoprotein,” *Biologicals*, vol. 47, pp. 46–51, 2017, doi: <https://doi.org/10.1016/j.biologicals.2017.02.008>.
- [119] A. M. Aura, R. D’Agata, and G. Spoto, “Ultrasensitive Detection of Staphylococcus aureus and Listeria monocytogenes Genomic DNA by Nanoparticle-Enhanced Surface Plasmon Resonance Imaging,” *ChemistrySelect*, vol. 2, no. 24, pp. 7024–7030, Aug. 2017, doi: <https://doi.org/10.1002/slct.201700779>.
- [120] W. Jin and G. Maduraiveeran, “Nanomaterial-based environmental sensing platforms using state-of-the-art electroanalytical strategies,” *J. Anal. Sci. Technol.*, vol. 9, no. 1, p. 18, 2018, doi: 10.1186/s40543-018-0150-4.
- [121] H. Lee and S. H. Lee, “Single to three nucleotide polymorphisms assay of miRNA-21 using DNA capped gold nanoparticle-electrostatic force microscopy system,” *Micro Nano Syst. Lett.*, vol. 7, no. 1, p. 21, 2019, doi: 10.1186/s40486-019-0100-y.
- [122] B. Liu and J. Liu, “Methods for preparing DNA-functionalized gold nanoparticles, a key reagent of bioanalytical chemistry,” *Anal. Methods*, vol. 9, no. 18, pp. 2633–2643, 2017, doi: 10.1039/C7AY00368D.
- [123] F. Li, H. Zhang, B. Dever, X.-F. Li, and X. C. Le, “Thermal Stability of DNA Functionalized Gold Nanoparticles,” *Bioconjug. Chem.*, vol. 24, no. 11, pp. 1790–1797, Nov. 2013, doi: 10.1021/bc300687z.
- [124] K. Mahato *et al.*, “Gold nanoparticle surface engineering strategies and their applications in biomedicine and diagnostics,” *3 Biotech*, vol. 9, no. 2, p. 57, 2019, doi: 10.1007/s13205-019-1577-z.
- [125] N. Bhatt, P.-J. J. Huang, N. Dave, and J. Liu, “Dissociation and Degradation of Thiol-Modified DNA on Gold Nanoparticles in Aqueous and Organic Solvents,” *Langmuir*,

- vol. 27, no. 10, pp. 6132–6137, May 2011, doi: 10.1021/la200241d.
- [126] V. Chegel *et al.*, “Gold Nanoparticles Aggregation: Drastic Effect of Cooperative Functionalities in a Single Molecular Conjugate,” *J. Phys. Chem. C*, vol. 116, no. 4, pp. 2683–2690, Feb. 2012, doi: 10.1021/jp209251y.
- [127] J.-H. Choi, H. Kim, J.-H. Choi, J.-W. Choi, and B.-K. Oh, “Signal Enhancement of Silicon Nanowire-Based Biosensor for Detection of Matrix Metalloproteinase-2 Using DNA-Au Nanoparticle Complexes,” *ACS Appl. Mater. Interfaces*, vol. 5, no. 22, pp. 12023–12028, Nov. 2013, doi: 10.1021/am403816x.
- [128] M. Hu *et al.*, “Single-Step, Salt-Aging-Free, and Thiol-Free Freezing Construction of AuNP-Based Bioprobes for Advancing CRISPR-Based Diagnostics,” *J. Am. Chem. Soc.*, vol. 142, no. 16, pp. 7506–7513, Apr. 2020, doi: 10.1021/jacs.0c00217.
- [129] W. Lu *et al.*, “Quantitative investigation of the poly-adenine DNA dissociation from the surface of gold nanoparticles,” *Sci. Rep.*, vol. 5, no. 1, p. 10158, 2015, doi: 10.1038/srep10158.
- [130] Q. Zhang, Y. Tian, Z. Liang, Z. Wang, S. Xu, and Q. Ma, “DNA-Mediated Au–Au Dimer-Based Surface Plasmon Coupling Electrochemiluminescence Sensor for BRCA1 Gene Detection,” *Anal. Chem.*, vol. 93, no. 6, pp. 3308–3314, Feb. 2021, doi: 10.1021/acs.analchem.0c05440.
- [131] J. Sun *et al.*, “Dual-Mode Aptasensor Assembled by a WO₃/Fe₂O₃ Heterojunction for Paper-Based Colorimetric Prediction/Photoelectrochemical Multicomponent Analysis,” *ACS Appl. Mater. Interfaces*, vol. 13, no. 3, pp. 3645–3652, Jan. 2021, doi: 10.1021/acsami.0c19853.
- [132] W. Wang, X. Li, K. Tang, Z. Song, and X. Luo, “A AuNP-capped cage fluorescent biosensor based on controlled-release and cyclic enzymatic amplification for ultrasensitive detection of ATP,” *J. Mater. Chem. B*, vol. 8, no. 27, pp. 5945–5951, 2020, doi: 10.1039/D0TB00666A.
- [133] S. Kasturi, Y. Eom, S. R. Torati, and C. Kim, “Highly sensitive electrochemical biosensor based on naturally reduced rGO/Au nanocomposite for the detection of miRNA-122 biomarker,” *J. Ind. Eng. Chem.*, vol. 93, pp. 186–195, 2021, doi: <https://doi.org/10.1016/j.jiec.2020.09.022>.

- [134] A. S. Mohammed, R. Nagarjuna, M. N. Khaja, R. Ganesan, and J. Ray Dutta, "Effects of free patchy ends in ssDNA and dsDNA on gold nanoparticles in a colorimetric gene sensor for Hepatitis C virus RNA," *Microchim. Acta*, vol. 186, no. 8, p. 566, 2019, doi: 10.1007/s00604-019-3685-1.
- [135] A. S. Mohammed, A. Balapure, M. N. Khaja, R. Ganesan, and J. R. Dutta, "Naked-eye colorimetric detection of HCV RNA mediated by a 5' UTR-targeted antisense oligonucleotide and plasmonic gold nanoparticles," *Analyst*, vol. 146, no. 5, pp. 1569–1578, 2021, doi: 10.1039/D0AN02481C.
- [136] A. S. Mohammed, A. Balapure, A. A. Khan, M. N. Khaja, R. Ganesan, and J. R. Dutta, "Genotyping simplified: rationally designed antisense oligonucleotide-mediated PCR amplification-free colorimetric sensing of viral RNA in HCV genotypes 1 and 3," *Analyst*, vol. 146, no. 15, pp. 4767–4774, 2021, doi: 10.1039/D1AN00590A.
- [137] H. Li and G. Jie, "A versatile dendritical amplification photoelectric biosensing platform based on Bi₂S₃ nanorods and a perylene-based polymer for signal 'on' and 'off' double detection of DNA," *Analyst*, vol. 145, no. 16, pp. 5524–5531, 2020, doi: 10.1039/D0AN01040E.
- [138] G. Wang, J. Li, Y. He, J. Liu, M. Yu, and G. Wang, "Establishment of a universal and sensitive plasmonic biosensor platform based on the hybridization chain reaction (HCR) amplification induced by a triple-helix molecular switch," *Analyst*, vol. 145, no. 11, pp. 3864–3870, 2020, doi: 10.1039/D0AN00249F.
- [139] V. Chauhan, M. P. Singh, and R. K. Ratho, "Identification of T cell and B cell epitopes against Indian HCV-genotype-3a for vaccine development- An in silico analysis," *Biologicals*, vol. 53, pp. 63–71, 2018, doi: <https://doi.org/10.1016/j.biologicals.2018.02.003>.
- [140] F. Saad, M. Gadallah, A. Daif, N. Bedair, and M. A. Sakr, "Heparanase (HPSE) gene polymorphism (rs12503843) contributes as a risk factor for hepatocellular carcinoma (HCC): a pilot study among Egyptian patients," *J. Genet. Eng. Biotechnol.*, vol. 19, no. 1, p. 3, 2021, doi: 10.1186/s43141-020-00106-x.
- [141] J. Turkevich, P. C. Stevenson, and J. Hillier, "A study of the nucleation and growth processes in the synthesis of colloidal gold," *Discuss. Faraday Soc.*, vol. 11, no. 0, pp.

- 55–75, 1951, doi: 10.1039/DF9511100055.
- [142] M. Sanromán-Iglesias, C. H. Lawrie, T. Schäfer, M. Grzelczak, and L. M. Liz-Marzán, “Sensitivity Limit of Nanoparticle Biosensors in the Discrimination of Single Nucleotide Polymorphism,” *ACS Sensors*, vol. 1, no. 9, pp. 1110–1116, Sep. 2016, doi: 10.1021/acssensors.6b00393.
- [143] M. Li *et al.*, “Nucleic Acid Tests for Clinical Translation,” *Chem. Rev.*, vol. 121, no. 17, pp. 10469–10558, Sep. 2021, doi: 10.1021/acs.chemrev.1c00241.
- [144] C. Zheng *et al.*, “Rapid developments in lateral flow immunoassay for nucleic acid detection,” *Analyst*, vol. 146, no. 5, pp. 1514–1528, 2021, doi: 10.1039/D0AN02150D.
- [145] H. S. Prakash, P. A. Maraju, N. S. S. Boppudi, A. Balapure, R. Ganesan, and J. Ray Dutta, “Influence of citrate buffer and flash heating in enhancing the sensitivity of ratiometric genosensing of Hepatitis C virus using plasmonic gold nanoparticles,” *Micro Nano Syst. Lett.*, vol. 9, no. 1, p. 8, 2021, doi: 10.1186/s40486-021-00134-3.
- [146] J. Li *et al.*, “Amplification-free smartphone-based attomolar HBV detection,” *Biosens. Bioelectron.*, vol. 194, p. 113622, 2021, doi: <https://doi.org/10.1016/j.bios.2021.113622>.
- [147] S. Li *et al.*, “Entropy-driven amplification strategy-assisted lateral flow assay biosensor for ultrasensitive and convenient detection of nucleic acids,” *Analyst*, vol. 146, no. 5, pp. 1668–1674, 2021, doi: 10.1039/D0AN02273J.
- [148] N. Toropov *et al.*, “SARS-CoV-2 Tests: Bridging the Gap between Laboratory Sensors and Clinical Applications,” *ACS Sensors*, vol. 6, no. 8, pp. 2815–2837, Aug. 2021, doi: 10.1021/acssensors.1c00612.
- [149] N. Mohajeri, E. Mostafavi, and N. Zarghami, “The feasibility and usability of DNA-dot bioconjugation to antibody for targeted in vitro cancer cell fluorescence imaging,” *J. Photochem. Photobiol. B Biol.*, vol. 209, p. 111944, 2020, doi: <https://doi.org/10.1016/j.jphotobiol.2020.111944>.
- [150] C. Singhal, A. Ingle, D. Chakraborty, A. K. PN, C. S. Pundir, and J. Narang, “Impedimetric genosensor for detection of hepatitis C virus (HCV1) DNA using viral probe on methylene blue doped silica nanoparticles,” *Int. J. Biol. Macromol.*, vol. 98, pp. 84–93, 2017, doi: <https://doi.org/10.1016/j.ijbiomac.2017.01.093>.

- [151] S. D. Warkad, S. B. Nimse, K.-S. Song, and T. Kim, “Development of a Method for Screening and Genotyping of HCV 1a, 1b, 2, 3, 4, and 6 Genotypes,” *ACS Omega*, vol. 5, no. 19, pp. 10794–10799, May 2020, doi: 10.1021/acsomega.0c00386.
- [152] R.-Y. Huang *et al.*, “Development and evaluation of a sensitive enzyme-linked oligonucleotide-sorbent assay for detection of polymerase chain reaction-amplified hepatitis C virus of genotypes 1–6,” *J. Virol. Methods*, vol. 151, no. 2, pp. 211–216, 2008, doi: <https://doi.org/10.1016/j.jviromet.2008.05.006>.
- [153] M. Lereau *et al.*, “Development of Innovative and Versatile Polythiol Probes for Use on ELOSA or Electrochemical Biosensors: Application in Hepatitis C Virus Genotyping,” *Anal. Chem.*, vol. 85, no. 19, pp. 9204–9212, Oct. 2013, doi: 10.1021/ac401941x.
- [154] D.-C. Nyan and K. L. Swinson, “A method for rapid detection and genotype identification of hepatitis C virus 1–6 by one-step reverse transcription loop-mediated isothermal amplification,” *Int. J. Infect. Dis.*, vol. 43, pp. 30–36, 2016, doi: <https://doi.org/10.1016/j.ijid.2015.12.002>.
- [155] P. Kralik and M. Ricchi, “A Basic Guide to Real Time PCR in Microbial Diagnostics: Definitions, Parameters, and Everything ,” *Frontiers in Microbiology* , vol. 8. 2017. [Online]. Available: <https://www.frontiersin.org/articles/10.3389/fmicb.2017.00108>
- [156] H. M. T. Choi, V. A. Beck, and N. A. Pierce, “Next-Generation in Situ Hybridization Chain Reaction: Higher Gain, Lower Cost, Greater Durability,” *ACS Nano*, vol. 8, no. 5, pp. 4284–4294, May 2014, doi: 10.1021/nn405717p.
- [157] S. Bi, S. Yue, and S. Zhang, “Hybridization chain reaction: a versatile molecular tool for biosensing, bioimaging, and biomedicine,” *Chem. Soc. Rev.*, vol. 46, no. 14, pp. 4281–4298, 2017, doi: 10.1039/C7CS00055C.
- [158] M. M. Ali *et al.*, “Rolling circle amplification: a versatile tool for chemical biology, materials science and medicine,” *Chem. Soc. Rev.*, vol. 43, no. 10, pp. 3324–3341, 2014, doi: 10.1039/C3CS60439J.
- [159] A. Hassibi *et al.*, “Multiplexed identification, quantification and genotyping of infectious agents using a semiconductor biochip,” *Nat. Biotechnol.*, vol. 36, no. 8, pp. 738–745, 2018, doi: 10.1038/nbt.4179.
- [160] P. Sadeghi *et al.*, “Lateral flow assays (LFA) as an alternative medical diagnosis method

- for detection of virus species: The intertwine of nanotechnology with sensing strategies,” *TrAC Trends Anal. Chem.*, vol. 145, p. 116460, 2021, doi: <https://doi.org/10.1016/j.trac.2021.116460>.
- [161] Y. Han, F. Zhang, H. Gong, and C. Cai, “Double G-quadruplexes in a copper nanoparticle based fluorescent probe for determination of HIV genes,” *Microchim. Acta*, vol. 186, no. 1, p. 30, 2018, doi: 10.1007/s00604-018-3119-5.
- [162] F. Zhang, L. Xiang, X. Xiao, X. Chen, C. Chen, and C. Cai, “A rapid label- and enzyme-free G-quadruplex-based fluorescence strategy for highly-sensitive detection of HIV DNA,” *Analyst*, vol. 145, no. 1, pp. 206–212, 2020, doi: 10.1039/C9AN01847F.
- [163] R. R. G. Soares, N. Madaboosi, and M. Nilsson, “Rolling Circle Amplification in Integrated Microsystems: An Uncut Gem toward Massively Multiplexed Pathogen Diagnostics and Genotyping,” *Acc. Chem. Res.*, vol. 54, no. 21, pp. 3979–3990, Nov. 2021, doi: 10.1021/acs.accounts.1c00438.
- [164] Y. Liu and K.-L. Yang, “Applications of metal ions and liquid crystals for multiplex detection of DNA,” *J. Colloid Interface Sci.*, vol. 439, pp. 149–153, 2015, doi: <https://doi.org/10.1016/j.jcis.2014.10.038>.
- [165] L. Kashefi-Kheyrabadi *et al.*, “Rapid, multiplexed, and nucleic acid amplification-free detection of SARS-CoV-2 RNA using an electrochemical biosensor,” *Biosens. Bioelectron.*, vol. 195, p. 113649, 2022, doi: <https://doi.org/10.1016/j.bios.2021.113649>.
- [166] D. Khodakov, J. Li, J. X. Zhang, and D. Y. Zhang, “Highly multiplexed rapid DNA detection with single-nucleotide specificity via convective PCR in a portable device,” *Nat. Biomed. Eng.*, vol. 5, no. 7, pp. 702–712, 2021, doi: 10.1038/s41551-021-00755-4.
- [167] T. Jet, G. Gines, Y. Rondelez, and V. Taly, “Advances in multiplexed techniques for the detection and quantification of microRNAs,” *Chem. Soc. Rev.*, vol. 50, no. 6, pp. 4141–4161, 2021, doi: 10.1039/D0CS00609B.
- [168] X. Wang, N. Choi, Z. Cheng, J. Ko, L. Chen, and J. Choo, “Simultaneous Detection of Dual Nucleic Acids Using a SERS-Based Lateral Flow Assay Biosensor,” *Anal. Chem.*, vol. 89, no. 2, pp. 1163–1169, Jan. 2017, doi: 10.1021/acs.analchem.6b03536.
- [169] Y. Zheng *et al.*, “Dual-probe fluorescent biosensor based on T7 exonuclease-assisted

- target recycling amplification for simultaneous sensitive detection of microRNA-21 and microRNA-155,” *Anal. Bioanal. Chem.*, vol. 413, no. 6, pp. 1605–1614, 2021, doi: 10.1007/s00216-020-03121-6.
- [170] B. Li, X. Zhou, H. Liu, H. Deng, R. Huang, and D. Xing, “Simultaneous Detection of Antibiotic Resistance Genes on Paper-Based Chip Using [Ru(phen)2dppz]2+ Turn-on Fluorescence Probe,” *ACS Appl. Mater. Interfaces*, vol. 10, no. 5, pp. 4494–4501, Feb. 2018, doi: 10.1021/acsami.7b17653.
- [171] Y. Han, F. Zhang, H. Gong, and C. Cai, “Functional three helix molecular beacon fluorescent ‘turn-on’ probe for simple and sensitive simultaneous detection of two HIV DNAs,” *Sensors Actuators B Chem.*, vol. 281, pp. 303–310, 2019, doi: <https://doi.org/10.1016/j.snb.2018.10.110>.
- [172] L. Xiang, F. Zhang, C. Chen, and C. Cai, “A general scheme for fluorometric detection of multiple oligonucleotides by using RNA-cleaving DNAzymes: application to the determination of microRNA-141 and H5N1 virus DNA,” *Microchim. Acta*, vol. 186, no. 8, p. 511, 2019, doi: 10.1007/s00604-019-3595-2.
- [173] R. Zou, F. Zhang, C. Chen, and C. Cai, “DNA-programming multicolor silver nanoclusters for sensitively simultaneous detection of two HIV DNAs,” *Sensors Actuators B Chem.*, vol. 296, p. 126608, 2019, doi: <https://doi.org/10.1016/j.snb.2019.05.085>.
- [174] S. Moraes Silva, R. Tavallaie, L. Sandiford, R. D. Tilley, and J. J. Gooding, “Gold coated magnetic nanoparticles: from preparation to surface modification for analytical and biomedical applications,” *Chem. Commun.*, vol. 52, no. 48, pp. 7528–7540, 2016, doi: 10.1039/C6CC03225G.
- [175] J. K. Patra and K.-H. Baek, “Green biosynthesis of magnetic iron oxide (Fe₃O₄) nanoparticles using the aqueous extracts of food processing wastes under photocatalyzed condition and investigation of their antimicrobial and antioxidant activity,” *J. Photochem. Photobiol. B Biol.*, vol. 173, pp. 291–300, 2017, doi: <https://doi.org/10.1016/j.jphotobiol.2017.05.045>.
- [176] D. Patra, R. Ganesan, and B. Gopalan, “Hydrogen generation rate enhancement by in situ Fe(0) and nitroarene substrates in Fe₃O₄@Pd catalyzed ammonia borane hydrolysis

- and nitroarene reduction tandem reaction,” *Int. J. Hydrogen Energy*, vol. 46, no. 50, pp. 25486–25499, 2021, doi: <https://doi.org/10.1016/j.ijhydene.2021.05.106>.
- [177] S. Challagulla, R. Nagarjuna, R. Ganesan, and S. Roy, “Acrylate-based Polymerizable Sol–Gel Synthesis of Magnetically Recoverable TiO₂ Supported Fe₃O₄ for Cr(VI) Photoreduction in Aerobic Atmosphere,” *ACS Sustain. Chem. Eng.*, vol. 4, no. 3, pp. 974–982, Mar. 2016, doi: 10.1021/acssuschemeng.5b01055.
- [178] D. Patra, B. Gopalan, and R. Ganesan, “Direct solid-state synthesis of maghemite as a magnetically recoverable adsorbent for the abatement of methylene blue,” *J. Environ. Chem. Eng.*, vol. 7, no. 5, p. 103384, 2019, doi: <https://doi.org/10.1016/j.jece.2019.103384>.
- [179] I. Y. Goon, L. M. H. Lai, M. Lim, R. Amal, and J. J. Gooding, “‘Dispersible electrodes’: a solution to slow response times of sensitive sensors,” *Chem. Commun.*, vol. 46, no. 46, pp. 8821–8823, 2010, doi: 10.1039/C0CC02690E.
- [180] C. Miao *et al.*, “Lipase immobilization on amino-silane modified superparamagnetic Fe₃O₄ nanoparticles as biocatalyst for biodiesel production,” *Fuel*, vol. 224, pp. 774–782, 2018, doi: <https://doi.org/10.1016/j.fuel.2018.02.149>.
- [181] M. H. Mahmoudian, M. Fazlzadeh, M. H. Niari, A. Azari, and E. C. Lima, “A novel silica supported chitosan/glutaraldehyde as an efficient sorbent in solid phase extraction coupling with HPLC for the determination of Penicillin G from water and wastewater samples,” *Arab. J. Chem.*, vol. 13, no. 9, pp. 7147–7159, 2020, doi: <https://doi.org/10.1016/j.arabjc.2020.07.020>.
- [182] Y. Morono, K. Kubota, D. Tsukagoshi, and T. Terada, “EDTA-FISH: A Simple and Effective Approach to Reduce Non-specific Adsorption of Probes in Fluorescence *in situ* Hybridization (FISH) for Environmental Samples,” *Microbes Environ.*, vol. 35, no. 3, 2020, doi: 10.1264/jsme2.ME20062.
- [183] S. Liu, P. Wu, W. Li, H. Zhang, and C. Cai, “Ultrasensitive and Selective Electrochemical Identification of Hepatitis C Virus Genotype 1b Based on Specific Endonuclease Combined with Gold Nanoparticles Signal Amplification,” *Anal. Chem.*, vol. 83, no. 12, pp. 4752–4758, Jun. 2011, doi: 10.1021/ac200624f.
- [184] X. Zhi *et al.*, “A novel HBV genotypes detecting system combined with microfluidic

- chip, loop-mediated isothermal amplification and GMR sensors,” *Biosens. Bioelectron.*, vol. 54, pp. 372–377, 2014, doi: <https://doi.org/10.1016/j.bios.2013.11.025>.
- [185] L. Xu, J. Duan, J. Chen, S. Ding, and W. Cheng, “Recent advances in rolling circle amplification-based biosensing strategies-A review,” *Anal. Chim. Acta*, vol. 1148, p. 238187, 2021, doi: <https://doi.org/10.1016/j.aca.2020.12.062>.
- [186] Q. Tian, P. Keshri, and M. You, “Recent developments in DNA-based mechanical nanodevices,” *Chem. Commun.*, vol. 58, no. 30, pp. 4700–4710, 2022, doi: [10.1039/D2CC00302C](https://doi.org/10.1039/D2CC00302C).
- [187] M. A. Pellitero, A. Shaver, and N. Arroyo-Currás, “Critical Review—Approaches for the Electrochemical Interrogation of DNA-Based Sensors: A Critical Review,” *J. Electrochem. Soc.*, vol. 167, no. 3, p. 37529, 2020, doi: [10.1149/2.0292003JES](https://doi.org/10.1149/2.0292003JES).
- [188] P. A. Maraju, R. Ganesan, and J. R. Dutta, “Fluorescence-based simultaneous dual oligo sensing of HCV genotypes 1 and 3 using magnetite nanoparticles,” *J. Photochem. Photobiol. B Biol.*, vol. 232, p. 112463, 2022, doi: <https://doi.org/10.1016/j.jphotobiol.2022.112463>.
- [189] B. Marco-Dufort, R. Iten, and M. W. Tibbitt, “Linking Molecular Behavior to Macroscopic Properties in Ideal Dynamic Covalent Networks,” *J. Am. Chem. Soc.*, vol. 142, no. 36, pp. 15371–15385, Sep. 2020, doi: [10.1021/jacs.0c06192](https://doi.org/10.1021/jacs.0c06192).
- [190] Q. Wang, H. Yin, Y. Zhou, J. Wang, and S. Ai, “Photoelectrochemical biosensor for 5-formylcytosine deoxyribonucleoside detection based on BiIO₄-WS₂/CuO ternary heterojunction,” *Sensors Actuators B Chem.*, vol. 341, p. 130019, 2021, doi: <https://doi.org/10.1016/j.snb.2021.130019>.
- [191] X. Wu, Z. Li, X.-X. Chen, J. S. Fossey, T. D. James, and Y.-B. Jiang, “Selective sensing of saccharides using simple boronic acids and their aggregates,” *Chem. Soc. Rev.*, vol. 42, no. 20, pp. 8032–8048, 2013, doi: [10.1039/C3CS60148J](https://doi.org/10.1039/C3CS60148J).
- [192] R. Nishiyabu, S. Iizuka, S. Minegishi, H. Kitagishi, and Y. Kubo, “Surface modification of a polyvinyl alcohol sponge with functionalized boronic acids to develop porous materials for multicolor emission, chemical sensing and 3D cell culture,” *Chem. Commun.*, vol. 53, no. 25, pp. 3563–3566, 2017, doi: [10.1039/C7CC00490G](https://doi.org/10.1039/C7CC00490G).
- [193] J. T. George and S. G. Srivatsan, “Bioorthogonal chemistry-based RNA labeling

- technologies: evolution and current state,” *Chem. Commun.*, vol. 56, no. 82, pp. 12307–12318, 2020, doi: 10.1039/D0CC05228K.
- [194] L. Wu *et al.*, “ESIPT-based ratiometric fluorescence probe for the intracellular imaging of peroxyxynitrite,” *Chem. Commun.*, vol. 54, no. 71, pp. 9953–9956, 2018, doi: 10.1039/C8CC04919J.
- [195] A. Galstyan, R. Schiller, and U. Dobrindt, “Boronic Acid Functionalized Photosensitizers: A Strategy To Target the Surface of Bacteria and Implement Active Agents in Polymer Coatings,” *Angew. Chemie Int. Ed.*, vol. 56, no. 35, pp. 10362–10366, Aug. 2017, doi: <https://doi.org/10.1002/anie.201703398>.
- [196] B. J. Graham, I. W. Windsor, B. Gold, and R. T. Raines, “Boronic acid with high oxidative stability and utility in biological contexts,” *Proc. Natl. Acad. Sci.*, vol. 118, no. 10, p. e2013691118, Mar. 2021, doi: 10.1073/pnas.2013691118.
- [197] W. Zhai, L. Male, and J. S. Fossey, “Glucose selective bis-boronic acid click-fluor,” *Chem. Commun.*, vol. 53, no. 14, pp. 2218–2221, 2017, doi: 10.1039/C6CC08534B.
- [198] A. R. Martin, I. Barvik, D. Luvino, M. Smietana, and J.-J. Vasseur, “Dynamic and Programmable DNA-Templated Boronic Ester Formation,” *Angew. Chemie Int. Ed.*, vol. 50, no. 18, pp. 4193–4196, Apr. 2011, doi: <https://doi.org/10.1002/anie.201007170>.
- [199] F. Li *et al.*, “Spatiotemporally programmable cascade hybridization of hairpin DNA in polymeric nanoframework for precise siRNA delivery,” *Nat. Commun.*, vol. 12, no. 1, p. 1138, 2021, doi: 10.1038/s41467-021-21442-7.
- [200] N. Yoshinaga *et al.*, “mRNA loading into ATP-responsive polyplex micelles with optimal density of phenylboronate ester crosslinking to balance robustness in the biological milieu and intracellular translational efficiency,” *J. Control. Release*, vol. 330, pp. 317–328, 2021, doi: <https://doi.org/10.1016/j.jconrel.2020.12.033>.
- [201] S. Qian *et al.*, “Boronic Acid Functionalized Au Nanoparticles for Selective MicroRNA Signal Amplification in Fiber-Optic Surface Plasmon Resonance Sensing System,” *ACS Sensors*, vol. 3, no. 5, pp. 929–935, May 2018, doi: 10.1021/acssensors.7b00871.
- [202] L. Liu *et al.*, “Simple, sensitive and label-free electrochemical detection of microRNAs based on the in situ formation of silver nanoparticles aggregates for signal amplification,” *Biosens. Bioelectron.*, vol. 94, pp. 235–242, 2017, doi:

<https://doi.org/10.1016/j.bios.2017.02.041>.

- [203] J. Ding, F. Liu, C. Qi, Y. Zhou, H. Yin, and S. Ai, “Enhanced photoactivity of perovskite Bi₄NbO₈Cl/PTC-NH₂ heterojunction and its application for photoelectrochemical sensing of DNA hydroxymethylation,” *Sensors Actuators B Chem.*, vol. 344, p. 130211, 2021, doi: <https://doi.org/10.1016/j.snb.2021.130211>.
- [204] Y.-Y. Aung, A. N. Kristanti, H. V. Lee, and M. Z. Fahmi, “Boronic-Acid-Modified Nanomaterials for Biomedical Applications,” *ACS Omega*, vol. 6, no. 28, pp. 17750–17765, Jul. 2021, doi: 10.1021/acsomega.1c01352.
- [205] Y. Li, Z. Zhang, B. Liu, and J. Liu, “Adsorption of DNA Oligonucleotides by Boronic Acid-Functionalized Hydrogel Nanoparticles,” *Langmuir*, vol. 35, no. 42, pp. 13727–13734, Oct. 2019, doi: 10.1021/acs.langmuir.9b01622.
- [206] G. Pina Luis, M. Granda, M. Granda, R. Badía, and M. Elena Díaz-García, “Selective fluorescent chemosensor for fructose,” *Analyst*, vol. 123, no. 1, pp. 155–158, 1998, doi: 10.1039/A703778C.
- [207] S. R. Nalluri, R. Nagarjuna, D. Patra, R. Ganesan, and G. Balaji, “Large Scale Solid-state Synthesis of Catalytically Active Fe₃O₄@M (M = Au, Ag and Au-Ag alloy) Core-shell Nanostructures,” *Sci. Rep.*, vol. 9, no. 1, p. 6603, 2019, doi: 10.1038/s41598-019-43116-7.
- [208] G. Liu, J. Li, D.-Q. Feng, J.-J. Zhu, and W. Wang, “Silver Nanoclusters Beacon as Stimuli-Responsive Versatile Platform for Multiplex DNAs Detection and Aptamer–Substrate Complexes Sensing,” *Anal. Chem.*, vol. 89, no. 1, pp. 1002–1008, Jan. 2017, doi: 10.1021/acs.analchem.6b04362.
- [209] Y. Zhang *et al.*, “DNA-Templated Silver Nanoclusters for Multiplexed Fluorescent DNA Detection,” *Small*, vol. 11, no. 12, pp. 1385–1389, Mar. 2015, doi: <https://doi.org/10.1002/sml.201402044>.
- [210] L. Zhu *et al.*, “Selective amyloid β oligomer assay based on abasic site-containing molecular beacon and enzyme-free amplification,” *Biosens. Bioelectron.*, vol. 78, pp. 206–212, 2016, doi: <https://doi.org/10.1016/j.bios.2015.11.048>.
- [211] L. Liu, N. Xia, J. Zhang, W. Mao, Y. Wu, and X. Ge, “A graphene oxide-based fluorescent platform for selective detection of amyloid- β oligomers,” *Anal. Methods*,

- vol. 7, no. 20, pp. 8727–8732, 2015, doi: 10.1039/C5AY02018B.
- [212] D.-L. Ma, H.-Z. He, K.-H. Leung, H.-J. Zhong, D. S.-H. Chan, and C.-H. Leung, “Label-free luminescent oligonucleotide-based probes,” *Chem. Soc. Rev.*, vol. 42, no. 8, pp. 3427–3440, 2013, doi: 10.1039/C2CS35472A.
- [213] W. Xu, K. M. Chan, and E. T. Kool, “Fluorescent nucleobases as tools for studying DNA and RNA,” *Nat. Chem.*, vol. 9, no. 11, pp. 1043–1055, 2017, doi: 10.1038/nchem.2859.
- [214] J. N. Murphy, A. K. H. Cheng, H.-Z. Yu, and D. Bizzotto, “On the Nature of DNA Self-Assembled Monolayers on Au: Measuring Surface Heterogeneity with Electrochemical in Situ Fluorescence Microscopy,” *J. Am. Chem. Soc.*, vol. 131, no. 11, pp. 4042–4050, Mar. 2009, doi: 10.1021/ja808696p.
- [215] M. C. Brothers *et al.*, “Impact of Self-Assembled Monolayer Design and Electrochemical Factors on Impedance-Based Biosensing,” *Sensors*, vol. 20, no. 8, 2020. doi: 10.3390/s20082246.
- [216] Y. Zhang, Y. Li, Y. Wei, H. Sun, and H. Wang, “A sensitive signal-off electrogenerated chemiluminescence biosensing method for the discrimination of DNA hydroxymethylation based on glycosylation modification and signal quenching from ferroceneboronic acid,” *Talanta*, vol. 170, pp. 546–551, 2017, doi: <https://doi.org/10.1016/j.talanta.2017.04.051>.
- [217] J. Song *et al.*, “Multiplex Detection of DNA Mutations by the Fluorescence Fingerprint Spectrum Technique,” *Angew. Chemie Int. Ed.*, vol. 52, no. 49, pp. 13020–13023, Dec. 2013, doi: <https://doi.org/10.1002/anie.201305461>.
- [218] Y. Duan *et al.*, “Mechanically Triggered Hybridization Chain Reaction,” *Angew. Chemie Int. Ed.*, vol. 60, no. 36, pp. 19974–19981, Sep. 2021, doi: <https://doi.org/10.1002/anie.202107660>.
- [219] H. Hosseinzadeh-Bandbafha *et al.*, “Environmental life cycle assessment of biodiesel production from waste cooking oil: A systematic review,” *Renew. Sustain. Energy Rev.*, vol. 161, p. 112411, 2022, doi: <https://doi.org/10.1016/j.rser.2022.112411>.
- [220] Z. Abdin, A. Zafaranloo, A. Rafiee, W. Mérida, W. Lipiński, and K. R. Khalilpour, “Hydrogen as an energy vector,” *Renew. Sustain. Energy Rev.*, vol. 120, p. 109620,

- 2020, doi: <https://doi.org/10.1016/j.rser.2019.109620>.
- [221] S. Sadekin, S. Zaman, M. Mahfuz, and R. Sarkar, “Nuclear power as foundation of a clean energy future: A review,” *Energy Procedia*, vol. 160, pp. 513–518, 2019, doi: <https://doi.org/10.1016/j.egypro.2019.02.200>.
- [222] M. M. El-Sheekh, M. Y. Bedaiwy, A. A. El-Nagar, M. ElKelawy, and H. Alm-Eldin Bastawissi, “Ethanol biofuel production and characteristics optimization from wheat straw hydrolysate: Performance and emission study of DI-diesel engine fueled with diesel/biodiesel/ethanol blends,” *Renew. Energy*, vol. 191, pp. 591–607, 2022, doi: <https://doi.org/10.1016/j.renene.2022.04.076>.
- [223] J. Gallagher *et al.*, “Adapting Stand-Alone Renewable Energy Technologies for the Circular Economy through Eco-Design and Recycling,” *J. Ind. Ecol.*, vol. 23, no. 1, pp. 133–140, Feb. 2019, doi: <https://doi.org/10.1111/jiec.12703>.
- [224] T.-L. Chen, H. Kim, S.-Y. Pan, P.-C. Tseng, Y.-P. Lin, and P.-C. Chiang, “Implementation of green chemistry principles in circular economy system towards sustainable development goals: Challenges and perspectives,” *Sci. Total Environ.*, vol. 716, p. 136998, 2020, doi: <https://doi.org/10.1016/j.scitotenv.2020.136998>.
- [225] N. Eghtesadi *et al.*, “Electroactivity of weak electricigen *Bacillus subtilis* biofilms in solution containing deep eutectic solvent components,” *Bioelectrochemistry*, vol. 147, p. 108207, 2022, doi: <https://doi.org/10.1016/j.bioelechem.2022.108207>.
- [226] R. Ganesan *et al.*, “A review on prospective production of biofuel from microalgae,” *Biotechnol. Reports*, vol. 27, p. e00509, 2020, doi: <https://doi.org/10.1016/j.btre.2020.e00509>.
- [227] V. K. Mishra and R. Goswami, “A review of production, properties and advantages of biodiesel,” *Biofuels*, vol. 9, no. 2, pp. 273–289, Mar. 2018, doi: [10.1080/17597269.2017.1336350](https://doi.org/10.1080/17597269.2017.1336350).
- [228] W.-J. Cong, S. Nanda, H. Li, Z. Fang, A. K. Dalai, and J. A. Kozinski, “Metal–organic framework-based functional catalytic materials for biodiesel production: a review,” *Green Chem.*, vol. 23, no. 7, pp. 2595–2618, 2021, doi: [10.1039/D1GC00233C](https://doi.org/10.1039/D1GC00233C).
- [229] K. Sangkharak, S. Mhaisawat, T. Rakkan, N. Paichid, and T. Yunu, “Utilization of mixed chicken waste for biodiesel production using single and combination of

- immobilized lipase as a catalyst,” *Biomass Convers. Biorefinery*, vol. 12, no. 5, pp. 1465–1478, 2022, doi: 10.1007/s13399-020-00842-7.
- [230] A. T. Hoang *et al.*, “Rice bran oil-based biodiesel as a promising renewable fuel alternative to petrodiesel: A review,” *Renew. Sustain. Energy Rev.*, vol. 135, p. 110204, 2021, doi: <https://doi.org/10.1016/j.rser.2020.110204>.
- [231] S. R. Uppada, M. Akula, A. Bhattacharya, and J. R. Dutta, “Immobilized lipase from *Lactobacillus plantarum* in meat degradation and synthesis of flavor esters,” *J. Genet. Eng. Biotechnol.*, vol. 15, no. 2, pp. 331–334, 2017, doi: <https://doi.org/10.1016/j.jgeb.2017.07.008>.
- [232] I. Khan, R. Nagarjuna, J. R. Dutta, and R. Ganesan, “Enzyme-Embedded Degradation of Poly(ϵ -caprolactone) using Lipase-Derived from Probiotic *Lactobacillus plantarum*,” *ACS Omega*, vol. 4, no. 2, pp. 2844–2852, Feb. 2019, doi: 10.1021/acsomega.8b02642.
- [233] W. Ssengooba *et al.*, “Whole genome sequencing to complement tuberculosis drug resistance surveys in Uganda,” *Infect. Genet. Evol.*, vol. 40, pp. 8–16, 2016, doi: <https://doi.org/10.1016/j.meegid.2016.02.019>.
- [234] I. Khan, R. Ganesan, and J. R. Dutta, “Probiotic lipase derived from *Lactobacillus plantarum* and *Lactobacillus brevis* for biodiesel production from waste cooking olive oil: an alternative feedstock,” *Int. J. Green Energy*, vol. 17, no. 1, pp. 62–70, Jan. 2020, doi: 10.1080/15435075.2019.1688157.
- [235] J. M. Marchetti, V. U. Miguel, and A. F. Errazu, “Techno-economic study of different alternatives for biodiesel production,” *Fuel Process. Technol.*, vol. 89, no. 8, pp. 740–748, 2008, doi: <https://doi.org/10.1016/j.fuproc.2008.01.007>.
- [236] V. Vescovi *et al.*, “Lipase-Catalyzed Production of Biodiesel by Hydrolysis of Waste Cooking Oil Followed by Esterification of Free Fatty Acids,” *J. Am. Oil Chem. Soc.*, vol. 93, no. 12, pp. 1615–1624, Dec. 2016, doi: <https://doi.org/10.1007/s11746-016-2901-y>.
- [237] X. Fan, “Enzymatic biodiesel production – the way of the future,” *Lipid Technol.*, vol. 24, no. 2, pp. 31–32, Feb. 2012, doi: <https://doi.org/10.1002/lite.201200169>.
- [238] H. T. Imam, P. C. Marr, and A. C. Marr, “Enzyme entrapment, biocatalyst immobilization without covalent attachment,” *Green Chem.*, vol. 23, no. 14, pp. 4980–

- 5005, 2021, doi: 10.1039/D1GC01852C.
- [239] Y. Hu, L. Dai, D. Liu, and W. Du, “Rationally designing hydrophobic UiO-66 support for the enhanced enzymatic performance of immobilized lipase,” *Green Chem.*, vol. 20, no. 19, pp. 4500–4506, 2018, doi: 10.1039/C8GC01284A.
- [240] P. Amruth Maroju, R. Ganesan, and J. Ray Dutta, “Biofuel generation from food waste through immobilized enzymes on magnetic nanoparticles,” *Mater. Today Proc.*, 2022, doi: <https://doi.org/10.1016/j.matpr.2022.05.555>.
- [241] J. Zhao *et al.*, “Characterization of a novel lipase from *Bacillus licheniformis* NCU CS-5 for applications in detergent industry and biodegradation of 2,4-D butyl ester,” *Int. J. Biol. Macromol.*, vol. 176, pp. 126–136, 2021, doi: <https://doi.org/10.1016/j.ijbiomac.2021.01.214>.
- [242] J. Zhao *et al.*, “Expression and characterization of a novel lipase from *Bacillus licheniformis* NCU CS-5 for application in enhancing fatty acids flavor release for low-fat cheeses,” *Food Chem.*, vol. 368, p. 130868, 2022, doi: <https://doi.org/10.1016/j.foodchem.2021.130868>.
- [243] I. Khan, J. Ray Dutta, and R. Ganesan, “*Lactobacillus* sps. lipase mediated poly (ϵ -caprolactone) degradation,” *Int. J. Biol. Macromol.*, vol. 95, pp. 126–131, 2017, doi: <https://doi.org/10.1016/j.ijbiomac.2016.11.040>.
- [244] A. Micsonai *et al.*, “BeStSel: a web server for accurate protein secondary structure prediction and fold recognition from the circular dichroism spectra,” *Nucleic Acids Res.*, vol. 46, no. W1, pp. W315–W322, Jul. 2018, doi: 10.1093/nar/gky497.
- [245] K. K. Haridhasapavalan, P. K. Sundaravadivelu, S. Bhattacharyya, S. H. Ranjan, K. Raina, and R. P. Thummer, “Generation of cell-permeant recombinant human transcription factor GATA4 from *E. coli*,” *Bioprocess Biosyst. Eng.*, vol. 44, no. 6, pp. 1131–1146, 2021, doi: 10.1007/s00449-021-02516-8.
- [246] N. J. Greenfield, “Using circular dichroism spectra to estimate protein secondary structure,” *Nat. Protoc.*, vol. 1, no. 6, pp. 2876–2890, 2006, doi: 10.1038/nprot.2006.202.
- [247] R. Nagarjuna, S. Challagulla, R. Ganesan, and S. Roy, “High rates of Cr(VI) photoreduction with magnetically recoverable nano-Fe₃O₄@Fe₂O₃/Al₂O₃ catalyst

- under visible light,” *Chem. Eng. J.*, vol. 308, pp. 59–66, 2017, doi: <https://doi.org/10.1016/j.cej.2016.09.044>.
- [248] H. Mude, P. A. Maraju, A. Balapure, R. Ganesan, and J. Ray Dutta, “Quaternized Polydopamine Coatings for Anchoring Molecularly Dispersed Broad-Spectrum Antimicrobial Silver Salts,” *ACS Appl. Bio Mater.*, vol. 4, no. 12, pp. 8396–8406, Dec. 2021, doi: 10.1021/acsbm.1c00952.
- [249] Z. Huang, T. Gengenbach, J. Tian, W. Shen, and G. Garnier, “Effect of Bovine Serum Albumin Treatment on the Aging and Activity of Antibodies in Paper Diagnostics ,” *Frontiers in Chemistry* , vol. 6. 2018. [Online]. Available: <https://www.frontiersin.org/articles/10.3389/fchem.2018.00161>
- [250] Z. Chen, L. Liu, and R. Yang, “Improved performance of immobilized lipase by interfacial activation on Fe₃O₄@PVBC nanoparticles,” *RSC Adv.*, vol. 7, no. 56, pp. 35169–35174, 2017, doi: 10.1039/C7RA05723G.
- [251] N. Dizge and B. Keskinler, “Enzymatic production of biodiesel from canola oil using immobilized lipase,” *Biomass and Bioenergy*, vol. 32, no. 12, pp. 1274–1278, 2008, doi: <https://doi.org/10.1016/j.biombioe.2008.03.005>.
- [252] N. Dizge, C. Aydinler, D. Y. Imer, M. Bayramoglu, A. Tanriseven, and B. Keskinler, “Biodiesel production from sunflower, soybean, and waste cooking oils by transesterification using lipase immobilized onto a novel microporous polymer,” *Bioresour. Technol.*, vol. 100, no. 6, pp. 1983–1991, 2009, doi: <https://doi.org/10.1016/j.biortech.2008.10.008>.
- [253] L. Li, W. Du, D. Liu, L. Wang, and Z. Li, “Lipase-catalyzed transesterification of rapeseed oils for biodiesel production with a novel organic solvent as the reaction medium,” *J. Mol. Catal. B Enzym.*, vol. 43, no. 1, pp. 58–62, 2006, doi: <https://doi.org/10.1016/j.molcatb.2006.06.012>.
- [254] S. Shah and M. N. Gupta, “Lipase catalyzed preparation of biodiesel from Jatropha oil in a solvent free system,” *Process Biochem.*, vol. 42, no. 3, pp. 409–414, 2007, doi: <https://doi.org/10.1016/j.procbio.2006.09.024>.
- [255] W. Xie and J. Wang, “Immobilized lipase on magnetic chitosan microspheres for transesterification of soybean oil,” *Biomass and Bioenergy*, vol. 36, pp. 373–380, 2012,

- doi: <https://doi.org/10.1016/j.biombioe.2011.11.006>.
- [256] M. Basri, M. A. Kassim, R. Mohamad, and A. B. Ariff, "Optimization and kinetic study on the synthesis of palm oil ester using Lipozyme TL IM," *J. Mol. Catal. B Enzym.*, vol. 85–86, pp. 214–219, 2013, doi: <https://doi.org/10.1016/j.molcatb.2012.09.013>.
- [257] M. Ilmi, A. Kloekhorst, J. G. M. Winkelman, G. J. W. Euverink, C. Hidayat, and H. J. Heeres, "Process intensification of catalytic liquid-liquid solid processes: Continuous biodiesel production using an immobilized lipase in a centrifugal contactor separator," *Chem. Eng. J.*, vol. 321, pp. 76–85, 2017, doi: <https://doi.org/10.1016/j.cej.2017.03.070>.
- [258] J. Li, J. Zhang, S. Shen, B. Zhang, and W. W. Yu, "Magnetic responsive *Thermomyces lanuginosus* lipase for biodiesel synthesis," *Mater. Today Commun.*, vol. 24, p. 101197, 2020, doi: <https://doi.org/10.1016/j.mtcomm.2020.101197>.
- [259] T. A. Andrade, M. Errico, and K. V Christensen, "Influence of the reaction conditions on the enzyme catalyzed transesterification of castor oil: A possible step in biodiesel production," *Bioresour. Technol.*, vol. 243, pp. 366–374, 2017, doi: <https://doi.org/10.1016/j.biortech.2017.06.118>.
- [260] J. H. C. Wancura *et al.*, "Improving the soluble lipase-catalyzed biodiesel production through a two-step hydroesterification reaction system," *Appl. Microbiol. Biotechnol.*, vol. 103, no. 18, pp. 7805–7817, 2019, doi: [10.1007/s00253-019-10075-y](https://doi.org/10.1007/s00253-019-10075-y).
- [261] H. M. Ahmed, S. S. Mohamed, H. A. Amin, M. E. Moharam, M. A. El-Bendary, and S. I. Hawash, "Semi-pilot scale production of biodiesel from waste frying oil by genetically improved fungal lipases," *Prep. Biochem. Biotechnol.*, vol. 50, no. 9, pp. 915–924, Oct. 2020, doi: [10.1080/10826068.2020.1771730](https://doi.org/10.1080/10826068.2020.1771730).
- [262] Y. Liu *et al.*, "Development of a *Pichia pastoris* whole-cell biocatalyst with overexpression of mutant lipase I PCLG47I from *Penicillium cyclopium* for biodiesel production," *RSC Adv.*, vol. 8, no. 46, pp. 26161–26168, 2018, doi: [10.1039/C8RA04462G](https://doi.org/10.1039/C8RA04462G).
- [263] J. Zhang *et al.*, "Heat-induced overexpression of the thermophilic lipase from *Bacillus thermocatenulatus* in *Escherichia coli* by fermentation and its application in preparation biodiesel using rapeseed oil," *Biotechnol. Appl. Biochem.*, vol. n/a, no. n/a, Sep. 2021, doi: <https://doi.org/10.1002/bab.2247>.

- [264] C. B. Hobuss, F. A. da Silva, M. A. Z. dos Santos, C. M. P. de Pereira, G. A. S. Schulz, and D. Bianchini, "Synthesis and characterization of monoacylglycerols through glycerolysis of ethyl esters derived from linseed oil by green processes," *RSC Adv.*, vol. 10, no. 4, pp. 2327–2336, 2020, doi: 10.1039/C9RA07834G.
- [265] G. Pathak, D. Das, K. Rajkumari, and S. L. Rokhum, "Exploiting waste: towards a sustainable production of biodiesel using *Musa acuminata* peel ash as a heterogeneous catalyst," *Green Chem.*, vol. 20, no. 10, pp. 2365–2373, 2018, doi: 10.1039/C8GC00071A.
- [266] M. Iuliano, M. Sarno, S. De Pasquale, and E. Ponticorvo, "Candida rugosa lipase for the biodiesel production from renewable sources," *Renew. Energy*, vol. 162, pp. 124–133, 2020, doi: <https://doi.org/10.1016/j.renene.2020.08.019>.
- [267] N. S. Kasim, T.-H. Tsai, S. Gunawan, and Y.-H. Ju, "Biodiesel production from rice bran oil and supercritical methanol," *Bioresour. Technol.*, vol. 100, no. 8, pp. 2399–2403, 2009, doi: <https://doi.org/10.1016/j.biortech.2008.11.041>.
- [268] S. Jain and M. P. Sharma, "Application of thermogravimetric analysis for thermal stability of *Jatropha curcas* biodiesel," *Fuel*, vol. 93, pp. 252–257, 2012, doi: <https://doi.org/10.1016/j.fuel.2011.09.002>.
- [269] M. T. Ghannam and M. Y. E. Selim, "Rheological Properties of the Jojoba Biofuel," *Sustainability*, vol. 13, no. 11, 2021. doi: 10.3390/su13116047.
- [270] C. Riccardi, S. McCormick, R. Kasi, and C. Kumar, "A Modular Approach for Interlocking Enzymes in Whatman Paper," *Angew. Chemie Int. Ed.*, vol. 57, no. 32, pp. 10158–10162, Aug. 2018, doi: <https://doi.org/10.1002/anie.201805074>.
- [271] A. Zhu *et al.*, "Cleaner enzymatic production of biodiesel with easy separation procedures triggered by a biocompatible hydrophilic ionic liquid," *Green Chem.*, vol. 22, no. 6, pp. 1944–1951, 2020, doi: 10.1039/C9GC03796A.
- [272] R. A. Sheldon, "Biocatalysis in ionic liquids: state-of-the-union," *Green Chem.*, vol. 23, no. 21, pp. 8406–8427, 2021, doi: 10.1039/D1GC03145G.

Publications (from Thesis)

1. **Pranay Amruth Maroju**, Pranathi Tata, Aniket Balapure, Jayati Ray Dutta, and Ramakrishnan Ganesan. "Lactobacillus amylovorus derived lipase-mediated silver derivatization over poly (ϵ -caprolactone) towards antimicrobial coatings." *Enzyme and Microbial Technology* 150 (2021): 109888.
(Pranay Amruth Maroju and Pranathi Tata contributed equally to this work).
2. Hrishikesh Shashi Prakash, **Pranay Amruth Maroju**, Naga Sai Sriteja Boppudi, Aniket Balapure, Ramakrishnan Ganesan, and Jayati Ray Dutta. "Influence of citrate buffer and flash heating in enhancing the sensitivity of ratiometric genosensing of Hepatitis C virus using plasmonic gold nanoparticles." *Micro and Nano Systems Letters* 9 (2021): 8.
(Hrishikesh Shashi Prakash and Pranay Amruth Maroju contributed equally to this work).
3. **Pranay Amruth Maroju**, Ramakrishnan Ganesan, and Jayati Ray Dutta. "Fluorescence-based simultaneous dual oligo sensing of HCV genotypes 1 and 3 using magnetite nanoparticles." *Journal of Photochemistry and Photobiology B: Biology* 232 (2022): 112463.
4. **Pranay Amruth Maroju**, Ramakrishnan Ganesan, and Jayati Ray Dutta. "Boronic acid chemistry for fluorescence-based quantitative DNA sensing." *Chemical Communications* 58 (2022): 7936-7939.
5. **Pranay Amruth Maroju**, Ramakrishnan Ganesan, and Jayati Ray Dutta. "Efficient biodiesel production from rice bran oil using magnetite immobilized-recombinant lipase from probiotic *Bacillus licheniformis*". *Green Chemistry* 24 (2022):8800–11.
6. **Pranay Amruth Maroju**, Ramakrishnan Ganesan, and Jayati Ray Dutta. "Biofuel generation from food waste through immobilized enzymes on magnetic nanoparticles". *Materials Today Proceedings* 72 (2022): 62-66.

Publications (outside Thesis)

1. Aniket Balapure, Mariya Midhu Francis, Hemanjali Mude, **Pranay Amruth Maroju**, Jayati Ray Dutta, and Ramakrishnan Ganesan. "ZnO core-triggered nitrogen-deficient carbonaceous g-C₃N₄ shell enhances the visible-light-driven disinfection." *Carbon Trends* 5 (2021): 100118.
2. Hemanjali Mude, **Pranay Amruth Maroju**, Aniket Balapure, Ramakrishnan Ganesan, and Jayati Ray Dutta. "Quaternized polydopamine coatings for anchoring molecularly dispersed broad-spectrum antimicrobial silver salts." *ACS Applied Bio Materials* 4, no. 12 (2021): 8396-8406.
3. Hemanjali Mude, Anindita Thakur, Aniket Balapure, **Pranay Amruth Maroju**, , Ramakrishnan Ganesan, and Jayati Ray Dutta. "Edible Acid–Base Complexes of Caffeic Acid with Histidine and Arginine Exhibit Enhanced Antimicrobial and Antioxidant Characteristics." *ACS Food Science & Technology* 2 (2022):368–377.
4. Hemanjali Mude, **Pranay Amruth Maroju**, Aniket Balapure, Ramakrishnan Ganesan, and Jayati Ray Dutta. "Water-soluble caffeic acid-dopamine acid-base complex exhibits enhanced bactericidal, antioxidant, and anticancer properties." *Food Chemistry* 374 (2022): 131830.

(Hemanjali Mude and Pranay Amruth Maroju contributed equally to this work)

Publications (from previous work)

1. **Pranay Amruth Maroju**, Sonu Yadav, Vishnupriya Kolipakam, Shweta Singh, Qamar Qureshi, and Yadvendradev Jhala. "Schrodinger's scat: a critical review of the currently available tiger (*Panthera Tigris*) and leopard (*Panthera pardus*) specific primers in India, and a novel leopard specific primer." *BMC genetics* 17 (2016): 1-6.
(*Pranay Amruth Maroju and Sonu Yadav authors contributed equally to this work*)
2. Sonal Saxena, **Pranay Amruth Maroju**, Sumana Choudhury, Anuhya Anne, and K. Naga Mohan. "Analysis of transcript levels of a few schizophrenia candidate genes in neurons from a transgenic mouse embryonic stem cell model overexpressing DNMT1." *Gene* 757 (2020): 144934.
3. Sonal Saxena, **Pranay Amruth Maroju**, Sumana Choudhury, Vidhya Chitta Voina, Poonam Naik, Kavitha Gowdhaman, Poornima Kkani et al. "Functional Analysis of DNMT1 SNPs (rs2228611 and rs2114724) Associated with Schizophrenia." *Genetics Research* (2021).
4. **Pranay Amruth Maroju** and Kommu Naga Mohan. "DNA Methyltransferases and Schizophrenia: Current Status." In *Psychosis-Phenomenology, Psychopathology and Pathophysiology*. IntechOpen, (2021).
5. Sonal Saxena, Sumana Choudhury, **Pranay Amruth Maroju**, Anuhya Anne, Lov Kumar, and Kommu Naga Mohan. "Dysregulation of schizophrenia-associated genes and genome-wide hypomethylation in neurons overexpressing DNMT1." *Epigenomics* 13 (2021): 1539-1555.

Conferences

1. Delivered an **Oral Presentation** on “Biofuel generation from food waste through immobilized enzymes on magnetic nanoparticles” at Novel Materials and Technologies for Energy Applications (NMTEEA-2022), held at BITS-Pilani, Hyderabad Campus.



2. Delivered a **Turbo Talk** on “Boronic acid chemistry for fluorescence-based quantitative nucleotide sensing” at International Symposium on Human Diseases (ISHD-2022), held at BITS-Pilani, Hyderabad Campus.
3. Presented a **Poster** on “Boronic acid chemistry for fluorescence-based quantitative nucleotide sensing” at National Symposium on Convergence of Chemistry & Materials (CCM-2023), held at BITS-Pilani, Hyderabad Campus. (Awarded a certificate with a cash prize)



Biography of Student

Mr. Pranay Amruth Maraju obtained his Masters degree (M.Sc-2012) in Biotechnology from Loyola Academy, Hyderabad, India. He cleared CSIR-UGC NET (lectureship) with the All India 27th rank in June 2012. He joined as a research fellow and obtained his basic training in molecular biology at the Laboratory for Conservation of Endangered Species (LaCONES), Center for Cellular and Molecular Biology (CCMB), Hyderabad, India, in October 2012. Later, he was a research biologist (Genetics) in the All India Tiger Monitoring Project at the Wildlife Institute of India, Dehradun (2013-2014). Since 2015, he has been associated with BITS-Pilani, Hyderabad. He briefly worked as a Research Associate at Bharat Biotech from 2016 to 2018. He enrolled for his Ph.D. at BITS-Pilani in June 2018.

Biography of Supervisor

Prof. Jayati Ray Dutta, Professor of Biological Sciences, has been with Birla Institute of Technology and Science, Pilani, Hyderabad Campus, India, since 2008. She obtained her Masters degree from Calcutta University (India) in 2000 and Ph.D. from the Indian Institute of Technology, Kharagpur (India) in 2004. She also served as DST FAST TRACK Young Scientist at IIT, Kharagpur, India, till July 2008.

Prof. Ray Dutta's research focuses on Nano biotechnology, Microbial Enzymology and its applications in biofuel production, polymer degradation for bio implantation, and bio sensing. Beginning her professional career in 2000, Prof. Ray Dutta has almost 23 years of academic and industry experience in Microbial Biotechnology. She has published over 50 research papers with 825 citations in reputable international journals and conferences. She has been a member of academic societies and associations, including the European Federation of Biotechnology, the Biotech Research Society, and the Probiotic Association of India (Life member). She has been an editorial board member and reviewer for many reputed international journals like Nature, Bioresource Technology, Enzyme and Microbial Technology, ACS Applied Polymer Materials, and many more. Currently, her group is developing industrially important enzymes like lipases and proteases, which are natural biocatalysts from different microbial sources for commercial purposes. She has completed research projects sponsored by CSIR, DST, DBT, and UGC, India, and is currently engaged with two DST grants.

Biography of Co-Supervisor

Prof. Ramakrishnan Ganesan, Professor in Chemistry, has been associated with Birla Institute of Technology and Science, Pilani, Hyderabad Campus, India since 2012. He obtained his Masters degree from Anna University (India) in 2002, and Ph.D. from Korea Advanced Institute of Science and Technology (KAIST, South Korea) in 2006. Later, he served as post doctoral scientist at KAIST, University of Liverpool (United Kingdom) between 2006 to 2008. He was a Scientific employee at Helmholtz-Zentrum Geesthacht (HZG), Teltow, Germany during 2008 to 2010 and as a Scientist, Institute of Materials Research and Engineering (IMRE), Singapore during 2010-2012.

Prof. Ramakrishnan's research focus is on Lithography, Materials Design & Synthesis, Photo(catalysis), Biosensing and Biomaterials. He has 16 years of academic experience in the field of Materials Chemistry and published over 100 research papers with 1770 citations in reputed international journals and conferences. He has been editorial board member and reviewer for many International Journals. Currently, his group is engaged in the development of industrially important materials based on precious metals. He has completed research projects sponsored by BITS and DST and is currently engaged with a CSIR project and a DST grants.